Chemical Geology 672 (2025) 122505

Contents lists available at ScienceDirect

Chemical Geology

journal homepage: www.elsevier.com/locate/chemgeo

A new geochemical database for ocean island basalts: Inferring an OIB mantle source from unevenly sampled oceanic hotspots

Sunna Harðardóttir *, Matthew G. Jackson

University of California Santa Barbara, Department of Earth Science, Santa Barbara, CA 93106-9630, USA

A R T I C L E I N F O

Editor: Don Porcelli

Keywords:
Mantle geochemistry
Hotspot volcanism
Ocean island basalt
Radiogenic isotopes
Helium isotopes

A B S T R A C T

The geochemistry of ocean island basalts (OIB) provides important information about the composition of the mantle, its temporal evolution, and insights into crustal recycling and magma genesis. We present a new ocean island basalt isotope database (OIBID) from 48 oceanic hotspots that includes isotope data ($^{87}Sr/^{86}Sr$, $^{143}Nd/^{144}Nd$, $^{176}Hf/^{177}Hf$, $^{206}Pb/^{204}Pb$, $^{207}Pb/^{204}Pb$, $^{208}Pb/^{204}Pb$, $^{187}Os/^{188}Os$, $^{3}He/^{4}He$ and $\delta^{18}O$) from over 1250 publications. The OIBID includes >13,000 samples and provides major and trace element concentrations and relevant metadata (sample location, methods, etc.), where available. In OIBID there are >41,000 individual isotope analyses that, when combined with individual major element and trace elements data, represent nearly 370,000 individual data entries in the database. Specific criteria are provided to identify the highest quality geochemical OIB data and filter the dataset for presentation here. After filtering, the OIBID is used to identify relationships between radiogenic isotopes and incompatible trace element ratios that resolve enriched mantle (EM) from HIMU (high $^{238}U/^{204}Pb$) mantle domains. We also show that EM lavas have only low MgO, while HIMU and high $^{3}He/^{4}He$ lavas range from low to high MgO. Additionally, we show that many oceanic hotspots still remain uncharacterized for $^{187}Os/^{188}Os$ ($N = 28$ oceanic hotspots lack robust analyses), $^{3}He/^{4}He$ ($N = 16$), and $^{176}Hf/^{177}Hf$ ($N = 15$). We also demonstrate that the existing published isotope data are highly biased: < 25 % of the hotspots (11 of 48 total oceanic hotspots) in the OIBID account for ≥ 75 % of the published Sr-Nd-Pb-Hf-Os-He isotope data. Just two of the 48 oceanic hotspots—Hawaiʻi and Iceland—represent 35 to 45 % of the total published analyses for these isotope systems. To correct for this considerable sampling bias, OIB isotope histograms are reweighted based on hotspot's fractional contribution to the global oceanic hotspot buoyancy flux. After reweighting, the contribution from each oceanic hotspot is in proportion to the mass of upwelling material in the plume. Our results demonstrate that very few OIB (just 7 % of all OIB samples with Nd isotopes analyzed) are geochemically enriched ($^{143}Nd/^{144}Nd < 0.51263$) while the majority of OIB are geochemically depleted (93 % of OIB samples). HIMU OIB ($^{206}Pb/^{204}Pb > 21$) are rare (only 2 % of OIB samples), and high $^{3}He/^{4}He$ OIB ($^{3}He/^{4}He > 20$ R_A) are uncommon (just 9 % of OIB samples). The reweighted dataset shifts global OIB to more radiogenic lead isotope compositions than the unweighted dataset, and more than half of OIB have MORB-like $^{3}He/^{4}He$ (8 ± 2 R_A) in the reweighted dataset. These observations have implications for the dominance of geochemically depleted lavas in the mantle, the formation of the HIMU mantle by subduction of oceanic crust, and the presence of MORB-like $^{3}He/^{4}He$ throughout the upper and lower mantle.

1. Introduction

Ocean island basalts (OIB) and mid-ocean ridge basalts (MORB) are mantle-derived melts that provide a window into the compositional and isotope heterogeneities in the mantle. Geochemical data from mantle-derived basalts such as MORB and OIB demonstrate that Earth's mantle is heterogenous (e.g., Gast et al., 1964; White and Hofmann, 1982). $^{87}Sr/^{86}Sr$, $^{143}Nd/^{144}Nd$ and $^{206}Pb/^{204}Pb$ data for MORB and OIB have been used to identify four mantle end-members: depleted MORB mantle (DMM), high μ (or high $^{238}U/^{204}Pb$, HIMU), enriched mantle 1 (EM-1) and enriched mantle 2 (EM-2) (Zindler and Hart, 1986). A widely-held hypothesis maintains that the isotope signatures of HIMU and EM end-members result from the recycling of crustal materials into the mantle at subduction zones (White and Hofmann, 1982; Hofmann and White, 1982). While many models have been proposed for the origin of EM and HIMU end-members (e.g., White, 1985; Weis et al., 1989;

---

* Corresponding author.
E-mail address: sunna341@ucsb.edu (S. Harðardóttir).

https://doi.org/10.1016/j.chemgeo.2024.122505
Received 16 April 2024; Received in revised form 21 October 2024; Accepted 14 November 2024

Woodhead and McCulloch, 1989; Hoernle et al., 1991; Weaver, 1991; Chauvel et al., 1992; Woodhead and Devey, 1993; Woodhead et al., 1993; Eiler et al., 1995; White and Duncan, 1996; Chauvel et al., 1997; Lassiter and Hauri, 1998; Blichert-Toft et al., 1999; Tatsumi, 2000; Eisele et al., 2002; Workman et al., 2004; Gibson et al., 2005; Honda and Woodhead, 2005; Stracke et al., 2005; Jackson et al., 2007a; Geldmacher et al., 2008; Pilet et al., 2008; Workman et al., 2008; Salters and Sachi-Kocher, 2010; Willbold and Stracke, 2010; Hanyu et al., 2011, 2014; Kawabata et al., 2011; Castillo, 2015; Garapic et al., 2015; Delavault et al., 2016; Weiss et al., 2016; Kendrick et al., 2017; Turner et al., 2017; Castillo et al., 2018; Homrighausen et al., 2018; Wang et al., 2018; Boyet et al., 2019; Cordier et al., 2021; Labidi et al., 2022), high $^{206}Pb/^{204}Pb$ in HIMU lavas are most commonly linked to recycling of altered oceanic crust (Hofmann and White, 1982), while high $^{87}Sr/^{86}Sr$ and low $^{143}Nd/^{144}Nd$ in EM lavas indicate the incorporation of recycled continental crustal materials (White and Hofmann, 1982). These recycled components are mixed with ambient mantle (primarily peridotite) and melted beneath hotspots to generate OIB melts.

In multi-dimensional isotope space, a fifth mantle component that is surrounded by the four mantle end-members has been suggested. This fifth component is thought to be intrinsic to all hotspots and is variously called *Pre*valent *Ma*ntle (PREMA) (Zindler and Hart, 1986), Primitive Helium Mantle (PHEM) (Farley et al., 1992), common component (C) (Hanan and Graham, 1996) or Focal Zone (FOZO) (Hart et al., 1992). This component will be called the "common component" throughout the paper, but we acknowledge that Stracke et al. (2022) has called into question the existence of a common component, and this will be the subject of future work. The common component is geochemically depleted: it has high $^{143}Nd/^{144}Nd$ and $^{176}Hf/^{177}Hf$, and low $^{87}Sr/^{86}Sr$ and $^{206}Pb/^{204}Pb$ that are the result of ancient melt extraction (Hart et al., 1992; Boyet and Carlson, 2005; Class and Goldstein, 2005). High $^{3}He/^{4}He$ signatures have been detected in the common component, which is thought to reflect the sampling of an ancient domain from the lower mantle that has remained less degassed than other mantle domains (Hart et al., 1992; Graham, 2002; Class and Goldstein, 2005; Mundl et al., 2017; Mukhopadhyay and Parai, 2019). The mantle sources of OIB therefore contain both crustal materials that have been recycled into the mantle and less degassed ancient domains (Zindler and Hart, 1986; Mukhopadhyay and Parai, 2019) that are less impacted by crustal recycling (White, 2015; Jackson et al., 2020).

While radiogenic isotopes provide one way to identify mantle end-members, some efforts have been made to use major and trace element chemistry of OIB to identify mantle end-members (e.g., Weaver, 1991; Condie, 2003, 2015; Willbold and Stracke, 2006; Jackson and Dasgupta, 2008; Huang and Zheng, 2017; Akbari et al., 2023). Weaver (1991) argued that the HIMU, EM-1, and EM-2 end-members have distinct trace element compositions that reflect which recycled crustal materials are incorporated into each end-member. For example, HIMU lavas are argued to be depleted in fluid mobile elements relative to fluid immobile elements which results in depletion in Rb, K, U and Pb relative to Th, Nb, and the rare earth elements (e.g., Kendrick et al., 2017). EM lavas tend to exhibit enrichment in Pb and depletion in Ti, Ta, and Nb relative to similarly incompatible elements—resulting in low Ce/Pb, Nb/Th, and Ti/Gd in EM lavas—which signals the presence of recycled continental crust (e.g., Eisele et al., 2002; Jackson et al., 2007a; Hofmann, 2014). Although, EM-1 and EM-2 lavas are distinguishable from HIMU lavas using trace element characteristics, the use of trace elements alone has limitations. For example, Willbold and Stracke (2006) argued that EM-1 and EM-2 lavas cannot be clearly distinguished from one another using only trace element ratios.

Pairing radiogenic isotopes and major elements is also a powerful tool for exploring OIB heterogeneity and origins, which reveals that melts of the different mantle domains exhibit different major element compositions (Jackson and Dasgupta, 2008). Major and trace elements can therefore provide important insights into the mantle sources and melting processes that give rise to OIB, and they are especially powerful tools when used in tandem with radiogenic isotopes. Unfortunately, there is currently no compiled database of high-quality isotope analyses on global OIB that has complementary major and trace element data, and such a resource is needed to explore critical geochemical relationships underlying the origin of OIB. Such databases already exist for MORB (Gale et al., 2013) and arc lavas (Turner and Langmuir, 2015), highlighting the need for a similar geochemical database for OIB. Many review papers on the geochemistry of OIB have been published recently (e.g., White, 2010, 2015; Weis et al., 2023) but none of them had the advantage of a truly *global* OIB database that includes radiogenic isotopes and major and trace element concentrations.

Here we present an OIB isotope database (OIBID) for 48 oceanic hotspots that includes OIB that have been characterized for heavy radiogenic (Sr, Nd, Pb, Hf, and Os), helium and/or oxygen isotopes. Below, we present how the OIBID is constructed, and how the data are treated. We identify important geochemical relationships in the database to show its utility, including some new ways OIB data can be presented. A key finding of this paper is that the available OIB geochemical data are heavily biased toward a small number of hotspots, with the result being that a small number of hotspots are overrepresented in the database and, thus, the database as a whole does not accurately represent the mantle source of global OIB. For example, Hawai'i and Iceland each have 1000's of radiogenic isotope analyses, accounting for 35 % to 45 % of the total Sr-Nd-Pb-Hf-Os-He analyses in global OIB. In contrast, the combined isotope analyses for the 41 least geochemically characterized oceanic hotspots are still less than the total number of Sr-Nd-Pb-Hf-Os-He isotope analyses available for just Hawai'i and Iceland. This overrepresentation of Hawai'i and Iceland strongly impacts the isotope histograms that we use to infer the mantle sources of OIB. After demonstrating the degree to which the geochemical data are biased, we conclude by providing one possible method for "correcting" for the geochemical bias in the OIBID, which allows us to arrive at isotope histograms for global OIB that reflect the average mantle sourced by OIB.

2. Methods

2.1. Data compilation

Isotope, major and trace element data for 48 oceanic hotspots (see Fig. 1 and Table 1) from 1274 publications (see Supplementary Table 1) that were published before August 1st, 2023, are compiled into a database—called OIBID—that includes 13,008 samples (see Supplementary Dataset 1). Our goal is to create a database that is useful for studying heterogeneities in the mantle source of oceanic hotspots. Because isotope compositions provide critical context for interpreting the mantle source compositions and the origin of OIB, a sample is included in the OIBID *only* if at least one of the following isotope ratios has been measured: $^{87}Sr/^{86}Sr$, $^{143}Nd/^{144}Nd$, $^{176}Hf/^{177}Hf$, $^{206}Pb/^{204}Pb$, $^{207}Pb/^{204}Pb$, $^{208}Pb/^{204}Pb$, $^{187}Os/^{188}Os$, $^{3}He/^{4}He$, $\delta^{18}O$ (oxygen isotopes on magmatic phases—olivine, clinopyroxene, plagioclase and glass—are included for completeness, and relationships with radiogenic isotopes and MgO are shown in Supplementary Figs. 1 and 2). For such samples, major and trace element data are also included in the OIBID, if available. However, samples where only major and/or trace elements have been measured (i.e., where none of the aforementioned isotopes have been analyzed) are excluded from the OIBID.

The list of oceanic hotspots considered in this study is shown in Table 1. This study examines the aforementioned geochemical and isotope data (if available) for the 48 commonly-accepted oceanic hotspots (Fig. 1), including 44 of the 45 oceanic hotspots from King and Adam's (2014) hotspot compilation (we exclude Lord Howe-Tasman East due to potential for continental contamination, see Section 4.3.1.11. in the Supplementary Text) as well as four additional oceanic hotspots not included in King and Adam's (2014) hotspot list (i.e., Christmas Island in the Indian Ocean, Conrad, Foundation, and Manus Basin).

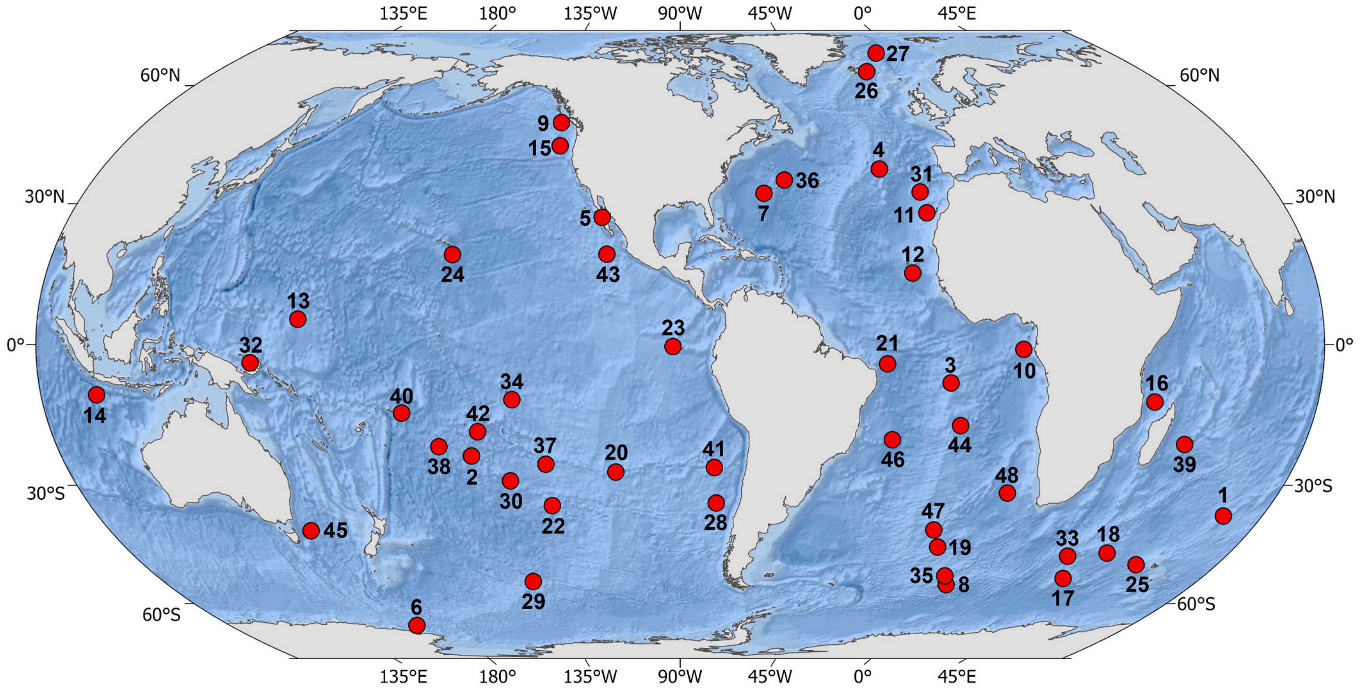

Esri, Garmin, GEBCO, NOAA NGDC, and other contributors

Fig. 1. Locations of the 48 oceanic hotspots that are included in the OIBID. 1 = Amsterdam-St. Paul, 2 = Arago-Rurutu, 3 = Ascension, 4 = Azores, 5 = Baja-Guadalupe, 6 = Balleny, 7 = Bermuda, 8 = Bouvet, 9 = Bowie-Kodiak/Pratt-Welker, 10 = Cameroon, 11 = Canary, 12 = Cape Verde, 13 = Caroline, 14 = Christmas Island, 15 = Cobb-Eickelberg/Axial-Juan de Fuca, 16 = Comoros, 17 = Conrad, 18 = Crozet, 19 = Discovery, 20 = Easter, 21 = Fernando de Noronha, 22 = Foundation, 23 = Galápagos, 24 = Hawaiʻi, 25 = Heard-Kerguelen, 26 = Iceland, 27 = Jan Mayen, 28 = Juan Fernández, 29 = Louisville, 30 = Macdonald, 31 = Madeira, 32 = Manus Basin, 33 = Marion-Prince Edward, 34 = Marquesas, 35 = Meteor-Shona, 36 = New England, 37 = Pitcairn, 38 = Rarotonga, 39 = Réunion, 40 = Samoa, 41 = San Félix, 42 = Sociétiés, 43 = Socorro-Revillagigedo, 44 = St. Helena, 45 = Tasmantid-Tasman Central, 46 = Trindade-Martín Vaz, 47 = Tristan-Gough-Walvis Ridge, and 48 = Vema.

Following an approach taken previously for a similarly compiled geochemical database for Icelandic lavas (Harðardóttir et al., 2018, 2022), geochemical data in the OIBID are *manual data entries* taken from primary references. Data are not compiled from other databases like GEOROC (https://georoc.eu/georoc/new-start.asp), PetDB (https://search.earthchem.org/), or GERM (https://earthref.org/GERM/#gsc.tab=0), etc. However, the GEOROC database is used as a starting point to find references with data to include in the OIBID. We include only geochemical data from published references. Data from unpublished dissertations are not included. The references that are used to compile the OIBID are listed in Supplementary Table 1.

After the geochemical data have been compiled, the OIBID is carefully filtered for typos in the primary references, for low-temperature alteration, for samples impacted by extreme magmatic differentiation and/or crustal assimilation, for less precise analytical techniques and/or data disagreement between analytical techniques, etc. (see Section 2.2 and Supplementary Text). These make the new database robust relative to other existing compilations.

2.2. Data Filtering and Data Exclusion

Isotope, major, and trace element data in the OIBID are filtered prior to data analyses to identify high-quality geochemical data (but the data that are filtered from figures and discussion are included in the OIBID). However, a subset of data are excluded from the OIBID: samples without radiogenic isotope or $\delta^{18}O$ analyses, non-igneous rocks, xenolith data, ${}^{187}Os/{}^{188}Os$ and ${}^{3}He/{}^{4}He$ analyses without complementary [Os] and [${}^{4}He$], ${}^{187}Os/{}^{188}Os$ not measured by negative ion mode-thermal ionization mass spectrometry (N-TIMS), ${}^{176}Hf/{}^{177}Hf$ analyses by TIMS, oceanic samples that are contaminated by continental lithosphere (Lord Howe-Tasman East hotspot and some Tasmantid-Tasman Central data), etc..

For the data that remain in the OIBID after exclusion using criteria described above, additional filtering is applied for display purposes in figures and for discussion regarding comparison with unfiltered data, but filtering does not result in exclusion of data from the OIBID. Where data filtering has been applied, the unfiltered geochemical parameter is given in one column and the filtered geochemical parameter is given in a separate column in Supplementary Dataset 1. Therefore, the filtered geochemical data that is used in figures can be easily identified in the database. A detailed description of the methods used for data filtering and data exclusion is provided in the Supplementary Text, and a brief description of the filtering methods is provided here and in Table 2.

The isotope systems included in the OIBID are filtered in different ways for display in figures and the discussion (i.e., ${}^{87}Sr/{}^{86}Sr$ are filtered using an MgO threshold, lower quality unspiked TIMS Pb isotope analyses, ${}^{187}Os/{}^{188}Os$ using an [Os] threshold, and ${}^{3}He/{}^{4}He$ using a [${}^{4}He$] threshold). For example, ${}^{87}Sr/{}^{86}Sr$ data in lavas with $MgO < 2.0$ wt% or no MgO are not shown in figures (except for Fig. 6) because highly evolved lavas tend to have high Rb/Sr and evolve post-eruptive radiogenic ${}^{87}Sr/{}^{86}Sr$ ratios. The filtered ${}^{87}Sr/{}^{86}Sr$ data are given in column AH of Supplementary Dataset 1. Similarly, samples with low [Os] are susceptible to crustal contamination (e.g., Class et al., 2009). Therefore, with the exception of Supplementary Fig. 4, samples with $[Os] < 50$ ppt (Eisele et al., 2002; Debaille et al., 2009) are not shown in figures and excluded from discussion; different [Os] thresholds could be used (e.g., Gibson et al., 2016), which is why ${}^{187}Os/{}^{188}Os$ and [Os] data are preserved for all samples in the OIBID. The filtered ${}^{187}Os/{}^{188}Os$ data are given in column CD of Supplementary Dataset 1. Likewise, samples with low [${}^{4}He$] are susceptible to crustal assimilation and/or post-eruptive radiogenic ingrowth of ${}^{4}He$ (Hilton et al., 1995; Class and Goldstein, 2005). Therefore, helium concentration thresholds (i.e., $[{}^{4}He] < 90$ $ncm^{3}STP/g$ for glasses, < 4 $ncm^{3}STP/g$ for olivine, and < 2 $ncm^{3}STP/g$ for clinopyroxene) are applied to the ${}^{3}He/{}^{4}He$ data to filter samples with

Table 1
The 48 oceanic hotspots included in the OIBID.

#	Short name	Oceanic hotspot	Latitude	Longitude	Buoyancy flux (Mg/s)[1]
1	AMSTER	Amsterdam-St. Paul	−37	78	*0.5*
2	ARAGO	Arago-Rurutu	−23.5	−150.7	*0.5*
3	ASCENS	Ascension	−7.93	−14.37	0.8
4	AZORES	Azores	38	−28	1.0
5	BAJAGU	Baja-Guadalupe	27	−113	*0.5*
6	BALLENY	Balleny	−67.4	164.7	2.2
7	BERMUDA	Bermuda	32.4	−64.7	1.1
8	BOUVET	Bouvet	−54.4	3.4	*0.5*
9	BOWIE	Bowie-Kodiak/ Pratt-Welker	49.5	−130	0.7
10	CAMERO	Cameroon	−1	6	1.1
11	CANARY	Canary	28	−17	0.8
12	CAPEVER	Cape Verde	15	−24	1.4
13	CAROLINE	Caroline	5.3	163	1.1
14	CHRISTM	Christmas Island	−10.5	105.7	*0.5*
15	COBB	Cobb-Eickelberg/ Axial-Juan de Fuca	43.6	−128.7	0.5
16	COMOROS	Comoros	−12	44	1.0
17	CONRAD	Conrad	−52.7	42.5	*0.5*
18	CROZET	Crozet	−46	50	0.8
19	DISCOV	Discovery	−44.5	−6.5	0.5
20	EASTER	Easter	−27	−109	1.6
21	FERNANDO	Fernando de Noronha	−4	−32	0.7
22	FOUNDA	Foundation	−34.6	−129	*0.5*
23	GALAPA	Galápagos	−0.4	−92	1.5
24	HAWAII	Hawaiʻi	18.9	−155.3	5.6
25	HEARD	Heard-Kerguelen	−49	63	1.1
26	ICELAND	Iceland	64.6	−17.6	5.2
27	JANMAYEN	Jan Mayen	71.7	−8	0.6
28	JUANFERN	Juan Fernández	−34	−79	1.5
29	LOUISVILLE	Louisville	−53.5	−141.2	1.5
30	MACDON	Macdonald	−29	−140.4	2.6
31	MADEIRA	Madeira	32.7	−17.5	*0.5*
32	MANUS	Manus Basin	−3.8	149.7	*0.5*
33	MARION	Marion-Prince Edward	−46.8	37.8	1.2
34	MARQUES	Marquesas	−11.5	−137.5	2.6
35	METEOR	Meteor-Shona	−52	1	0.5
36	NEWENGL	New England	35.4	−58.1	0.7
37	PITCAIRN	Pitcairn	−25.3	−129.3	2.1
38	RAROTO	Rarotonga	−21.5	−159.7	1.9
39	REUNION	Réunion	−21	55.5	1.5
40	SAMOA	Samoa	−14.3	−169	1.9
41	SANFELIX	San Félix	−26	−80	1.7
42	SOCIETY	Sociétiés	−18.3	−148	3.2
43	REVILLA	Socorro-Revillagigedo	19	−111	*0.5*
44	STHELENA	St. Helena	−17	−10	0.5
45	TASMAN	Tasmantid-Tasman Central	−40.5	153.4	0.9
46	TRINDADE	Trindade-Martín Vaz	−20	−29	0.9
47	TRISTAN	Tristan-Gough-Walvis Ridge	−40.3	−10	1.0
48	VEMA	Vema	−31.7	8.4	*0.5*

[1] The buoyancy fluxes given in the table are calculated averages. The compilation used to calculate averages is given in Supplementary Table 2, and a description of how the averages are calculated is given in the Supplementary Text. Oceanic hotspots that have buoyancy fluxes <0.5 Mg/s or that have no prior buoyancy flux estimates are assigned a buoyancy flux of 0.5 Mg/s; these buoyancy fluxes are underlined and shown in italics. See the Supplementary Text for explanation.

Table 2
Overview of filtering criteria used for analysis of OIB data for display in figures[1].

	Analytical techniques	MgO threshold	Trace element threshold[2]	Other
^{87}Sr/^{86}Sr ^{143}Nd/^{144}Nd ^{176}Hf/^{177}Hf $^{206/207/208}$Pb/^{204}Pb	Lower quality unspiked TIMS analyses (i.e., analyses that fall outside of a 2σ envelope and/or the range defined by high-precision Pb isotope data) are filtered out	2.0 wt%		Unspiked TIMS data that fall within a 2σ envelope, and the range defined by Tl-addition and Pb-double and triple spike methods are included.
^{187}Os/^{188}Os			[Os] > 50 ppt	
^{3}He/^{4}He			[^{4}He] > 90 ncm^{3}STP/g for glasses, > 4 ncm^{3}STP/g for olivine, and > 2 ncm^{3}STP/g for clinopyroxenxe	
Major elements				All 10 major elements measured on the sample are required, as well as totals > 95 % and < 102 % on a volatile free basis.
Trace elements	Only ICP-MS measurements included	5.0 wt%	LOI < 4 wt%, Ba/Rb > 6 and < 50, Ce/Ce* > 0.8 and < 1.2, and Y/Y* > 0.7 and < 1.3	

[1] While the OIB data are filtered for display in figures using the criteria in this table, the data are preserved in OIBID. However, the filtering approach in this table is applied only after exclusion of particular data from OIBID for the following reasons: exclusion of samples without any radiogenic isotope or δ^{18}O analyses (i.e., samples that have only major and/or trace element analyses are excluded), non-igneous rocks and xenoliths, He and Os isotope data that lacks corresponding concentrations, Os isotopes not measured by N-TIMS, Hf isotopes measured by TIMS, oceanic samples contaminated by continental lithosphere, sample preparation with W-carbide (which results in exclusion of Ta concentration and Hf isotope data), data typos in the manuscripts presenting the data, and data that appear to be of poor quality based on reasons provided in Supplementary Table 4.

[2] Isotope data provided in Supplementary Dataset 1 are not filtered for alteration, for example using the following proxies for rock alteration state: Ba/Rb, Ce/Ce*, Y/Y*, and LOI. This is because isotope data show no global relationships with these alteration indices (see Supplementary Fig. 6). This is likely due to the fact that OIB samples are frequently acid leached prior to isotope analysis.

low [^{4}He] (see Supplementary Fig. 5 where thresholds are shown). The filtered ^{3}He/^{4}He data are given in column CJ of Supplementary Dataset 1. The only figures where these isotope filters are *not* applied are the figures used to demonstrate the need for the filter (e.g., ^{87}Sr/^{86}Sr versus MgO [Fig. 6], ^{187}Os/^{188}Os vs [Os] [Supplementary Fig. 4], ^{3}He/^{4}He vs [^{4}He] [Supplementary Fig. 5]).

High-precision Pb-isotope analyses (i.e., double or triple spike method by TIMS, or the Tl addition or Pb-spike method by multi-collector (MC)-ICP-MS) are identified separately from unspiked TIMS Pb isotope analyses in the OIBID. High-precision Pb-isotope data are given in columns AN, AP, and AR in Supplementary Dataset 1. In the subset of Pb isotope data represented by unspiked TIMS analyses there are two groups: a higher quality unspiked TIMS group (i.e., all unspiked TIMS Pb isotope analyses that fall within a 2σ envelope and the range defined by precise Pb isotope analyses), and a lower quality unspiked TIMS Pb isotope analyses (i.e., all unspiked TIMS Pb isotope analyses that fall outside a 2σ envelope and/or the range defined by precise Pb isotope analyses) (see Section 4.3.2.1. of the Supplementary Text and Supplementary Fig. 3 for a full description of how the quality of unspiked TIMS analyses is determined). The lower quality unspiked TIMS Pb isotope analyses are filtered from figures and excluded from discussion, but lower quality unspiked TIMS Pb analyses are still preserved in the OIBID. The higher quality, filtered unspiked TIMS analyses that are shown in many (but not all) figures, are given in separate columns (i.e., columns BB, BD, BF) in Supplementary Dataset 1.

After filtering the isotope data (i.e., MgO, [Os], and [^{4}He] thresholds are applied and lower quality unspiked TIMS Pb isotope data are filtered), 4303 OIB in the database have complete Sr-Nd-Pb isotope analyses on the same sample, and 1902 of these samples have complete Sr-Nd-Pb-Hf isotope analyses. If ^{3}He/^{4}He data are included, then 339 samples in OIBID have complete Sr-Nd-Pb-He isotope analyses, 158 samples have complete Sr-Nd-Hf-Pb-He isotope analyses, and only 48 samples in OIBID have complete Sr-Nd-Hf-Pb-Os-He isotope analyses.

Additionally, trace element data included in the OIBID are filtered using several criteria for display in figures and the discussion (but the trace element data that have been filtered from figures and discussion are preserved in the OIBID). These filters include the analytical technique, an MgO threshold (for magmatic differentiation), and trace element ratio thresholds (for low temperature alteration). Figures show only trace element data measured by inductively coupled plasma mass spectrometry (ICP-MS) (except for [Os]—which is measured by N-TIMS—and [He]). Low MgO lavas can have highly fractionated incompatible trace element ratios (see Fig. 3 and Supplementary Fig. 8), and we find that a threshold of 5 wt% MgO (similar to Willbold and Stracke's (2006) threshold of 4 to 5 wt% MgO) successfully filters samples that have experienced significant trace element fractionation due to magmatic evolution. Trace element data filtered to exclude only lavas with MgO < 5 wt% are given in columns GY to JU of Supplementary Dataset 1.

All samples with LOI > 4 wt%, Ba/Rb < 6 or > 50, Ce/Ce* < 0.8 or > 1.2, or Y/Y* < 0.7 of > 1.3 are suspected to have been affected by alteration (where $Ce/Ce^* = Ce_N/(La_N \times Pr_N)^{0.5}$ and $Y/Y^* = Y_N/(Dy_N \times Yb_N)^{0.5}$, where N represents normalization to primitive mantle from McDonough and Sun, (1995)). These samples as well as samples that lack data used for calculating the alteration filters, are shown with black "x" symbols in trace element figures. In this study we do not apply MnO and P_2O_5 filters for low temperature alteration because high MnO (> 0.5 wt%) and P_2O_5 (> 3 wt%) samples are all filtered out when other alteration filters used in this study are applied (i.e., LOI, Ba/Rb, Ce/Ce*, and Y/Y*) (see Supplementary Fig. 7). The alteration filters are applied to plots showing trace elements (trace elements versus trace elements, or trace elements versus isotopes), except for figures showing trace element ratios versus MgO (Fig. 3 and Supplementary Fig. 8) and trace element alteration filters versus isotopes (Supplementary Fig. 6). Trace element data filtered to exclude both evolved samples (MgO < 5 wt%) and samples with alteration signatures (i.e., no reported LOI, Ba/Rb, Ce/Ce*, Y/Y* or LOI > 4 wt%, Ba/Rb < 6 or > 50, Ce/Ce* < 0.8 or > 1.2, or Y/Y* < 0.7 or > 1.3), are given in columns JX to MT of Supplementary Dataset 1. Additionally, trace element data filtered to exclude only samples with alteration signatures (i.e., no reported LOI, Ba/Rb, Ce/Ce*, Y/Y* or LOI > 4 wt%, Ba/Rb < 6 or > 50, Ce/Ce* < 0.8 or > 1.2, or Y/Y* < 0.7 or > 1.3)—thereby preserving both fresh samples that are evolved (MgO < 5 wt%) and more primitive (MgO > 5 wt%)—are given in columns MW to PS of Supplementary Dataset 1.

The alteration filters are not applied to isotope versus isotope plots, otherwise too much of the isotope dataset would be lost. Critically, figures showing isotope ratios versus alteration filters show no relationships (Supplementary Fig. 6). This is likely a result of acid leaching (and concomitant removal of alteration of signatures) that is applied community-wide to most sample material prior to dissolution and chemistry.

3. Results and discussion

3.1. Geochemical characteristics of OIB

3.1.1. Major and trace element geochemistry of OIB as a function of magmatic differentiation

MgO is used as a proxy to investigate how magmatic differentiation affects geochemical compositions in OIB (Figs. 2–3 and Supplementary Figs. 7–8). Again, the OIBID is not comprehensive for major and trace elements measured in OIB: geochemical data are presented only for lavas that have had at least one isotope ratio (Sr-Nd-Pb-Hf-Os-He-O) measured, as isotopes provide critical geochemical information about mantle sources of OIB.

3.1.1.1. Major element geochemistry of OIB as a function of MgO content. In Fig. 2, the TAS diagram (Macdonald and Katsura, 1964) is shown to demonstrate that OIB in the database span a wide range of compositions, from tholeiitic to alkalic (e.g., Weis et al., 2023). Additionally, SiO_2 is plotted against MgO to demonstrate that the OIBID samples a wide range magmatic evolution. In Supplementary Fig. 7, the remaining major element oxides are plotted versus MgO.

3.1.1.2. Trace element geochemistry of OIB as a function of MgO content. In Fig. 3 and Supplementary Fig. 8 we evaluate how magma differentiation affects trace element ratios by plotting them as a function of MgO. Rb/Sr, Ba/Th, Sr/Sr*, Ba/Nb, and Eu/Eu* all show extreme fractionation at low MgO (< 2 wt%) (where $Sr/Sr^* = Sr_N/(Sm_N \times Nd_N)^{0.5}$ and $Eu/Eu^* = Eu_N/(Sm_N \times Gd_N)^{0.5}$). Ba/Th, Sr/Sr*, Ba/Nb and Eu/Eu* all decrease substantially, and Rb/Sr increases, at MgO < 2 wt%. These indicate depletion in Sr, Ba, and Eu—all of which partition into plagioclase during magma evolution—in differentiated lavas (Bindeman et al., 1998).

High field strength elements (HFSE) also exhibit extreme fractionation at low MgO. Zr/Zr* and Hf/Sm increase at low MgO (< 5 wt%) (where $Zr/Zr^* = Zr_N/(Sm_N \times Nd_N)^{0.5}$), indicating the accumulation of a zirconium or hafnium rich phase (e.g., zircon), but we cannot exclude fractionation of rare earth element (REE)-rich phases (Supplementary Fig. 8). Additionally, Ti/Gd decreases at low MgO (< 5 wt%), indicating the loss of a Ti-rich phase. Nb/Ta ratios also increase substantially at low MgO (< 5 wt%), indicating the accumulation of a high Nb/Ta phase, or fractionation of a low Nb/Ta phase. Similarly, at MgO < 5 wt% the Nb/Th ratio shows considerable variability, trending to both very high and very low ratios. Nb/Ta (Green, 1995; Kamber and Collerson, 2000) and Nb/Th ratios (Willhite et al., 2019) are considered to be relatively constant and indicative of mantle source in primitive lavas, but this is clearly only the case when lavas are sufficiently primitive to have not experienced HFSE fractionation.

Similarly, K_2O/P_2O_5 increases substantially at low MgO (< 5 wt%) demonstrating that high K_2O/P_2O_5 is the result of magma differentiation, most likely through fractional crystallization of a phosphorus-rich phase such as apatite (Fig. 3b). Given the sensitivity of K_2O/P_2O_5 to magmatic differentiation, there are potential concerns regarding the reliability of K_2O/P_2O_5 as an indicator of alteration (e.g., Hauri, 1996; Pietruszka et al., 2013; Ruttor et al., 2021).

Some REE ratios also demonstrate fractionation at low MgO (<2 wt %), as demonstrated by La/Sm versus MgO (Supplementary Fig. 8), which shows that lavas with the highest La/Sm ratios also have the lowest MgO. Similarly, K/La (and K/Nb, not shown) increases at low MgO (< 2 wt%) (Supplementary Fig. 8).

In general, we find that fractionation of incompatible trace elements by magmatic differentiation is greatly minimized by using an MgO threshold of 5 wt%. Throughout the remainder of this paper, we plot only trace element data for samples with >5 wt% MgO.

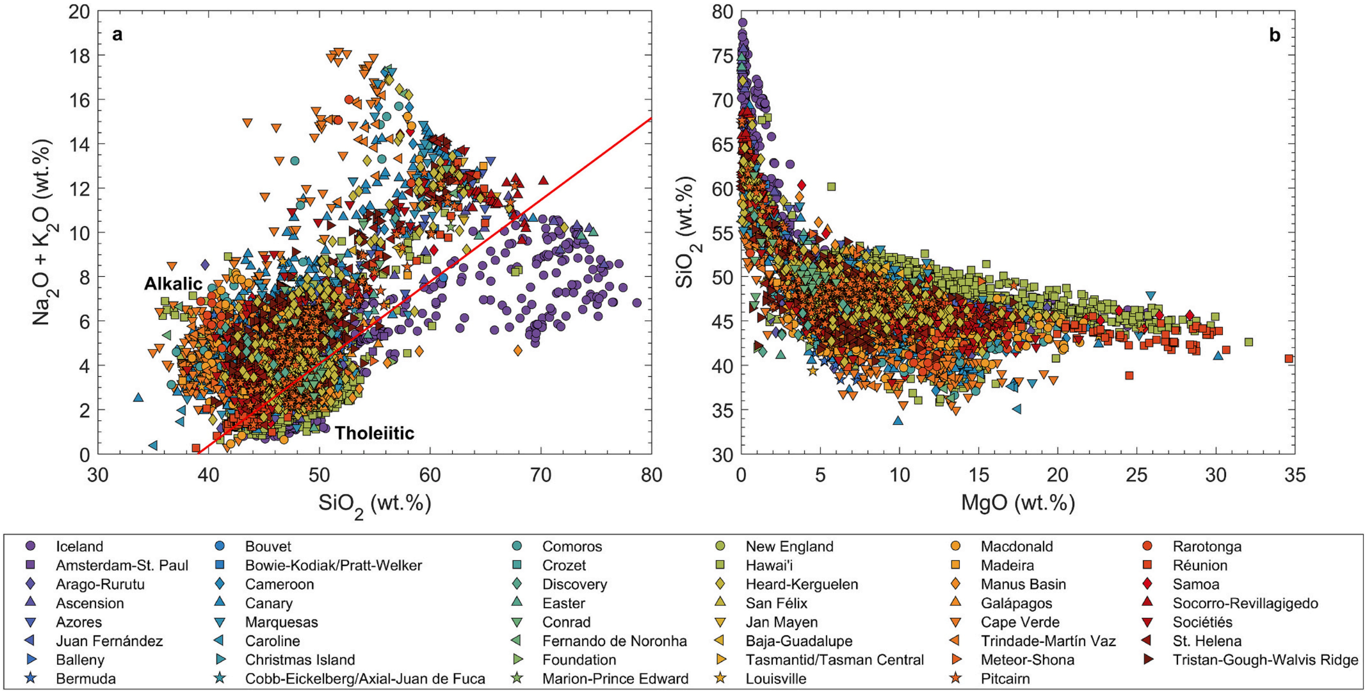

Fig. 2. Major element chemistry of global OIB. a) TAS diagram that shows $Na_2O + K_2O$ plotted against SiO_2 with the tholeiitic-alkalic dividing line (in red) from Macdonald and Katsura (1964), and b) SiO_2 plotted against MgO. The figure shows only major element data for OIB samples that have been characterized for at least one isotope ratio (i.e., $^{87}Sr/^{86}Sr$, $^{143}Nd/^{144}Nd$, $^{176}Hf/^{177}Hf$, $^{206}Pb/^{204}Pb$, $^{207}Pb/^{204}Pb$, $^{208}Pb/^{204}Pb$, $^{187}Os/^{188}Os$, $^{3}He/^{4}He$ and/or $\delta^{18}O$). Other plots showing major element oxides versus MgO are presented in Supplementary Fig. 7. (For interpretation of the references to color in this figure legend, the reader is referred to the web version of this article.)

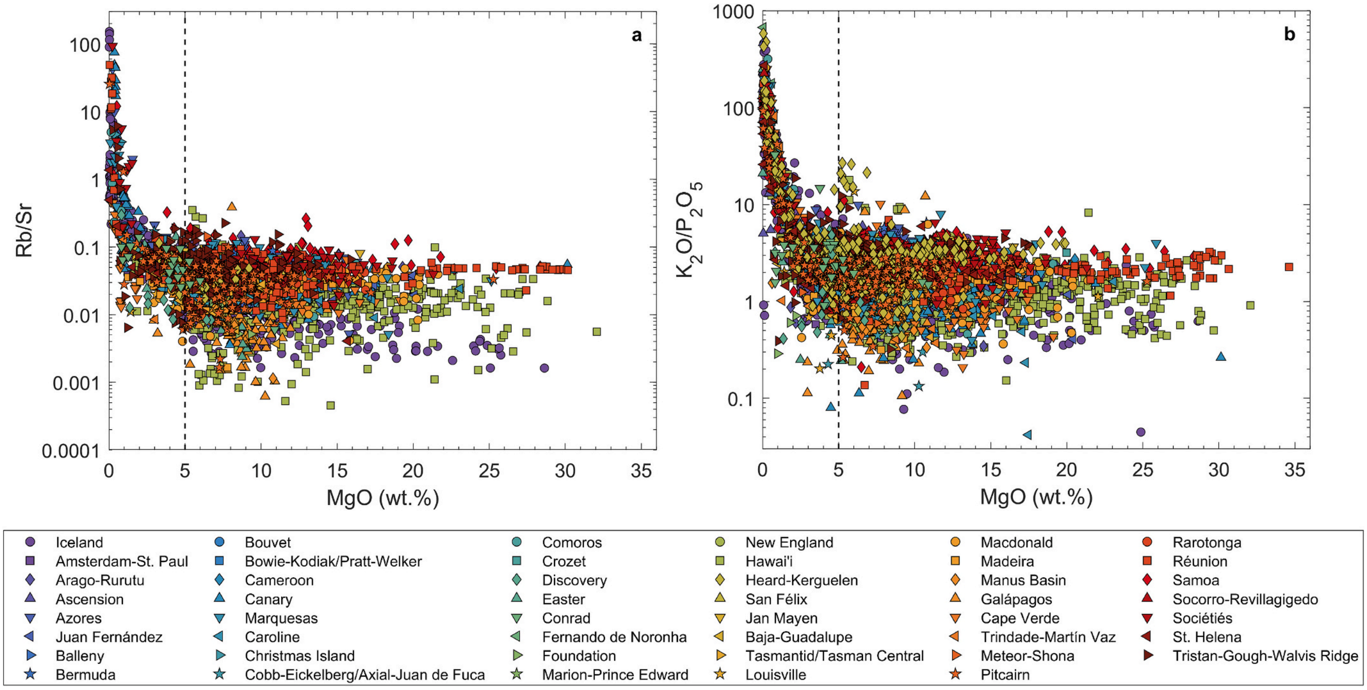

Fig. 3. Trace element ratios plotted against MgO. a) Rb/Sr plotted against MgO, and b) K_2O/P_2O_5 plotted against MgO. The vertical black dashed line is plotted at 5 wt% MgO, which is the MgO threshold that is used to filter differentiated lavas from the trace element dataset. The figure shows only trace element data measured by ICP-MS on OIB samples that have been characterized for at least one isotope ratio (i.e., $^{87}Sr/^{86}Sr$, $^{143}Nd/^{144}Nd$, $^{176}Hf/^{177}Hf$, $^{206}Pb/^{204}Pb$, $^{207}Pb/^{204}Pb$, $^{208}Pb/^{204}Pb$, $^{187}Os/^{188}Os$, $^{3}He/^{4}He$ and/or $\delta^{18}O$). Trace element data are not filtered based on low-temperature alteration filters (i.e., LOI, Ba/Rb, Ce/Ce*, and Y/Y*). Related plots showing incompatible trace element ratios versus MgO are presented in Supplementary Fig. 8.

3.1.2. Isotope characterization of OIB

In general, OIB data from the database form a positive linear trend in $^{206}Pb/^{204}Pb$-$^{207}Pb/^{204}Pb$, $^{206}Pb/^{204}Pb$-$^{208}Pb/^{204}Pb$, and $^{143}Nd/^{144}Nd$-$^{176}Hf/^{177}Hf$ isotope spaces. By contrast, they display a negative linear trend in $^{87}Sr/^{86}Sr$-$^{143}Nd/^{144}Nd$ isotope space (Fig. 4). When $^{87}Sr/^{86}Sr$, $^{143}Nd/^{144}Nd$, and $^{176}Hf/^{177}Hf$ (not shown) are plotted against $^{206}Pb/^{204}Pb$, no linear trends are formed (Fig. 4c-d). Details of how the isotope data are filtered in each panel are provided in Section 2.2, the Supplementary Text, and briefly summarized in the figure captions. While these relationships are all well established in the literature (e.g., Stracke et al., 2005, 2022; Stracke, 2012; Weis et al., 2011, 2023; Hofmann, 2014; White, 2015), the utility of the new OIBID is that it allows us to, for example, make plots of OIB Pb isotope data that do not show inferior unspiked TIMS Pb isotope data (compare Fig. 4 and Supplementary Fig. 9), or to show radiogenic isotope plots where the global OIB dataset is color coded for a trace element ratio (e.g., Nb/Th, see Supplementary Fig. 10). Furthermore, because these radiogenic isotope plots demonstrate that the new OIBID shows broad geochemical trends that are well known in the literature, we have more confidence that the OIBID can indeed serve as a foundation for exploring isotope geochemistry of the mantle.

As is well-established in the literature (e.g., Kurz et al., 1982; Farley et al., 1992; Graham et al., 1992; Graham, 2002; Class and Goldstein, 2005; White, 2015), helium isotopes fail to exhibit global correlations with heavy radiogenic data (Fig. 5 and Supplementary Fig. 11). EM and HIMU lavas generally have low $^{3}He/^{4}He$ within or below the MORB range (where MORB $^{3}He/^{4}He$ is 8 ± 2 R_A) (Graham, 2002). High $^{3}He/^{4}He$ lavas (> 20 R_A) have geochemically depleted Sr, Nd, and Hf radiogenic isotope compositions and relatively unradiogenic Pb ($^{206}Pb/^{204}Pb < 19.3$) (e.g., Hart et al., 1992; Class and Goldstein, 2005). However, the high $^{3}He/^{4}He$ domain is heterogeneous (Jackson et al., 2007b), and the OIB data form three distinct groups in $^{143}Nd/^{144}Nd$-$^{206}Pb/^{204}Pb$ and $^{206}Pb/^{204}Pb$-$^{208}Pb/^{204}Pb$ isotope spaces (Fig. 5c and Supplementary Fig. 11c). Yet, despite the heavy radiogenic isotope variability in high $^{3}He/^{4}He$ lavas, all high $^{3}He/^{4}He$ lavas have intermediate Sr-Nd-Pb isotope compositions that plot in a relatively narrow range in the OIB field, furthest away from the mantle end member compositions in multi-isotope space (e.g., Hart et al., 1992). However, not all samples located far from the mantle end-members in multi-isotope space have high $^{3}He/^{4}He$ (i.e., even the common component region of multi-isotope space is host to low $^{3}He/^{4}He$ OIB), and thus there is no systematic decrease in $^{3}He/^{4}He$ toward EM and HIMU compositions (Fig. 5a-b). Like plots of $^{3}He/^{4}He$ versus Sr-Nd-Pb-Hf isotopes, $^{187}Os/^{188}Os$ also fails to exhibit clear trends when plotted against other heavy radiogenic isotopes (Fig. 5d and Supplementary Fig. 12).

3.1.3. Isotope composition of OIB as a function of MgO

In Fig. 6 and Supplementary Fig. 13, heavy radiogenic isotope ratios and $^{3}He/^{4}He$ are plotted against MgO, and observations made from these figures are presented here.

3.1.3.1. Nd and Hf isotopes. OIB with the strongest EM signatures (i.e., lowest $^{143}Nd/^{144}Nd$ and $^{176}Hf/^{177}Hf$) tend to have lower MgO (i.e., MgO < 11.2 wt%), and a narrower range of MgO, than OIB with more geochemically depleted isotope compositions (i.e., high $^{143}Nd/^{144}Nd$ and $^{176}Hf/^{177}Hf$) (Fig. 6a-b). For example, all OIB with $^{143}Nd/^{144}Nd < 0.5124$ have MgO < 11.2 wt% and include lavas from the following oceanic hotspots: Conrad, Discovery, Heard-Kerguelen, Pitcairn, Samoa, and Tristan-Gough-Walvis Ridge. Similarly, OIB with $^{176}Hf/^{177}Hf < 0.28265$ have MgO < 11.2 wt% and include the same oceanic hotspots, with the exception of Conrad and Heard-Kerguelen hotspots (note that samples with low $^{143}Nd/^{144}Nd$ (< 0.5124) from these two oceanic hotspots lack Hf isotope data). Put in another way, extreme EM signatures are not found in OIB with the highest MgO. This, relationship is best described by an envelope (see arrows defining envelope in Figs. 6a-b) where, with decreasing MgO, the minimum observed $^{143}Nd/^{144}Nd$ and $^{176}Hf/^{177}Hf$ in OIB also decreases.

One concern emerging from the observation that geochemically enriched (low) $^{143}Nd/^{144}Nd$ and $^{176}Hf/^{177}Hf$ exhibit only low MgO ($<$ 11.2 wt%) (Fig. 6a-b) is that EM signatures are not reflective of the mantle source, but instead result from assimilation of geochemically enriched materials at shallow levels in the oceanic lithosphere. The only abundant material with geochemically enriched $^{143}Nd/^{144}Nd$ and $^{176}Hf/^{177}Hf$ in the oceanic lithosphere is marine sediment. Ocean island volcanoes are constructed on top of any pre-existing marine sediment that veneers the oceanic crust, which opens up the potential for assimilation as magma ascends through the volcano. Marine sediments have high Nd and Pb concentrations (Plank and Langmuir, 1998) compared to OIB, making Nd and Pb isotopes in OIB sensitive to sediment assimilation. Therefore, we expect that, in a plot showing Nd versus Pb isotopes, sediment assimilation in OIB lavas would result in OIB forming arrays that trend toward marine sediment as $^{143}Nd/^{144}Nd$ decreases. However, we find that, in a plot showing $^{143}Nd/^{144}Nd$ versus $\Delta^{208}Pb/^{204}Pb$ (Hart, 1984), global marine sediments from Plank and Langmuir (1998) form a trend that is offset, and diverges away, from global OIB (Fig. 7). This relationship shows that shallow-level assimilation of modern sediments cannot be responsible for generating the extreme EM signatures observed in OIB. However, this relationship does not rule out the possibility that ancient subducted continental materials in the OIB sources generate the modern EM signatures (White and Hofmann, 1982; Eisele et al., 2002; Jackson et al., 2007a). Other possible sources for the EM signatures are delaminated continental lithosphere (McKenzie and O'Nions, 1983), recycled lower continental crust (Willbold and Stracke, 2010), subducted oceanic plateaus (Gasperini et al., 2000), recycled depleted MORB material (Weis et al., 1989), CO_2-fluxed lower mantle (Collerson et al., 2010), metasomatized subcontinental lithospheric mantle (Geldmacher et al., 2008), or recycled Archean carbonates (Wang et al., 2018).

This still leaves unresolved the mechanism responsible for the EM lavas having only low MgO. The observation of lower MgO in geochemically enriched lavas is gaining traction in the literature and is consistent with Shorttle and Maclennan's (2011) results showing that Icelandic lavas with the most enriched geochemical signatures (e.g., high Nb/Zr) have lower MgO than the more geochemically depleted melts. Similarly, Shorttle et al. (2016) showed that geochemically enriched primary MORB melts tend to have lower MgO than depleted primary MORB melts, owing to the former being derived from a more pyroxenitic contribution. If globally applicable, these models may help explain why global OIB with the most extreme EM signatures consistently have low MgO.

3.1.3.2. Sr isotopes. Below 2.0 wt% MgO, $^{87}Sr/^{86}Sr$ in OIB increases dramatically (Fig. 6d). High $^{87}Sr/^{86}Sr$ in evolved OIB have previously been interpreted to be primary signatures (e.g., Ashwal et al., 2016). However, lavas with MgO < 2 wt% have high Rb/Sr due to plagioclase fractionation (Fig. 3a). As a result, such lavas rapidly evolve post-eruptive radiogenic $^{87}Sr/^{86}Sr$, even in relatively young lavas. Therefore, we do not show $^{87}Sr/^{86}Sr$ for lavas with MgO < 2 wt% in other figures in this paper. When this MgO filter is applied (inset in Fig. 6d), the data are permissive of elevated $^{87}Sr/^{86}Sr$ being associated with the mantle sources of relatively low MgO lavas, but the relationship is not as clear as for Hf and Nd isotopes.

3.1.3.3. Pb isotopes. In contrast to Nd and Hf isotopes, Pb isotopes do not exhibit any clear relationships with MgO (Fig. 6c). Both HIMU ($^{206}Pb/^{204}Pb > 21.0$) and non-HIMU lavas exhibit both low and high MgO. For example, HIMU lavas span a wide range of MgO (3–21 wt%), while lavas with unradiogenic $^{206}Pb/^{204}Pb$ of ~18 also span a wide range of MgO, from 1 to 26 wt%. Similar patterns emerge in figures

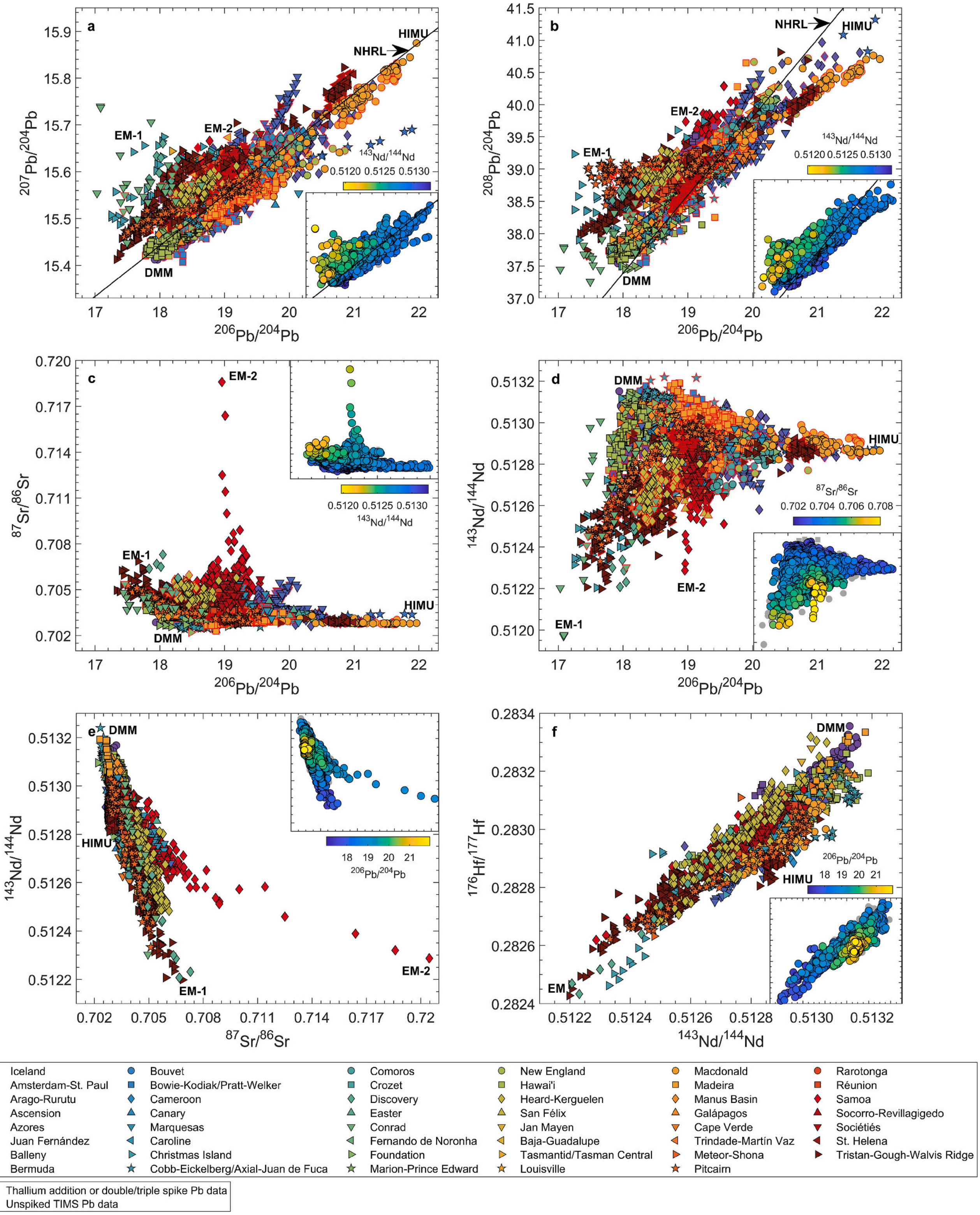

Fig. 4. Isotope characterization of global OIB. a) $^{207}Pb/^{204}Pb$ plotted against $^{206}Pb/^{204}Pb$, b) $^{208}Pb/^{204}Pb$ plotted against $^{206}Pb/^{204}Pb$, c) $^{87}Sr/^{86}Sr$ plotted against $^{206}Pb/^{204}Pb$, d) $^{143}Nd/^{144}Nd$ plotted against $^{206}Pb/^{204}Pb$, e) $^{143}Nd/^{144}Nd$ plotted against $^{87}Sr/^{86}Sr$, and f) $^{176}Hf/^{177}Hf$ plotted against $^{143}Nd/^{144}Nd$. The Northern Hemisphere Reference Line (NHRL; Hart, 1984) is plotted in panels a, and b. $^{87}Sr/^{86}Sr$ data with MgO < 2.0 wt% or no MgO are not shown in the figure. Higher quality unspiked TIMS Pb isotope data are shown in the figure, but the lower quality unspiked TIMS Pb isotope data are not (see Supplementary Text Section 4.3.2.1.). Datapoints showing Pb isotopes measured by thallium-addition method or double/triple-spike method are shown with a black outline; unspiked TIMS Pb data that plot inside a 2σ envelope and inside the range of precise Pb isotope analyses are shown with a red outline. Insets show the isotope data color coded for $^{143}Nd/^{144}Nd$ in panels a, b, and c, $^{87}Sr/^{86}Sr$ in panel d, and $^{206}Pb/^{204}Pb$ in panels e, and f. Grey datapoints in insets lack analyses for the isotope ratio that is used for color coding. Equivalent plots showing only high-precision Pb isotope analyses (i.e., no unspiked TIMS analyses are plotted) are presented in Supplementary Fig. 9. (For interpretation of the references to color in this figure legend, the reader is referred to the web version of this article.)

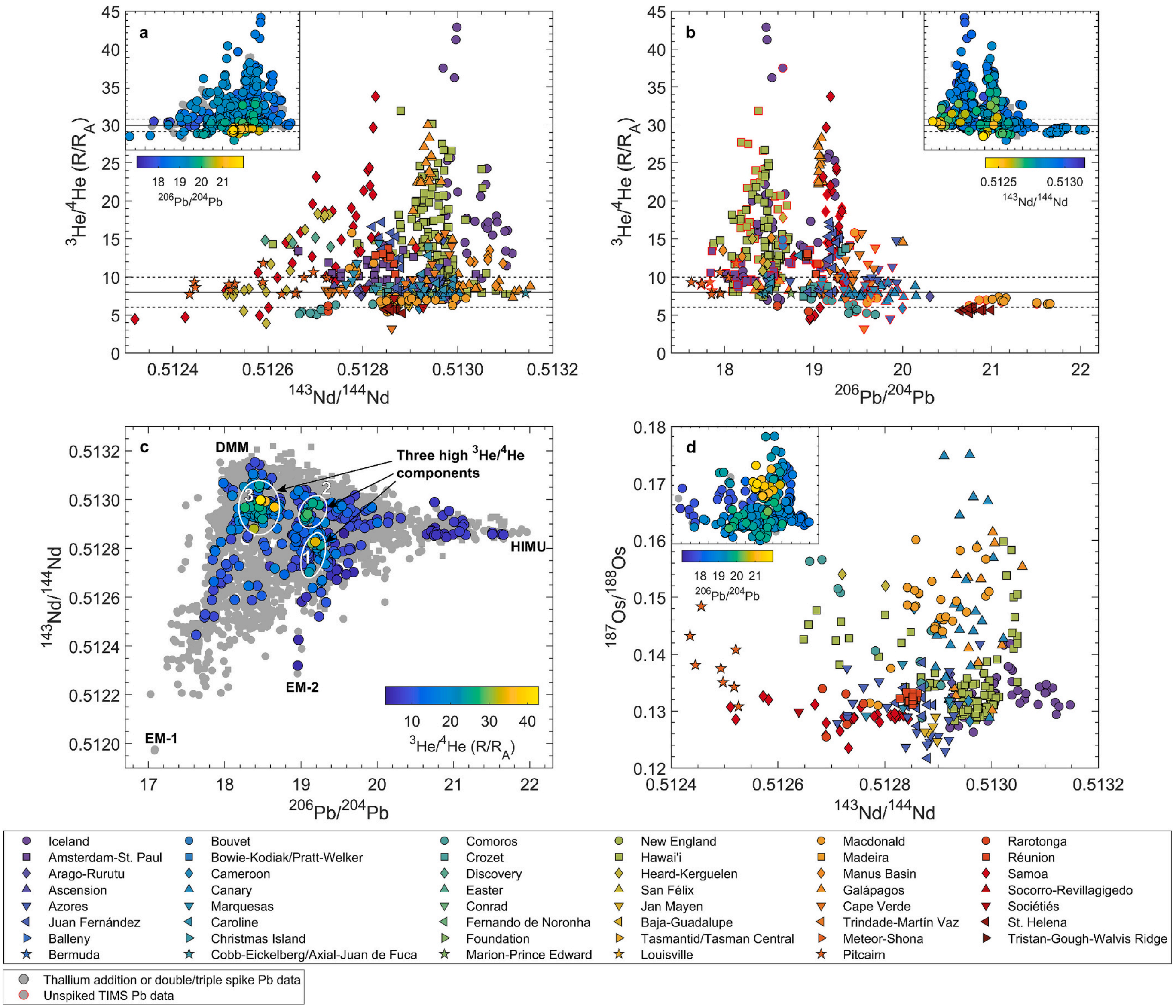

Fig. 5. Helium and osmium isotope systematics in global OIB. a) ^{3}He/^{4}He plotted against ^{143}Nd/^{144}Nd, b) ^{3}He/^{4}He plotted against ^{206}Pb/^{204}Pb, c) ^{143}Nd/^{144}Nd plotted against ^{206}Pb/^{204}Pb color coded for ^{3}He/^{4}He, and d) ^{187}Os/^{188}Os plotted against ^{143}Nd/^{144}Nd. ^{3}He/^{4}He data with [^{4}He] < 90 (gl), < 4 (ol), or < 2 (cpx) ncm^{3}STP/g, and ^{187}Os/^{188}Os data with [Os] < 50 ppt are not shown in the figure. Higher quality unspiked TIMS Pb isotope data are shown in the figure, but the lower quality unspiked TIMS Pb isotope data are not (see Supplementary Text Section 4.3.2.1.). Datapoints showing Pb isotopes measured by thallium-addition method or double/triple-spike method are shown with a black outline; unspiked TIMS Pb data that plot inside a 2σ envelope and inside the range of precise Pb isotope analyses are shown with a red outline. Horizontal black lines in panels a and b show the ^{3}He/^{4}He MORB range (8 ± 2 R$_A$) (Graham, 2002). White ovals in panel c identify the three different high ^{3}He/^{4}He (> 20 R$_A$) groups in global OIB. Insets in panels a and d show the isotope data color coded for ^{206}Pb/^{204}Pb, and ^{143}Nd/^{144}Nd in panel b. Grey datapoints in insets and panel c lack analyses for the isotope ratio that is used for color coding. Other related plots showing ^{3}He/^{4}He and ^{187}Os/^{188}Os versus other radiogenic isotopes are presented in Supplementary Figs. 11–12. (For interpretation of the references to color in this figure legend, the reader is referred to the web version of this article.)

showing ^{207}Pb/^{204}Pb and ^{208}Pb/^{204}Pb (see Supplementary Fig. 13). We do not have an explanation for the lack of relationship between Pb isotopes and MgO, but this may be because Pb isotopes do not correlate with radiogenic isotope indicators of geochemical enrichment (i.e., note the lack of correlation between Nd and Pb isotopes in Fig. 4). Therefore, any relationships between Nd (or Hf) isotopes and MgO are unlikely to be reflected in figures of Pb isotopes versus MgO.

3.1.4. Relationships between trace element ratios and radiogenic isotopes in OIB

To estimate how source heterogeneity is mirrored by trace element variability in OIB, trace element ratios are plotted with ^{143}Nd/^{144}Nd and ^{206}Pb/^{204}Pb (Fig. 8 and Supplementary Figs. 14–15). After applying the alteration filters (i.e., LOI, Ba/Rb, Y/Y*, and Ce/Ce*) and excluding lavas with MgO < 5 wt%, ^{143}Nd/^{144}Nd forms a positive relationship with Nb/Th and a negative relationship with Ba/Nb, demonstrating that EM lavas generally have lower Nb/Th, and higher Ba/Nb, than other OIB (Fig. 8a-b) (e.g., Chauvel et al., 1992; Barling et al., 1994; Willbold and Stracke, 2006; Chauvel et al., 2012), which is consistent with a Nb depletion in EM lavas (e.g., Hofmann et al., 1986; Eisele et al., 2002; Jackson et al., 2007a; Hofmann, 2014).

It has been argued that HIMU is depleted in fluid mobile elements relative to less fluid mobile elements (e.g., Kendrick et al., 2017). To evaluate this, we use ratios of fluid mobile elements (Ba, Pb, Rb, K) to

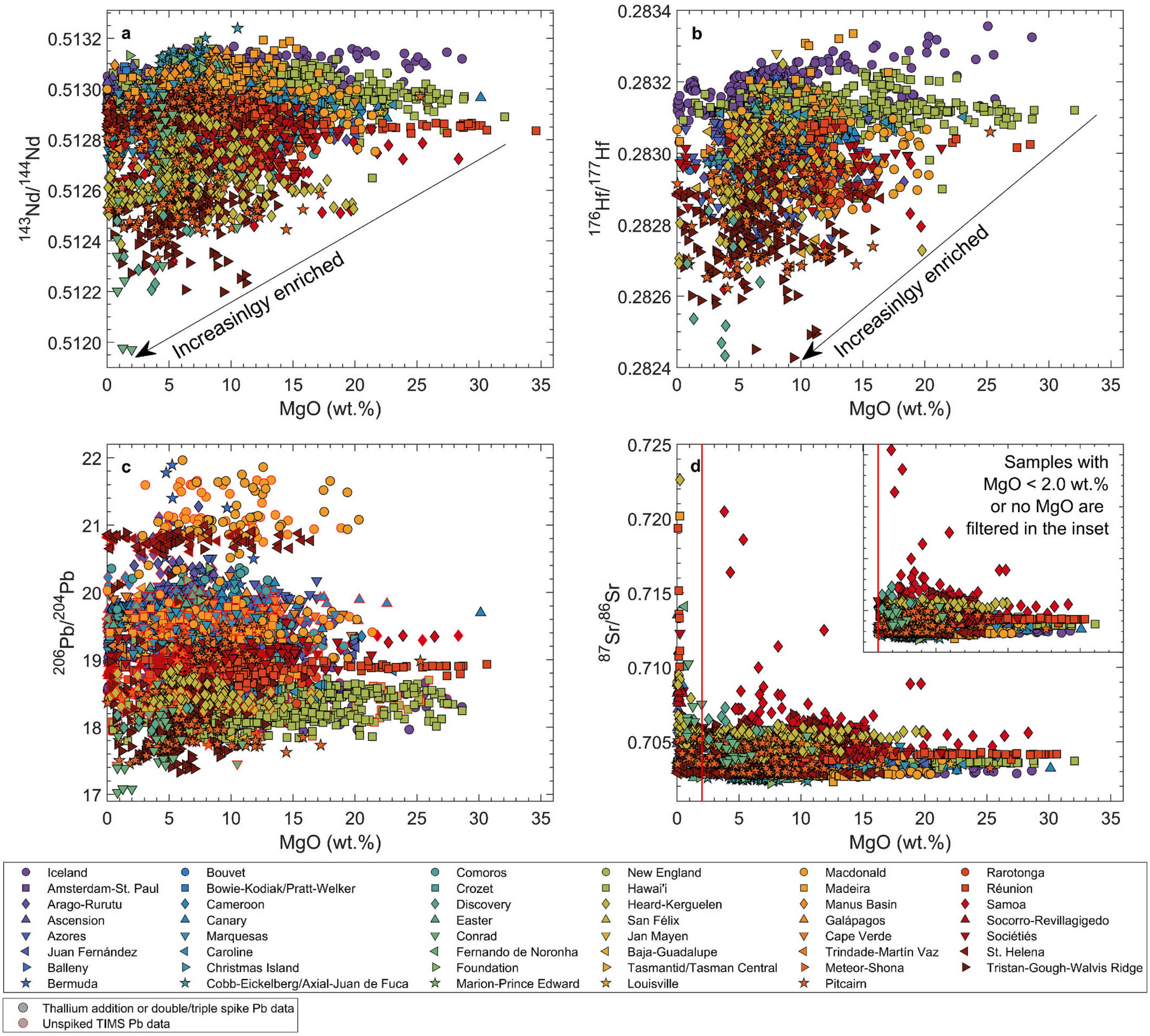

Fig. 6. Isotope ratios plotted against MgO. a) ^{143}Nd/^{144}Nd plotted against MgO, b) ^{176}Hf/^{177}Hf plotted against MgO, c) ^{206}Pb/^{204}Pb plotted against MgO, and d) ^{87}Sr/^{86}Sr plotted against MgO. The vertical red line in panel d shows the MgO threshold of 2.0 wt% that is used to filter ^{87}Sr/^{86}Sr from figures and discussion, and the inset in panel d shows ^{87}Sr/^{86}Sr plotted against MgO when the MgO threshold has been applied. Higher quality unspiked TIMS Pb isotope data are shown in the figure, but the lower quality unspiked TIMS Pb isotope data are not (see Supplementary Text Section 4.3.2.1.). Datapoints showing Pb isotopes measured by thallium-addition method or double/triple-spike method are shown with a black outline; unspiked TIMS Pb data that plot inside a 2σ envelope and inside the range of precise Pb isotope analyses are shown with a red outline. Other related plots showing isotope ratios versus MgO are presented in Supplementary Fig. 13. (For interpretation of the references to color in this figure legend, the reader is referred to the web version of this article.)

less fluid mobile elements (Th, Nb, Ce). A key observation is that the low Pb/Ce, Pb/Th, Rb/Th, Ba/Th, Ba/Nb, and K/Nb ratios found in HIMU lavas (^{206}Pb/^{204}Pb $>$ 21)—indicative of fluid-mobile element depletion—are also found in OIB that have ^{206}Pb/^{204}Pb down to 18.0 (Fig. 8c-d and Supplementary Fig. 15). Thus, a substantial subset of non-HIMU OIB exhibit evidence for depletion in fluid mobile elements, suggesting that fluid-mobile element depletion resulting from subduction zone processes broadly impact HIMU and non-HIMU lithologies contributing to OIB melting. We acknowledge that analyses of these trace elements in fresh submarine glasses (as was the case for Kendrick et al., 2017) is better for avoiding alteration signatures that might impact fluid-mobile element (Ba, Pb, Rb, K) concentrations in whole rock basalt analyses. Nonetheless, the sheer abundance of non-HIMU lavas that, like HIMU lavas, have low ratios of Pb/Ce, Pb/Th, Rb/Th, Ba/Th, Ba/Nb, and K/Nb does suggest that non-HIMU OIB can also exhibit depletion in fluid mobile elements. Finally, we note that the low Ba/Th and Ba/Nb in HIMU lavas is not a consequence of using Ba/Rb as an alteration filter because relationships between Ba/Th, Ba/Nb, and ^{206}Pb/^{204}Pb hold even when the Ba/Rb alteration filter is not used (Supplemententaty Fig. 16).

The OIBID can be used to shed light on previously suggested relationships between trace elements and radiogenic isotopes. In contrast to prior observations, which suggested low K/U in HIMU (Lassiter, 2004; Hanyu et al., 2011), K/U does not clearly correlate with ^{206}Pb/^{204}Pb across global OIB (Supplementary Fig. 15e). Again, the relationship between K/U and ^{206}Pb/^{204}Pb, which uses fluid-mobile trace elements,

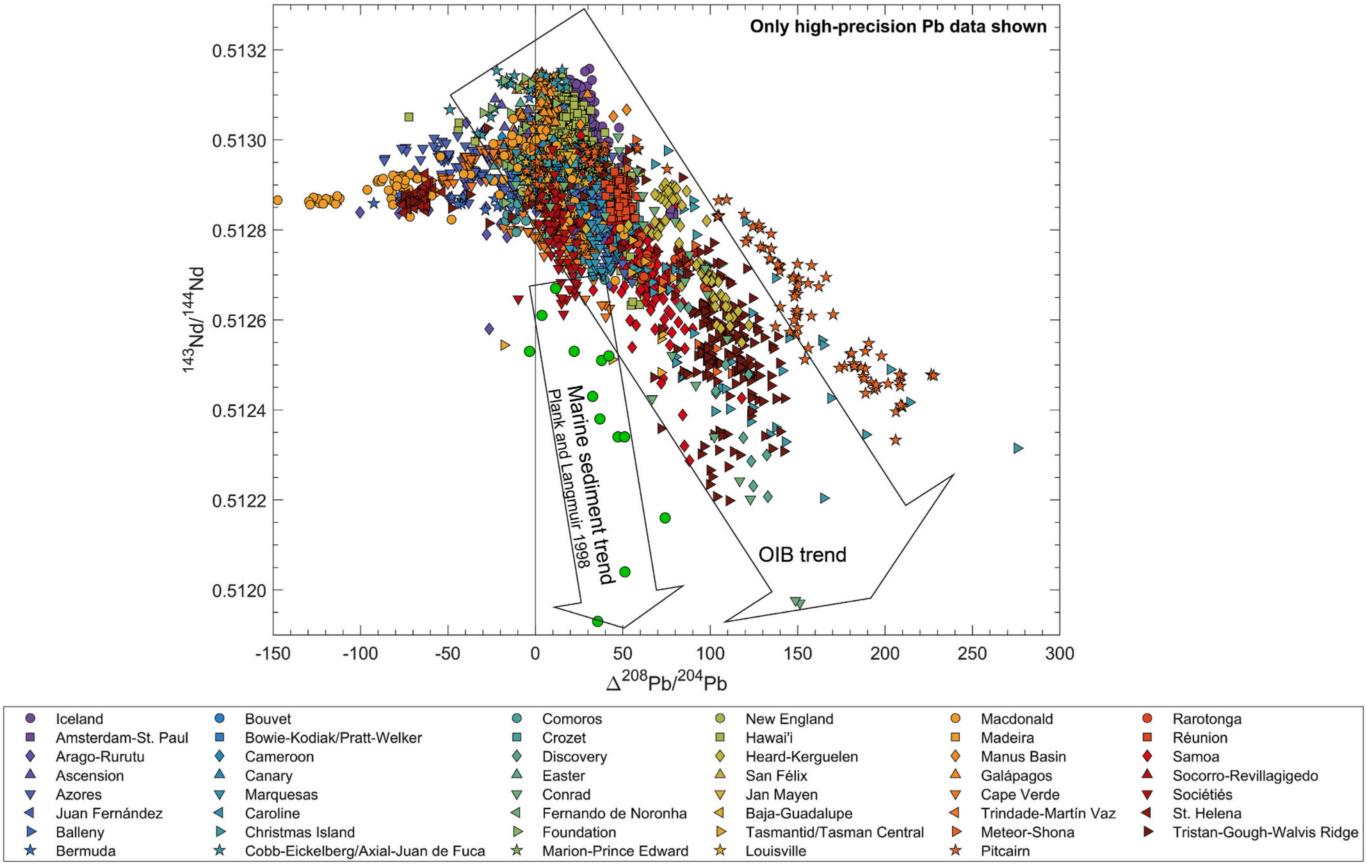

Fig. 7. $^{143}Nd/^{144}Nd$ plotted against $\Delta^{208}Pb/^{204}Pb$ for global OIB and marine sediments from Plank and Langmuir (1998). No unspiked TIMS Pb isotope data are shown in the figure.

would be best evaluated using fresh submarine glass to avoid subtle submarine alteration signatures that might not be fully captured by our alteration filters (i.e., Y/Y*, Ce/Ce*, Ba/Rb, and LOI), but datasets for submarine OIB glass analyses are less complete because OIB glasses are not as commonly analyzed as whole rocks. Nonetheless, the average K/U ratio in the filtered OIBID is 10,667 ± 8893 (2SD), which overlaps with the mean OIB K/U of 12,011 ± 7332 (2SD) determined by Arevalo Jr. et al. (2009).

Additionally, Eu/Eu* does not correlate with $^{206}Pb/^{204}Pb$ in the global OIB dataset (Supplementary Fig. 15f), in contrast to a prior suggestion (Tang et al., 2015). Finally, K_2O/P_2O_5 and Th/U exhibit possible relationships with $^{143}Nd/^{144}Nd$, where lavas with low Th/U and low K_2O/P_2O_5 are associated with high $^{143}Nd/^{144}Nd$ (Supplementary Fig. 14a-b). Such relationships with radiogenic isotopes suggest that Th/U and K_2O/P_2O_5 should not be used as alteration filters (e.g., Pietruszka et al., 2013; Ruttor et al., 2021; Bai et al., 2022) as they may exhibit variability related to the mantle source.

3.1.5. *Mantle end-member classification based on trace elements*

Some of the trace element ratios described above can be used to resolve EM lavas from HIMU lavas. For example, the Nb depletion in EM lavas relative to other OIB—resulting from a Nb-depleted continental crust contribution in EM lavas—results in low Nb/Th and high Ba/Nb in EM lavas (Fig. 8). Therefore, a plot of Ba/Nb versus Nb/Th (Fig. 9) shows that EM lavas (with low $^{143}Nd/^{144}Nd$) plot in the upper left portion of the global OIB array, while HIMU lavas (with high $^{206}Pb/^{204}Pb$) plot in the lower right portion. While we do not make an attempt to comprehensively resolve EM and HIMU lavas across the full range of possible trace element compositions discussed in the prior section, this example serves as a template for identifying trace element differences between the mantle end-members, which is a long-standing effort in the community (e.g., Weaver, 1991; Willbold and Stracke, 2006)

3.2. *Geochemically-extreme OIB—EM, HIMU, and high $^3He/^4He$ lavas—are rare*

The existing OIB literature focuses heavily on compositionally extreme OIB (i.e., EM, HIMU, and high $^3He/^4He$ compositions) (e.g., Woodhead, 1996; Workman et al., 2004; Gibson et al., 2005; Hanyu et al., 2011; Homrighausen et al., 2018). This focus is understandable, as the most compositionally extreme OIB give important insights into the origins of the different end-members of the mantle. However, these mantle end-members are volumetrically minor components (e.g., Stracke et al., 2003; Sobolev et al., 2007) and may therefore not be representative of the OIB mantle source. This section attempts to place the relative abundance of geochemically-extreme OIB in context of global OIB magma genesis.

Neodymium isotopes are useful for constraining the long-term geochemical enrichment (or depletion) of silicate Earth reservoirs, and Fig. 10a shows that oceanic hotspot lavas with geochemically enriched (low) $^{143}Nd/^{144}Nd$ are relatively uncommon. Of the 47 oceanic hotspots with $^{143}Nd/^{144}Nd$ data, just 16 oceanic hotspots (i.e., 34 % of the oceanic hotspots characterized for $^{143}Nd/^{144}Nd$) have at least one geochemically enriched lava with $^{143}Nd/^{144}Nd < 0.512630$ (where 0.512630 represents the chondrite value, which is the threshold for distinguishing long-term geochemical enrichment or depletion) (Bouvier et al., 2008). Similarly, only 7.2 % of all $^{143}Nd/^{144}Nd$ analyses in the OIBID have $^{143}Nd/^{144}Nd < 0.512630$, indicative of the relative rarity of geochemically enriched domains in OIB. In summary, 66 % of the characterized oceanic hotspots do not have a single lava with geochemically enriched $^{143}Nd/^{144}Nd$, and 92.8 % of all $^{143}Nd/^{144}Nd$ analyses in the OIBID reflect geochemically depleted compositions

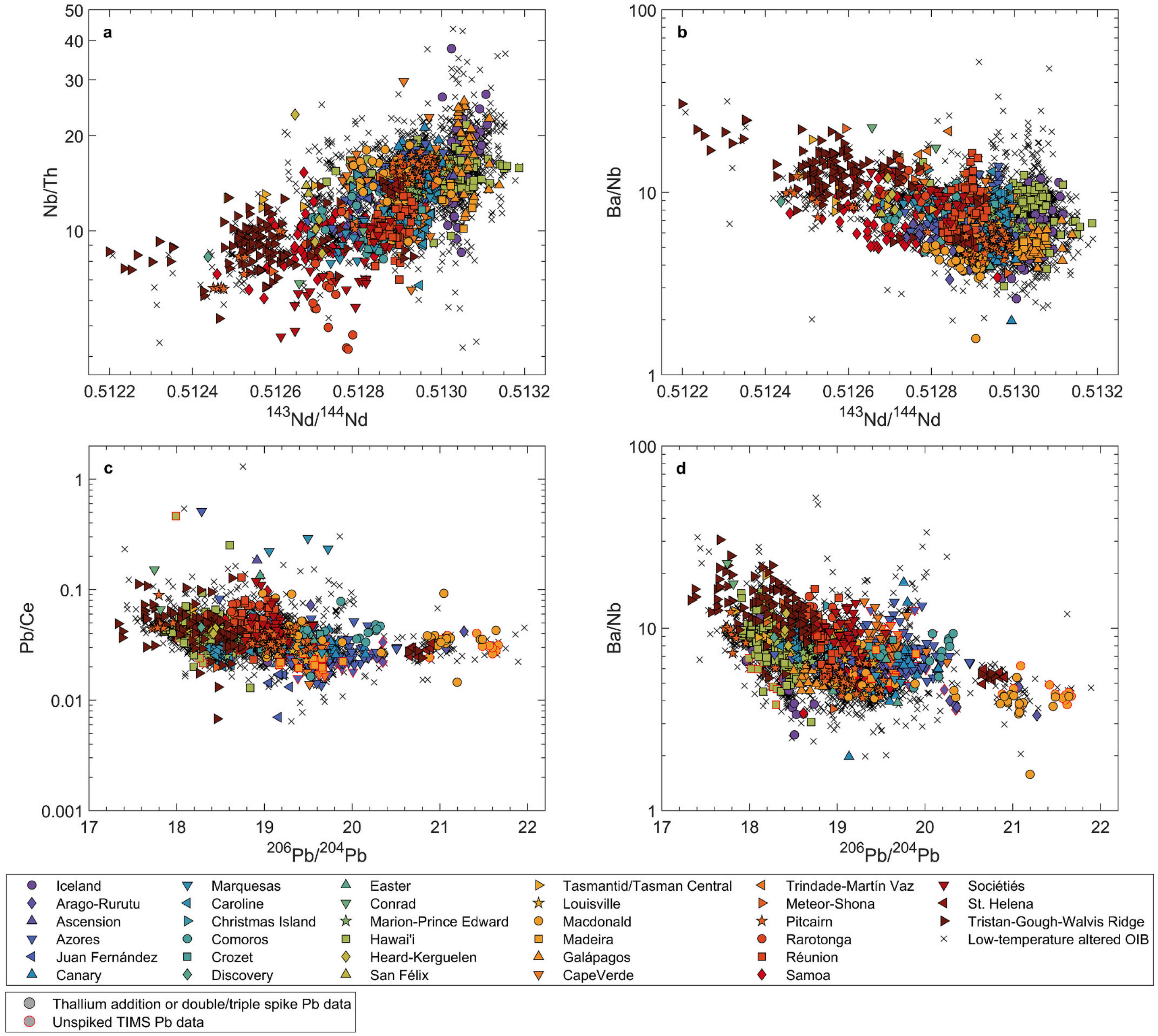

Fig. 8. Trace element ratios plotted against neodymium and lead isotopes. a) Nb/Th plotted against ^{143}Nd/^{144}Nd, b) Ba/Nb plotted against ^{143}Nd/^{144}Nd, c) Pb/Ce plotted against ^{206}Pb/^{204}Pb, and d) Ba/Nb plotted against ^{206}Pb/^{204}Pb. Higher quality unspiked TIMS Pb isotope data are shown in the figure, but the lower quality unspiked TIMS Pb isotope data are not (see Supplementary Text Section 4.3.2.1.). Datapoints showing Pb isotopes measured by thallium-addition method or double/triple-spike method are shown with a black outline; unspiked TIMS Pb data that plot inside a 2σ envelope and inside the range of precise Pb isotope analyses are shown with a red outline. Only trace element data measured by ICP-MS on samples with MgO ≥ 5 wt% are plotted in the figure. Black "x" symbols show data filtered based on low-temperature alteration filters (i.e., LOI > 4 wt%, Ba/Rb < 6 or > 50, Ce/Ce* < 0.8 or > 1.2, or Y/Y* < 0.7 or > 1.3). Other related plots showing trace element ratios versus ^{143}Nd/^{144}Nd and ^{206}Pb/^{204}Pb are presented in Supplementary Fig. 14–16. (For interpretation of the references to color in this figure legend, the reader is referred to the web version of this article.)

(Fig. 10a). Similarly, only 6.1 % of ^{176}Hf/^{177}Hf analyses in global OIB are geochemically enriched and fall below the chondritic value of 0.282785 (Bouvier et al., 2008) (Supplementary Fig. 17b). Thus, ^{143}Nd/^{144}Nd and ^{176}Hf/^{177}Hf data indicate that the OIB mantle is dominantly depleted geochemically, not enriched (e.g., Stracke et al., 2022). This is in line with the early observation that the most common Nd-isotope composition sampled by hotspots, referred to as PREMA, has ^{143}Nd/^{144}Nd close to 0.5130 (Zindler and Hart, 1986), a value that is closer to the average ^{143}Nd/^{144}Nd for MORB (0.513083; Gale et al., 2013) than it is to the chondrite average (0.512630; Bouvier et al., 2008).

If EM signatures (i.e., low ^{143}Nd/^{144}Nd and low ^{176}Hf/^{177}Hf) result primarily from subduction of continental crust materials (White and Hofmann, 1982), then the relatively rarity of OIB with EM signatures could result from the relatively small mass of continental crust subducted compared to oceanic crust, particularly if continental crust has been subducting for a much shorter period of time than oceanic crust (Condie, 2021; Jackson and Macdonald, 2022). While this is partially offset by higher incompatible trace element concentration in subducted continental crust compared to oceanic crust and ambient mantle, EM compositions may be even more rare in the mantle than indicated by their distribution in OIB lavas (e.g., Stracke, 2021). This is because volumetrically minor enriched lithologies are often more fusible (e.g., Pertermann and Hirschmann, 2003; Kogiso et al., 2004; Ito and

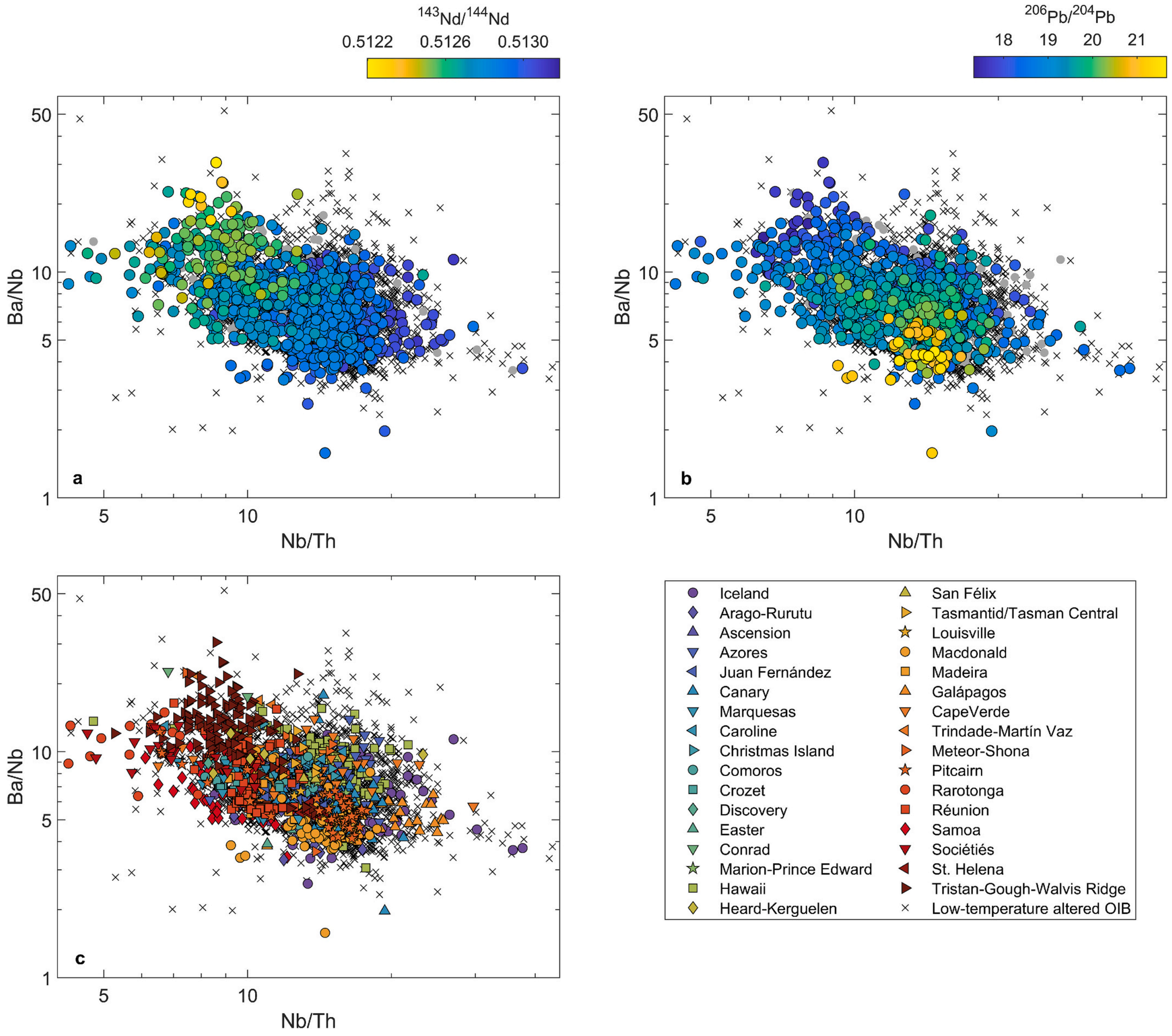

Fig. 9. Ba/Nb plotted against Nb/Th. a) Data are color coded for $^{143}Nd/^{144}Nd$ where the lowest $^{143}Nd/^{144}Nd$ ratios are shown at the front, and b) data are color coded for $^{206}Pb/^{204}Pb$ where the highest $^{206}Pb/^{204}Pb$ ratios are shown at the front, and c) the various oceanic hotspots are shown with different symbols. Higher quality unspiked TIMS Pb isotope data are shown in the figure, but the lower quality unspiked TIMS Pb isotope data are not (see Supplementary Text Section 4.3.2.1.). The figure shows only trace element data measured by ICP-MS for OIB with MgO ≥ 5 wt% from the database. Black "x" symbols show data filtered based on low-temperature alteration filters (i.e., LOI > 4 wt%, Ba/Rb < 6 or > 50, Ce/Ce* < 0.8 or > 1.2, or Y/Y* < 0.7 or > 1.3).

Mahoney, 2005), and thus more likely to survive magma differentiation processes, a mechanism that will bias the OIB data toward enriched compositions (e.g., Neave et al., 2019). Similarly, depleted signatures in OIB are most likely undersampled relative to their abundance in the mantle source (e.g., Stracke et al., 2019). As a result, the *mantle sources* of OIB may be even more geochemically depleted (i.e., have even higher $^{143}Nd/^{144}Nd$ and $^{176}Hf/^{177}Hf$), on average, than indicated by distributions showing Nd and Hf isotopes in OIB (see Fig. 12 and Supplementary Fig. 20).

If we adopt a $^{206}Pb/^{204}Pb$ threshold of 21.0 for defining HIMU lavas, then only 3 of the 47 oceanic hotspots with Pb isotope data—Macdonald, Bermuda, and Arago-Rurutu, representing just 6 % of the oceanic hotspots characterized for $^{206}Pb/^{204}Pb$—have at least one lava with a HIMU composition (Fig. 10b). Additionally, only ~1.3 % of all lavas in the OIBID with Pb isotopes analyzed have $^{206}Pb/^{204}Pb \geq 21$. If the threshold $^{206}Pb/^{204}Pb$ for HIMU is lowered to 20.5, then 8 of the 47 oceanic hotspots with Pb isotope data (or 17 % of the oceanic hotspots characterized for $^{206}Pb/^{204}Pb$) have at least one lava with a HIMU signature, and only 3.4 % of all lavas in the OIBID with Pb isotopes analyzed have HIMU compositions. This apparent paucity of HIMU lavas may actually be reflective of the mass of recycled oceanic crust that has entered the mantle over geologic time. For example, Rudnick et al. (2000) estimate that the minimum mass of oceanic crust subducted through Earth history is equal to 3.3 % of the mass of the silicate Earth. If HIMU lavas are melts that sample a component of recycled oceanic crust, then the percentage of HIMU lavas in the OIBID (3.4 %) is similar to the fraction of the mantle's mass that consists of subducted oceanic crust (3.3 %). In this light, the small proportion of HIMU lavas in the OIBID may reflect the relatively small proportion of the mantle composed of subducted oceanic crust. However, it has been suggested that recycled crustal materials in the mantle are more fusible than the surrounding peridotite (e.g., Pertermann and Hirschmann, 2003; Kogiso

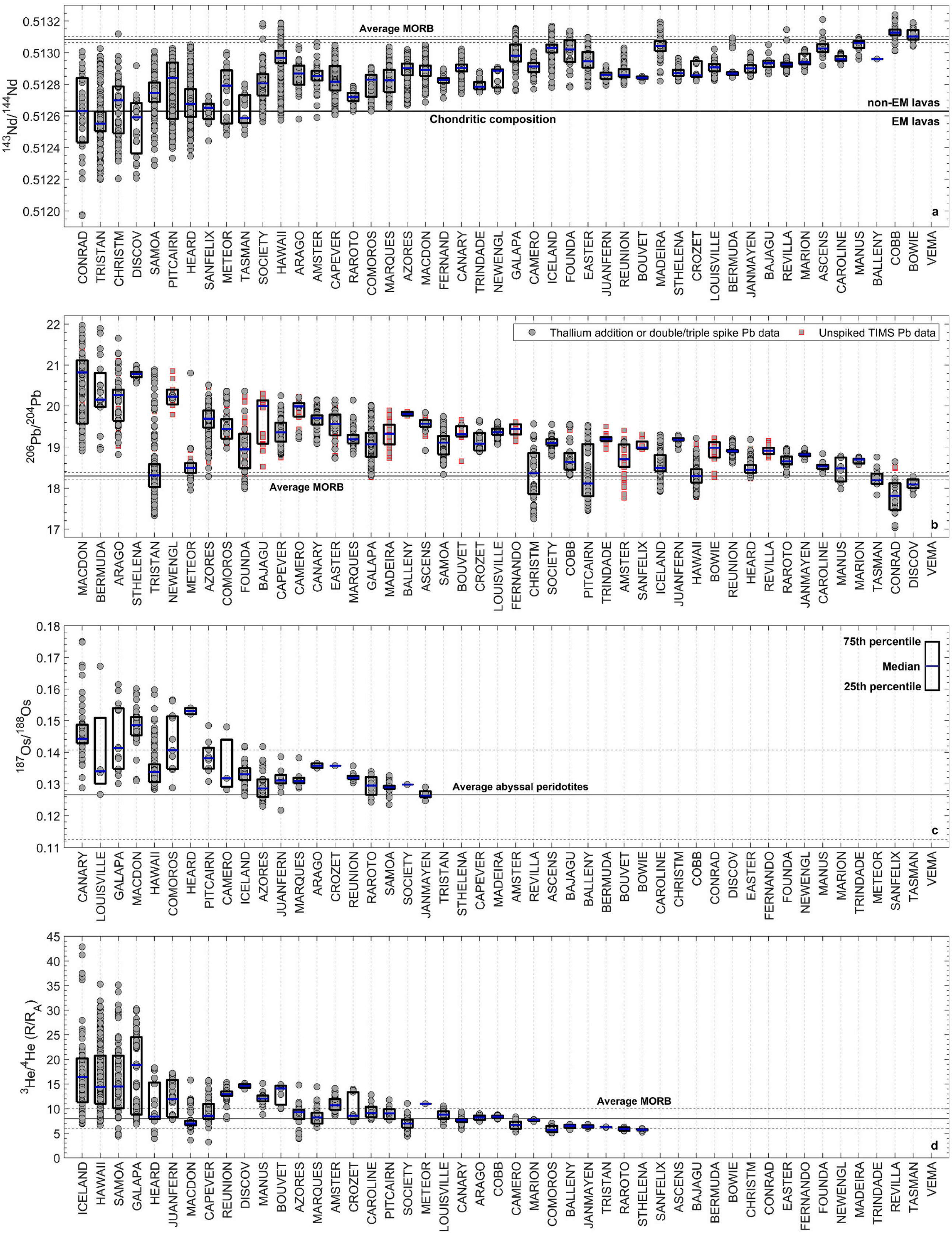

(caption on next page)

Fig. 10. Isotope range identified in samples at each oceanic hotspot for a) ^{143}Nd/^{144}Nd, b) ^{206}Pb/^{204}Pb, c) ^{187}Os/^{188}Os, and d) ^{3}He/^{4}He. Hotspots are ordered from left to right based on the lowest ^{143}Nd/^{144}Nd in panel a, highest ^{206}Pb/^{204}Pb in panel b, highest ^{187}Os/^{188}Os in panel c, and highest ^{3}He/^{4}He in panel d. The black boxes represent data within the 25th and 75th percentile with the median shown as a blue line. ^{187}Os/^{188}Os with [Os] $<$ 50 ppt, and ^{3}He/^{4}He with [^{4}He] $<$ 90 ncm^{3}STP/g (gl), $<$ 4 ncm^{3}STP/g (ol), and $<$ 2 ncm^{3}STP/g (cpx) are not shown in the figure. Higher quality unspiked TIMS Pb isotope data are shown in the figure, but the lower quality unspiked TIMS Pb isotope data are not (see Supplementary Text Section 4.3.2.1.). Datapoints showing Pb isotopes measured by thallium-addition method or double/triple-spike method are shown with a black outline; unspiked TIMS Pb data that plot inside a 2σ envelope and inside the range of precise Pb isotope analyses are shown with a red outline. Hotspot short names that are used on the x-axis are identified in Table 1. Average MORB composition and 2σ from Gale et al. (2013) (for ^{143}Nd/^{144}Nd and ^{206}Pb/^{204}Pb) and Graham (2002) (for ^{3}He/^{4}He) are shown with grey horizontal lines. Average abyssal peridotites and 2σ compiled in Paquet et al. (2022) (for ^{187}Os/^{188}Os) are shown with grey horizontal lines. Black horizontal line in panel a shows the chondritic composition (^{143}Nd/^{144}Nd = 0.512630) (Bouvier et al., 2008). Other related plots including ^{87}Sr/^{86}Sr, ^{176}Hf/^{177}Hf, ^{207}Pb/^{204}Pb and ^{208}Pb/^{204}Pb are presented in Supplementary Fig. 17; Supplementary Fig. 18 shows isotope data that is lost in the filtering process, and not shown in Fig. 10 and Supplementary Fig. 17. (For interpretation of the references to color in this figure legend, the reader is referred to the web version of this article.)

et al., 2004; Ito and Mahoney, 2005) which should result in oversampling of melts of recycled crustal materials such as HIMU melts. This would make the HIMU end-member even rarer in the mantle source than indicated by the sampling frequency in the OIBID.

The new OIBID also provides insights into the hypothesized prevalence of high ^{3}He/^{4}He in global OIB. Analyses of ^{3}He/^{4}He in MORB show that MORB have ^{3}He/^{4}He of 8 ± 2 R_A (2σ) (Graham, 2002). Thus, OIB that have ^{3}He/^{4}He $>$ 10 R_A are considered to have "higher-than-MORB" ^{3}He/^{4}He. Of the 32 oceanic hotspots that have ^{3}He/^{4}He data with sufficiently high helium concentrations to be included in the OIBID, 21 oceanic hotspots (or 66 % of the oceanic hotspots characterized for ^{3}He/^{4}He) have ^{3}He/^{4}He $>$ 10, and 57 % of OIB lavas with ^{3}He/^{4}He analyses have values greater than 10 R_A (Fig. 10d). Thus, 11 oceanic hotspots (or 34 % of the oceanic hotspots characterized for ^{3}He/^{4}He) fail to exhibit a single lava with ^{3}He/^{4}He above the MORB range, and 43 % of individual OIB ^{3}He/^{4}He analyses have values within, or below, the MORB range. Breaking this down further, 38 % of the individual OIB ^{3}He/^{4}He analyses lie within the MORB range (i.e., 8 ± 2 R_A), and 5 % have ^{3}He/^{4}He analyses below the MORB range ($<$ 6 R_A). The important point here is that it is not entirely correct to say that OIB have higher ^{3}He/^{4}He than MORB because a relatively large fraction of oceanic hotspots (11 out of 32, or 34 %) and individual OIB ^{3}He/^{4}He analyses (43 %) do not.

Lavas with very high ^{3}He/^{4}He are rare. If we adopt 20 R_A as the threshold value for "very high" ^{3}He/^{4}He, then only 4 oceanic hotspots (or 12.5 % of oceanic hotspots characterized for ^{3}He/^{4}He) in the OIBID—Iceland, Hawai'i, Galápagos, and Samoa—have samples that achieve this threshold (Fig. 10d). We note that ^{3}He/^{4}He of 25 R_A is reported for the Easter hotspot, but helium concentrations are not yet available (Stroncik et al., 2011). Yellowstone is a continental hotspot, which is thus excluded from the database, but ^{3}He/^{4}He $>$ 20 R_A have been reported for this hotspot (Licciardi et al., 2001; Abedini et al., 2006; Graham et al., 2009). Similarly, the Afar hotspot approaches 20 R_A (19.6 R_A; Marty et al., 1996), but is excluded because it erupted in a continental setting. (As continental crust has low ^{3}He/^{4}He and high ^{4}He concentrations, the high ^{3}He/^{4}He values of hotspot lavas erupted in continental setting may be impacted by crustal assimilation and will not reflect the mantle source.) Focusing only on the oceanic lavas in the OIBID that have helium concentrations above the threshold value, just 15 % of individual OIB ^{3}He/^{4}He analyses have ^{3}He/^{4}He $>$ 20 R_A, confirming that very high ^{3}He/^{4}He ratios are uncommon in OIB.

If high ^{3}He/^{4}He mantle represent mantle domains "less modified" by subduction of crust (White, 2015), then a corollary to this hypothesis is that the rarity of high ^{3}He/^{4}He in OIB is a result of this signature having been widely overprinted by subducted crustal materials (e.g., Hanyu and Kaneoka, 1997; Moreira and Kurz, 2001; Class and Goldstein, 2005; Jackson et al., 2020). Subducted crust has high U and Th concentrations, and thus evolves high ^{4}He concentrations and low ^{3}He/^{4}He over time, so it may have significantly higher ^{4}He concentrations than high ^{3}He/^{4}He mantle domains, which would make high ^{3}He/^{4}He domains highly susceptible to being overprinted by low ^{3}He/^{4}He. As a result, it is possible that even minor amounts of subducted crust—perhaps too low to be easily resolved using lithophile radiogenic isotopes—could be ubiquitous in the mantle and have a devastating impact on the survival of high ^{3}He/^{4}He domains. In this model, high ^{3}He/^{4}He mantle domains were more prevalent early in Earth history, before widespread crustal subduction impacted the geochemistry of the mantle. In this light, high ^{3}He/^{4}He mantle domains in the modern mantle now constitute an "endangered species" that have survived in an aging, dynamic mantle.

3.3. Sampling bias in the radiogenic isotope OIB dataset that overrepresents a small number of oceanic hotspots

3.3.1. Isotope analyses across global oceanic hotspots are biased toward a small number of hotspots and provide an incomplete picture of the mantle

The observations above are limited by the fact that radiogenic isotope analyses available in the OIBID are highly biased, which we explore here.

Multiple oceanic hotspots lack isotope data either because no (or very few) isotope analyses have been performed at a given hotspot, and/or because isotope analyses are removed from consideration in the filtering process (e.g., ^{87}Sr/^{86}Sr with low or no MgO, lower quality unspiked TIMS Pb-isotope data, ^{187}Os/^{188}Os with low [Os], ^{3}He/^{4}He with low [^{4}He]). In contrast, some oceanic hotspots have an abundance of isotope data, even after data filtering (Fig. 11 and Supplementary Fig. 19). As a result, the available isotope data in the OIBID are highly biased toward a relatively small number of the 48 known oceanic hotspots.

Fig. 10 and Supplementary Fig. 17 show the isotope range, and median, for Sr-Nd-Pb-Hf-Os-He isotopes at each oceanic hotspot. ^{143}Nd/^{144}Nd and ^{206}Pb/^{204}Pb analyses are available for 47 out of 48 oceanic hotspots (i.e., no isotope analyses are available for the Vema hotspot). For eight oceanic hotspots (i.e., Baja-Guadalupe, Balleny, Bowie-Kodiak/Pratt-Welker, Fernando de Noronha, Madeira, San Félix, Socorro-Revillagigedo, and Trindade-Martín Vaz) only unspiked TIMS lead isotope analyses are available, and for several other oceanic hotspots the majority of the lead isotope analyses have been measured with unspiked TIMS methods (e.g., Amsterdam-St. Paul, Ascension, Bouvet, Cameroon, Easter, and New England) (see Fig. 10b and Table 3). Looking forward, it will be important to measure lead isotope ratios with modern analytical techniques that are more precise and accurate (e.g., Jackson et al., 2014; Taylor et al., 2015; Cordier et al., 2016) at these hotspots.

^{87}Sr/^{86}Sr analyses are available for 46 out of 48 oceanic hotspots (Supplementary Fig. 17a). Again, no isotope analyses are available for the Vema hotspot and all ^{87}Sr/^{86}Sr analyses from Christmas Island are filtered from figures and discussion because no MgO concentrations are reported for the lavas with reported ^{87}Sr/^{86}Sr. A large number (N = 3244) of Sr isotope analyses are filtered from figures because the host rocks have no MgO or MgO $<$ 2 wt% (and these filtered lavas are shown with an "x" symbol in Supplementary Fig. 18a).

^{176}Hf/^{177}Hf analyses are available for 33 out of 48 oceanic hotspots (Supplementary Fig. 17b), but 15 oceanic hotspots (i.e., Balleny, Bowie-Kodiak/Pratt-Welker, Comoros, Conrad, Crozet, Fernando de Noronha, Foundation, Juan Fernández, Manus Basin, Marion-Prince Edward, New England, San Félix, Socorro-Revillagigedo, Trindade-Martín Vaz, and

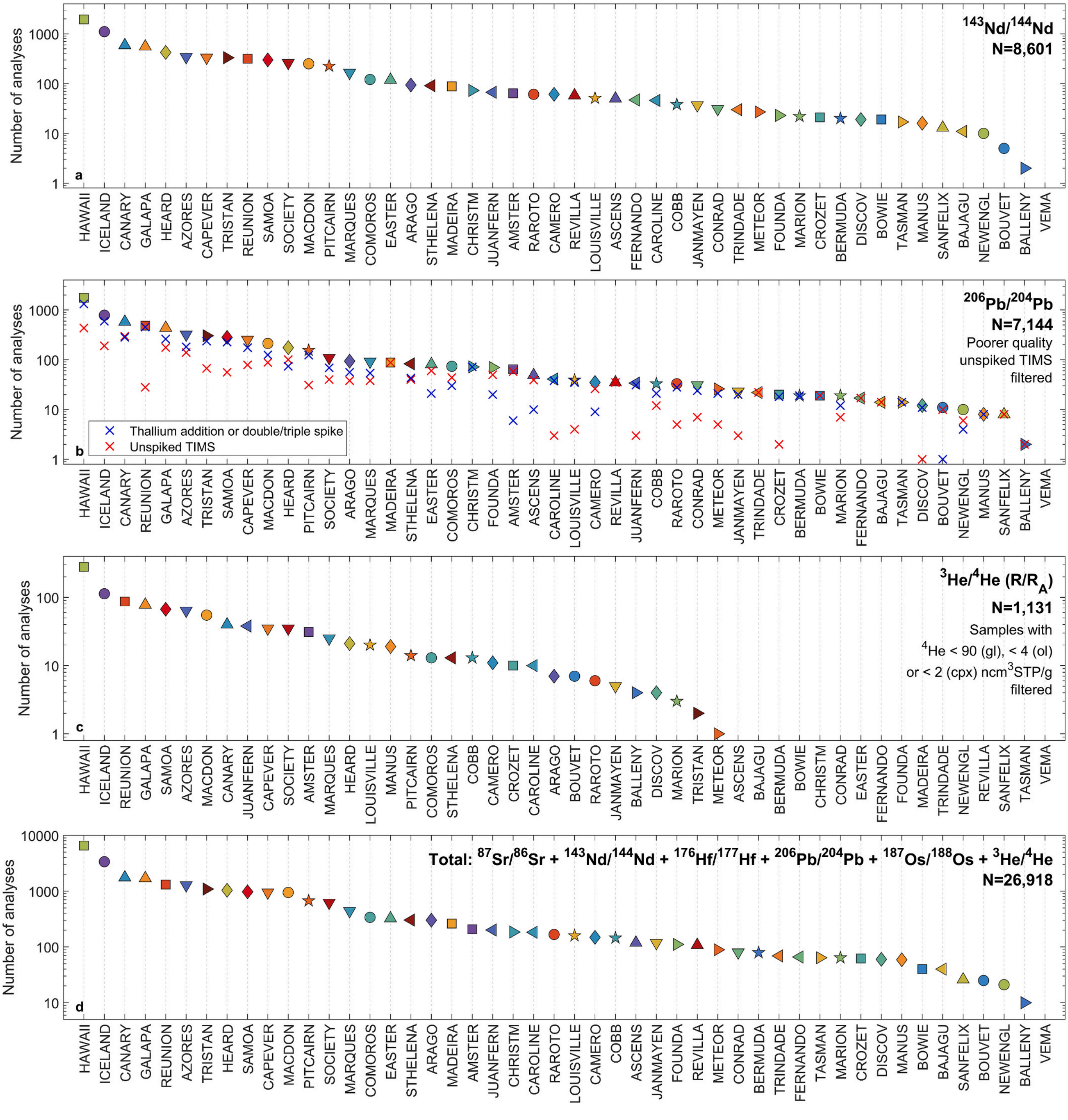

Fig. 11. Number of analyses in the filtered OIBID for different isotope systems. a) ^{143}Nd/^{144}Nd, b) ^{206}Pb/^{204}Pb, c) ^{3}He/^{4}He, and d) total number of analyses for ^{87}Sr/^{86}Sr, ^{143}Nd/^{144}Nd, ^{176}Hf/^{177}Hf, ^{206}Pb/^{204}Pb, ^{187}Os/^{188}Os, and ^{3}He/^{4}He. Lower quality unspiked TIMS Pb isotope data (see Supplementary Text Section 4.3.2.1.), and ^{3}He/^{4}He with [^{4}He] < 90 ncm^{3}STP/g (gl), < 4 ncm^{3}STP/g (ol), and < 2 ncm^{3}STP/g (cpx) are not shown in the figure. While lower quality unspiked TIMS Pb isotope data are excluded from panel b, the higher quality unspiked TIMS Pb data (red "x" symbols) are shown separately from Pb isotopes measured by Tl-addition and double/triple spike methods (blue "x" symbols). Hotspot short names that are used on the x-axis are identified in Table 1. Other related plots showing ^{87}Sr/^{86}Sr, ^{176}Hf/^{177}Hf and ^{187}Os/^{188}Os are presented in Supplementary Fig. 19.

Vema) still lack Hf isotope analyses by MC-ICP-MS.

^{3}He/^{4}He analyses with [^{4}He] above the threshold value are available for 32 out of 48 oceanic hotspots (Fig. 10d). 15 oceanic hotspots still lack ^{3}He/^{4}He analyses (i.e., Ascension, Baja-Guadalupe, Bermuda, Bowie-Kodiak/Pratt-Welker, Christmas Island, Conrad, Easter, Fernando de Noronha, Foundation, Madeira, New England, Socorro-Revillagigedo, Tasmantid-Tasman Central, Trindade-Martín Vaz, and Vema), and the single ^{3}He/^{4}He datum for San Félix is not included in figures and is excluded from discussion because of a low helium concentration (Supplementary Fig. 18d). Thus, 16 out of 48 oceanic hotspots (i.e., 33 % of known OIB hotspots) lack reliable ^{3}He/^{4}He data.

^{187}Os/^{188}Os analyses with [Os] above the 50 ppt threshold are available for 20 out of 48 oceanic hotspots (Fig. 10c). ^{187}Os/^{188}Os analyses are reported for another six oceanic hotspots (i.e., Amsterdam-St.

Table 3
Number of analyses for different radiogenic isotope systems at each oceanic hotspot following filtering and exclusion of data (as outlined in Table 2).

#	Short name	^{87}Sr/^{86}Sr	^{143}Nd/^{144}Nd	^{176}Hf/^{177}Hf	^{206}Pb/^{204}Pb total	Unspiked TIMS	High-precision	^{187}Os/^{188}Os	^{3}He/^{4}He	Total
1	AMSTER	28	64	20	64	58	6	0	31	207
2	ARAGO	55	94	50	94	38	56	2	7	302
3	ASCENS	16	50	4	49	39	10	0	0	119
4	AZORES	335	343	187	322	140	182	28	64	1279
5	BAJAGU	8	11	7	14	14	0	0	0	40
6	BALLENY	2	2	0	2	2	0	0	4	10
7	BERMUDA	20	20	20	19	0	19	0	0	79
8	BOUVET	1	5	1	11	10	1	0	7	25
9	BOWIE	2	19	0	19	19	0	0	0	40
10	CAMERO	30	61	9	35	26	9	3	11	149
11	CANARY	443	591	43	579	297	282	58	40	1754
12	CAPEVER	272	333	54	254	79	175	0	35	948
13	CAROLINE	50	46	36	41	3	38	0	10	183
14	CHRISTM	0	73	40	72	0	72	0	0	185
15	COBB	45	38	16	33	12	21	0	13	145
16	COMOROS	120	121	0	74	44	30	11	13	339
17	CONRAD	18	31	0	31	7	24	0	0	80
18	CROZET	10	21	0	20	2	18	1	10	62
19	DISCOV	10	19	15	12	1	11	0	4	60
20	EASTER	91	119	33	81	60	21	0	0	324
21	FERNANDO	2	47	0	17	17	0	0	0	66
22	FOUNDA	18	23	0	70	50	20	0	0	111
23	GALAPA	505	555	112	437	176	261	14	78	1701
24	HAWAII	1462	1948	943	1753	434	1319	159	280	6545
25	HEARD	250	423	166	175	101	74	2	21	1037
26	ICELAND	889	1107	435	785	190	595	39	113	3368
27	JANMAYEN	29	37	19	23	3	20	5	5	118
28	JUANFERN	49	67	0	34	3	31	13	38	201
29	LOUISVILLE	42	51	3	39	4	35	4	20	159
30	MACDON	215	251	177	213	88	125	36	55	947
31	MADEIRA	68	88	19	88	88	0	0	0	263
32	MANUS	16	16	0	8	0	8	0	19	59
33	MARION	20	22	0	19	7	12	0	3	64
34	MARQUES	115	166	34	92	38	54	9	25	441
35	METEOR	15	27	20	26	5	21	0	1	89
36	NEWENGL	1	10	0	10	6	4	0	0	21
37	PITCAIRN	175	225	93	155	31	124	9	14	671
38	RAROTO	31	61	28	33	5	28	8	6	167
39	REUNION	326	315	74	483	28	455	23	87	1308
40	SAMOA	232	299	65	283	56	227	25	67	971
41	SANFELIX	5	13	0	8	8	0	0	0	26
42	SOCIETY	143	261	71	109	40	69	1	35	620
43	REVILLA	15	58	0	35	35	0	0	0	108
44	STHELENA	79	91	37	83	40	43	0	13	303
45	TASMAN	17	17	16	14	0	14	0	0	64
46	TRINDADE	17	30	0	22	22	0	0	0	69
47	TRISTAN	261	332	192	304	67	237	0	2	1091
48	VEMA	0	0	0	0	0	0	0	0	0
	Total	6554	8602	3039	7144	2393	4751	450	1131	26,920

Paul, Cape Verde, Madeira, Socorro-Revillagigedo, St. Helena, and Tristan-Gough-Walvis Ridge), but these ^{187}Os/^{188}Os analyses are filtered from figures and excluded from discussion due to low [Os] (< 50 ppt) (Supplementary Fig. 18c). No ^{187}Os/^{188}Os analyses are available for 22 out of 48 oceanic hotspots (i.e., Ascension, Baja-Guadalupe, Balleny, Bermuda, Bouvet, Bowie-Kodiak/Pratt-Welker, Caroline, Christmas Island, Cobb-Eickelberg/Axial-Juan de Fuca, Conrad, Discovery, Easter, Fernando de Noronha, Foundation, Manus Basin, Marion-Prince Edward, Meteor-Shona, New England, San Félix, Tasmantid-Tasman Central, Trindade-Martín Vaz, and Vema). As a result, 28 oceanic hotspots (i.e., 58 % of known oceanic hotspots) lack reliable ^{187}Os/^{188}Os data.

Sampling bias in the OIBID is further explored in Fig. 11 and Supplementary Fig. 19 which, instead of showing the range and median isotope values at each oceanic hotspot (Fig. 10), shows the number of isotope analyses made for different isotope systems at each oceanic hotspot. After filtering, there is a larger quantity of Nd, Pb and Sr isotopes data, while the Hf isotope system, and in particular the He and Os isotope systems, are not as well represented in the OIBID (see Fig. 11, Supplementary Fig. 19 and Table 3). ^{143}Nd/^{144}Nd ($N = 8601$ analyses in the OIBID), ^{206}Pb/^{204}Pb ($N = 7144$ after filtering out lower quality unspiked TIMS data), and ^{87}Sr/^{86}Sr ($N = 6553$ with MgO > 2 wt%) are the best sampled isotope systems in the OIBID (Fig. 11 and Supplementary Fig. 19). ^{176}Hf/ ^{177}Hf ($N = 3039$ for MC-ICP-MS analyses) is also a reasonably well sampled isotope system. However, ^{187}Os/^{188}Os ($N = 450$ for N-TIMS analyses with [Os] > 50 ppt) and ^{3}He/^{4}He ($N = 1131$ for analyses with [^{4}He] above the threshold values) have considerably fewer number of total analyses than the Sr-Nd-Pb-Hf isotope systems (the reasons for which are provided in Section 6 of the Supplementary Text).

A small handful of oceanic hotspots are overrepresented in terms of the total number of isotope analyses (Fig. 11 and Supplementary Fig. 19), which is consistent with previous observations (e.g., Weis et al., 2023). For example, Hawai'i is the best geochemically characterized oceanic hotspot: after filtering there are 1462 analyses for ^{87}Sr/^{86}Sr in Hawaiian OIB (Hawai'i represents 22 % of filtered ^{87}Sr/^{86}Sr data in OIBID), 1948 for ^{143}Nd/^{144}Nd (23 %), 943 for ^{176}Hf/ ^{177}Hf (31 %), 1753 for ^{206}Pb/^{204}Pb (24 %), 159 for ^{187}Os/^{188}Os (35 %), and 280 for ^{3}He/^{4}He (25 %) (see Table 3). Iceland is the second-best geochemically characterized oceanic hotspot: after filtering there are 889 analyses for

^{87}Sr/^{86}Sr in Icelandic OIB (Iceland represents 14 % of filtered ^{87}Sr/^{86}Sr data in OIBID), 1107 for ^{143}Nd/^{144}Nd (13 %), 435 for ^{176}Hf/ ^{177}Hf (14 %), 785 for ^{206}Pb/^{204}Pb (11 %), 39 for ^{187}Os/^{188}Os (9 %), and 113 for ^{3}He/^{4}He (10 %). When their datasets are considered together, Hawai'i and Iceland represent 35 to 45 % (depending on the isotope considered) of the total analyses for the Sr-Nd-Pb-Hf-Os-He isotope systems in the global OIB dataset of 48 oceanic hotspots.

Hawai'i and Iceland are so oversampled that the following nine best geochemically characterized oceanic hotspots (i.e., Azores, Canary, Cape Verde, Galápagos, Heard-Kerguelen, Macdonald, Réunion, Samoa, and Tristan-Gough-Walvis Ridge) must be grouped to achieve a similar proportion of the Sr-Nd-Pb-Hf-Os-He isotope analyses in the OIBID. Taken together, these nine oceanic hotspots represent 35 to 43 % of the total analyses for the Sr-Nd-Pb-Hf-Os-He isotope systems in the global OIB dataset. For these nine oceanic hotspots there are a total of 2839 analyses for ^{87}Sr/^{86}Sr (these nine oceanic hotspots represent 43 % of filtered ^{87}Sr/^{86}Sr data in OIBID), 3442 for ^{143}Nd/^{144}Nd (40 %), 1070 for ^{176}Hf/ ^{177}Hf (35 %), 3050 for ^{206}Pb/^{204}Pb (43 %), 186 for ^{187}Os/^{188}Os (41 %), and 449 for ^{3}He/^{4}He (40 %). When Hawai'i and Iceland are considered together with these 9 oceanic hotspots, we find that these 11 oceanic hotspots account for 75 to 85 % of total Sr-Nd-Pb-Hf-Os-He isotope analyses in the OIBID. In other words, $<$ 25 % of the oceanic hotspots (11 of 48 total oceanic hotspots) in the OIBID account for $\geq$75 % of the isotope data.

For the remaining 37 oceanic hotspots (i.e., 48 oceanic hotspots minus 11 oceanic hotspots considered above) there are only 1364 total analyses for ^{87}Sr/^{86}Sr (these 37 oceanic hotspots represent 21 % of filtered ^{87}Sr/^{86}Sr data in OIBID), 2105 for ^{143}Nd/^{144}Nd (24 %), 591 for ^{176}Hf/ ^{177}Hf (20 %), 1556 for ^{206}Pb/^{204}Pb (22 %), 66 for ^{187}Os/^{188}Os (15 %), and 289 for ^{3}He/^{4}He (25 %). When considered together, these 37 oceanic hotspots represent just 15 to 25 % of total Sr-Nd-Pb-Hf-Os-He isotope analyses in the OIBID. In other words, $>$ 75 % of the oceanic hotspots in the OIBID have $\leq$25 % of the isotope data, which illustrates the degree to which most oceanic hotspots remain poorly characterized.

The sampling and geochemical characterization of different hotspots is to some degree influenced by the accessibility at each hotspot. For example, Hawai'i and Iceland—the two best sampled and geochemically characterized oceanic hotspots—are both accessible islands with good infrastructure (e.g., accessible roads, ports, international airports) and relatively large human populations. It is more challenging to sample some of the other hotspots. For example, some of the hotspots consist entirely of submarine seamounts (e.g., Cobb-Eickelberg/Axial-Juan de Fuca, Discovery, Louisville, etc.), while lack of infrastructure and geographic inaccessibility can affect sampling at other hotspots (e.g., Balleny, Bouvet, etc.). Nonetheless, considerable efforts have been made to sample some of the more remote hotspots. For example, the Tristan-Gough-Walvis Ridge hotspot has a relatively small human population ($<$ 250 residents), yet it is the seventh best geochemically characterized hotspot in the OIBID.

3.3.2. *Isotope distributions in OIB compared to MORB*

Figs. 12–13 and Supplementary Fig. 20 show histograms for Sr-Nd-Pb-Hf-Os-He isotope analyses from the OIBID. The figures also show kernel density estimates of both the OIB isotope data (i.e., blue lines) and available MORB data (red lines) compiled in Gale et al. (2013). In these plots OIB are dominantly geochemically depleted in their radiogenic isotope compositions: the histograms show that majority of OIB have low ^{87}Sr/^{86}Sr (the peak in the distribution is at 0.7032), high ^{143}Nd/^{144}Nd (the peak is at 0.51294), and high ^{176}Hf/^{177}Hf (the peak is at 0.28310) (Fig. 12a and c and Supplementary Fig. 20a). While OIB are dominated by geochemically depleted compositions for ^{87}Sr/^{86}Sr, ^{143}Nd/^{144}Nd, and ^{176}Hf/^{177}Hf, OIB are not as geochemically depleted as MORB (e.g., Zindler and Hart, 1986; Paul et al., 2005; White, 2010; Harrison et al., 2020; Stracke et al., 2022). When the OIB distributions (for ^{87}Sr/^{86}Sr, ^{143}Nd/^{144}Nd, and ^{176}Hf/^{177}Hf data are compared to MORB distributions from Gale et al. (2013), the peaks of the MORB distributions have substantially lower ^{87}Sr/^{86}Sr (0.7026), higher ^{143}Nd/^{144}Nd (0.51306) and higher ^{176}Hf/^{177}Hf (0.28317) (Fig. 12a and c and Supplementary Fig. 20a), as is well established in the literature (e.g., Zindler and Hart, 1986; Hofmann, 1997; Stracke et al., 2022).

The OIB histogram for ^{3}He/^{4}He forms a peak at 8 R$_A$, similar to the MORB distribution (Fig. 12e). This observation is notable because it demonstrates that OIB exhibit a dominant ^{3}He/^{4}He composition that overlaps with the dominant 8 R$_A$ peak of the MORB distribution. This has potentially important implications for the origin and depth of the helium that defines that dominant 8 R$_A$ peak among global OIB, which we discuss in Section 3.3.4.2. Critically, while the peaks of the OIB and MORB ^{3}He/^{4}He distributions align at 8 R$_A$, the OIB distribution has tails that show significantly greater contributions from both lower and higher ^{3}He/^{4}He values than MORB (Fig. 12e), signaling greater ^{3}He/^{4}He heterogeneity in the OIB mantle (e.g., White, 2010; Moreira, 2013).

The radiogenic isotope ratios of Pb exhibit more complex histograms, with several peaks each (Fig. 13) (for example, see Weis et al., 2023). For example, the ^{207}Pb/^{204}Pb and ^{208}Pb/^{204}Pb histograms for OIB show two dominant peaks, one with unradiogenic (i.e., "low-Pb" peak) and one with moderately radiogenic ("mid-Pb" peak) Pb isotope ratios, and a third minor peak at radiogenic Pb compositions ("high-Pb" peak) that represents a smaller contribution of HIMU material (Fig. 13c and e). While the high-Pb peak is also present in the ^{206}Pb/^{204}Pb histogram, the low-Pb and mid-Pb peaks are not resolved as clearly. Instead, the low-Pb and mid-Pb peaks in the ^{206}Pb/^{204}Pb histogram are split up into several less-clearly-defined peaks (Fig. 13a).

Notably, Hawai'i and Iceland—which are the dominant contributors to the low-Pb peak—generally have lower ^{206}Pb/^{204}Pb (~18.4 ± 0.6, 2SD), ^{207}Pb/^{204}Pb (~15.47 ± 0.05, 2SD), and ^{208}Pb/^{204}Pb (~38.0 ± 0.5, 2SD) than other oceanic hotspots, and overlap with the MORB distribution (Fig. 13a, c and e). The mid-Pb peak includes lead isotope analyses from a variety of oceanic hotspots (and, hence, is not dominated by Pb isotope contributions from just two oceanic hotspots like the low-Pb peak) and has higher Pb-isotope ratios that only partially overlap with the MORB distribution. Finally, the small size of the high-Pb peak highlights the earlier observation that HIMU lavas make up only a minor portion of the OIBID (see Section 3.2).

3.3.3. *Geochemical bias in the OIB dataset resulting from oversampling Hawai'i and Iceland*

Oversampling of Hawai'i and Iceland—the two best geochemically characterized oceanic hotspots in the OIBID—significantly biases the isotope distributions for global OIB toward lower ^{206,207,208}Pb/^{204}Pb, and higher ^{3}He/^{4}He compositions. To illustrate the outsized impact that Hawai'i and Iceland have on the histograms of radiogenic isotope data in the OIB dataset, a separate set of histograms are shown that do not include data from the Hawai'i and Iceland hotspots (Supplementary Fig. 21). When Hawai'i and Iceland are removed, the low-Pb peak—which overlaps with the unimodal MORB distribution—*completely disappears* from the ^{206,207,208}Pb/^{204}Pb histograms (Supplementary Fig. 21d-f).

Similarly, when Hawai'i and Iceland are removed, the shape of the ^{3}He/^{4}He OIB histogram changes dramatically because Hawai'i and Iceland represent a large fraction of total ^{3}He/^{4}He analyses in the OIBID (35 %) and because Hawai'i and Iceland represent 67 % of high-^{3}He/^{4}He (i.e., $>$ 20 R$_A$) analyses in the OIBID dataset (Supplementary Fig. 21c). With the removal of Hawai'i and Iceland data, the peak of the ^{3}He/^{4}He OIB histogram still coincides with the peak of the MORB distribution (i.e., 8 ± 2 R$_A$) (Graham, 2002), but the broad OIB tail extending to high ^{3}He/^{4}He becomes much less pronounced (compare panel e in Fig. 12 to panel c in Supplementary Fig. 21). The strong influence that Hawai'i and Iceland have on the shape of the ^{3}He/^{4}He histogram illustrates the danger of interpreting individual peaks in the histograms of global OIB (Parman, 2007; Rudge, 2009) without first accounting for sampling bias.

The removal of Hawai'i and Iceland data only slightly changes the shape of the ^{87}Sr/^{86}Sr, ^{143}Nd/^{144}Nd, and ^{176}Hf/^{177}Hf histograms

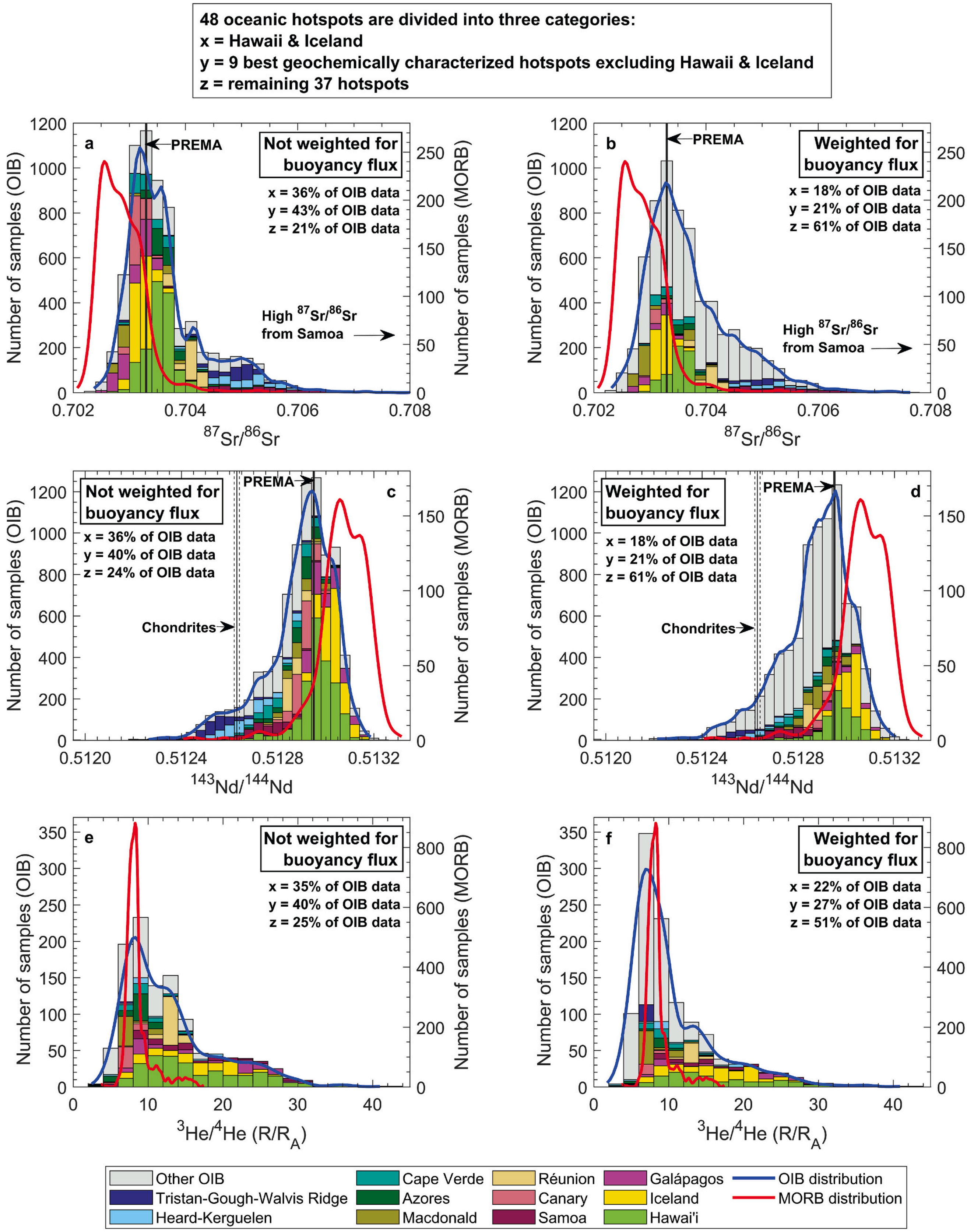

(caption on next page)

Fig. 12. Histograms for a) $^{87}Sr/^{86}Sr$ in all OIB, b) $^{87}Sr/^{86}Sr$ for all OIB where the data contributions for each oceanic hotspot are reweighted based on each hotspot's contribution to the global oceanic buoyancy flux, c) $^{143}Nd/^{144}Nd$ in all OIB, d) $^{143}Nd/^{144}Nd$ for all OIB where the data contributions for each oceanic hotspot are reweighted based on each hotspot's contribution to the global oceanic buoyancy flux, e) $^{3}He/^{4}He$ in all OIB, and f) $^{3}He/^{4}He$ for all OIB where the data contributions for each oceanic hotspot are reweighted based on each hotspot's contribution to the global oceanic buoyancy flux. The x-axis in panels a and b shows $^{87}Sr/^{86}Sr$ values up to 0.708, but thirteen $^{87}Sr/^{86}Sr$ analyses from Samoa have $^{87}Sr/^{86}Sr$ above 0.708 (up to 0.7205) and are therefore not shown in the $^{87}Sr/^{86}Sr$ histograms. Black vertical lines in panels a, b, c, and d, show estimated PREMA values for $^{87}Sr/^{86}Sr$ and $^{143}Nd/^{144}Nd$ (0.7033 and 0.51295, respectively, which are estimated from panels b and d by identifying the mode of the OIB distribution defined by the blue lines). The chondritic $^{143}Nd/^{144}Nd$ value, shown with black vertical lines in panels c and d, is from Bouvier et al. (2008) (0.512630 ± 0.000011). For OIB $^{87}Sr/^{86}Sr$ data with MgO < 2.0 wt% or no MgO, and $^{3}He/^{4}He$ data with [^{4}He] < 90 (gl), < 4 (ol), or < 2 (cpx) ncm^{3}STP/g are not shown in the figure. $^{87}Sr/^{86}Sr$ and $^{143}Nd/^{144}Nd$ data used to plot the MORB distributions are from Gale et al. (2013), and MORB $^{3}He/^{4}He$ data are compiled in Graham (2002) and updated to include data from Gautheron et al. (2015), Graham et al. (2014, 2018), Graham and Michael (2021), and Moreira et al. (2008). The MORB data were not filtered (e.g., sampling depth, helium concentration etc.). OIB and MORB distributions are constructed using a kernel smoothing function fit. The three data categories (i.e., x, y, and z) sum to 100 %, and are provided to illustrate sampling bias in the OIB dataset (left versus right panels). Equivalent plots showing $^{176}Hf/^{177}Hf$ and $^{187}Os/^{188}Os$ are presented in Supplementary Fig. 20. (For interpretation of the references to color in this figure legend, the reader is referred to the web version of this article.)

(Supplementary Fig. 21a-b and g). The peaks for $^{143}Nd/^{144}Nd$ and $^{176}Hf/^{177}Hf$ shift—$^{143}Nd/^{144}Nd$ from 0.51294 to 0.51290 and $^{176}Hf/^{177}Hf$ from 0.28310 to 0.28303—and the width of the peaks narrow substantially (because of the removal of high $^{143}Nd/^{144}Nd$ and high $^{176}Hf/^{177}Hf$ ratios that characterize the Hawai'i and Iceland datasets). Finally, the $^{87}Sr/^{86}Sr$ peak (at 0.7032) does not shift appreciably when Hawai'i and Iceland data are removed.

3.3.4. *Reweighting OIB isotope datasets using hotspot buoyancy flux to correct for geochemical sampling bias across the 48 oceanic hotspots*

The considerable sampling bias observed in the OIBID prevents clear understanding of the actual composition of the OIB mantle source and the distribution of different end-members in the mantle. The OIB dataset can be reweighted to overcome this sampling bias. Many approaches can be used to reweight the OIB dataset. For example, each of the 48 oceanic hotspots included in the OIBID could be weighted equally. However, it is highly unlikely that the 48 oceanic hotspots each sample an equal volume of the OIB mantle source. Another possible reweighting approach is to reweight the hotspots based on magma volume. However, magma volume estimates are available for only a small subset of oceanic hotspots, which makes reweighting for magma volume an impractical option for the global suite of oceanic hotspots. Instead, we use an approach that is similar to the approach by Arevalo Jr. et al. (2009): we reweight the OIB dataset based on the hotspot buoyancy flux of each hotspot. Hotspot buoyancy flux can be used for reweighting because hotspot buoyancy flux estimates are available for the global suite of oceanic hotspots (e.g., Davies, 1988, 1992; Sleep, 1990; Schilling, 1991; Ito et al., 1997; Ribe and Christensen, 1999; King and Adam, 2014; Parnell-Turner et al., 2014; Hoggard et al., 2020).

Buoyancy flux is related to the upward flow of material from deeper in the mantle. We suggest here that the geochemical sampling at an oceanic hotspot should ideally be in proportion to the buoyancy flux. This way the number of geochemical analyses made at an oceanic hotspot would be in direct proportion to the mass of material upwelling in the plume: high flux hotspots should have a larger number of isotope analyses, and low plume flux hotspots should have a proportionally smaller number of isotope analyses. Therefore, in order to correct for the current sampling bias in the OIB dataset, we reweight the contribution from the isotope analyses at each hotspot using that hotspot's fractional contribution to the global oceanic hotspot buoyancy flux (see Supplementary Text for details regarding the reweighting method).

3.3.4.1. Reweighting OIB histograms for hotspot buoyancy flux: Implications for the Pb composition of the OIB mantle source. When OIB Pb isotope histograms are reweighted based on buoyancy flux, the low-Pb peak shrinks dramatically because the contribution from Hawai'i and Iceland decreases dramatically (Fig. 13b, d and f). Additionally, the mid-Pb peak expands, which is primarily because the 37 oceanic hotspots categorized as "other OIB" are dominated by Pb isotope compositions that fall in the range of the mid-Pb peak (Fig. 13d-f). The expansion of the mid-Pb peak in the buoyancy flux-weighted histograms shows that majority of oceanic hotspots sample a mantle source that has significantly more radiogenic Pb-isotope signatures than both the unweighted OIB dataset and the global MORB dataset. This means that the Pb isotope composition of OIB have higher $^{207}Pb/^{204}Pb$ and $^{206}Pb/^{204}Pb$ (Fig. 13)—and are thus even further to the right of the terrestrial geochron—than suggested by unweighted datasets, which has important implications for identifying the terrestrial domain to the left of the geochron that is needed to solve the first Pb paradox: the Pb isotope composition of bulk Earth must lie on the geochron, so there must be a reservoir with unradiogenic Pb located to the left of the geochron that balances the radiogenic Pb in the OIB reservoir. Because the reweighted histograms show that OIB have more radiogenic Pb, the reservoir located to the left of the geochron must be larger, and/or have higher Pb concentrations, and/or have even more unradiogenic Pb than the unweighted OIB Pb-isotope data indicate (e.g., Oversby and Ringwood, 1971; Vollmer, 1977; Allègre et al., 1982; Zartman and Haines, 1988; Hart and Gaetani, 2006; Malaviarachchi et al., 2008; Burton et al., 2012; Castillo, 2016; Zhang et al., 2020; Doucet et al., 2023 and references therein).

3.3.4.2. Reweighting OIB histograms for hotspot buoyancy flux: OIB are dominated by MORB-like $^{3}He/^{4}He$. While reweighting isotope histograms for global hotspot buoyancy flux has a clear impact on their shape, the $^{3}He/^{4}He$ peak in the buoyancy flux-weighted histogram still plots in the MORB range (8 ± 2 R_A, or 6 to 10 R_A) (Graham, 2002): the unweighted OIB peak is in the 8–10 R_A range, which is slightly higher than the 6–8 R_A range of the reweighted OIB peak (Fig. 12e-f). However, the salient observation is that the OIB $^{3}He/^{4}He$ peak, while still positioned in the MORB range, both narrows and increases in prominence in the reweighted histogram (Fig. 12f). In other words, the fraction of OIB $^{3}He/^{4}He$ data that lie within the MORB range expands in the reweighted $^{3}He/^{4}He$ histogram: slightly more than half of the total OIB $^{3}He/^{4}He$ analyses (51 %) plot within the MORB range in the reweighted histogram compared to just 38 % in the unweighted $^{3}He/^{4}He$ histogram (Fig. 12e-f). The observations that 1) the peak of the OIB $^{3}He/^{4}He$ distribution corresponds with the peak of the MORB $^{3}He/^{4}He$ histogram, and 2) more than half of OIB $^{3}He/^{4}He$ lies within the MORB range could be interpreted to mean that the lower mantle source of plumes is host to a more degassed MORB-like $^{3}He/^{4}He$ component, which would mean that the MORB $^{3}He/^{4}He$ reservoir is not limited to the upper mantle. Using an approach from Jackson et al. (2021) that categorizes hotspots into two categories—hotspots sourced by plumes versus non-plume hotspots—by pairing seismic and geodynamics constraints to trace plume conduits into the mantle, we show that the $^{3}He/^{4}He$ histogram for plume-sourced hotspots has a peak in the MORB range (Supplementary Fig. 23). This strengthens the hypothesis that the lower mantle source of plumes hosts MORB-like $^{3}He/^{4}He$.

But how is it that deeply-sourced plumes have a dominant $^{3}He/^{4}He$ peak that overlaps with MORB? Deep mantle plumes do not efficiently entrain upper mantle material (Hart et al., 1992; Farnetani et al., 2002)—making entrainment of upper mantle $^{3}He/^{4}He$ an unlikely mechanism explaining the dominance of MORB-like $^{3}He/^{4}He$

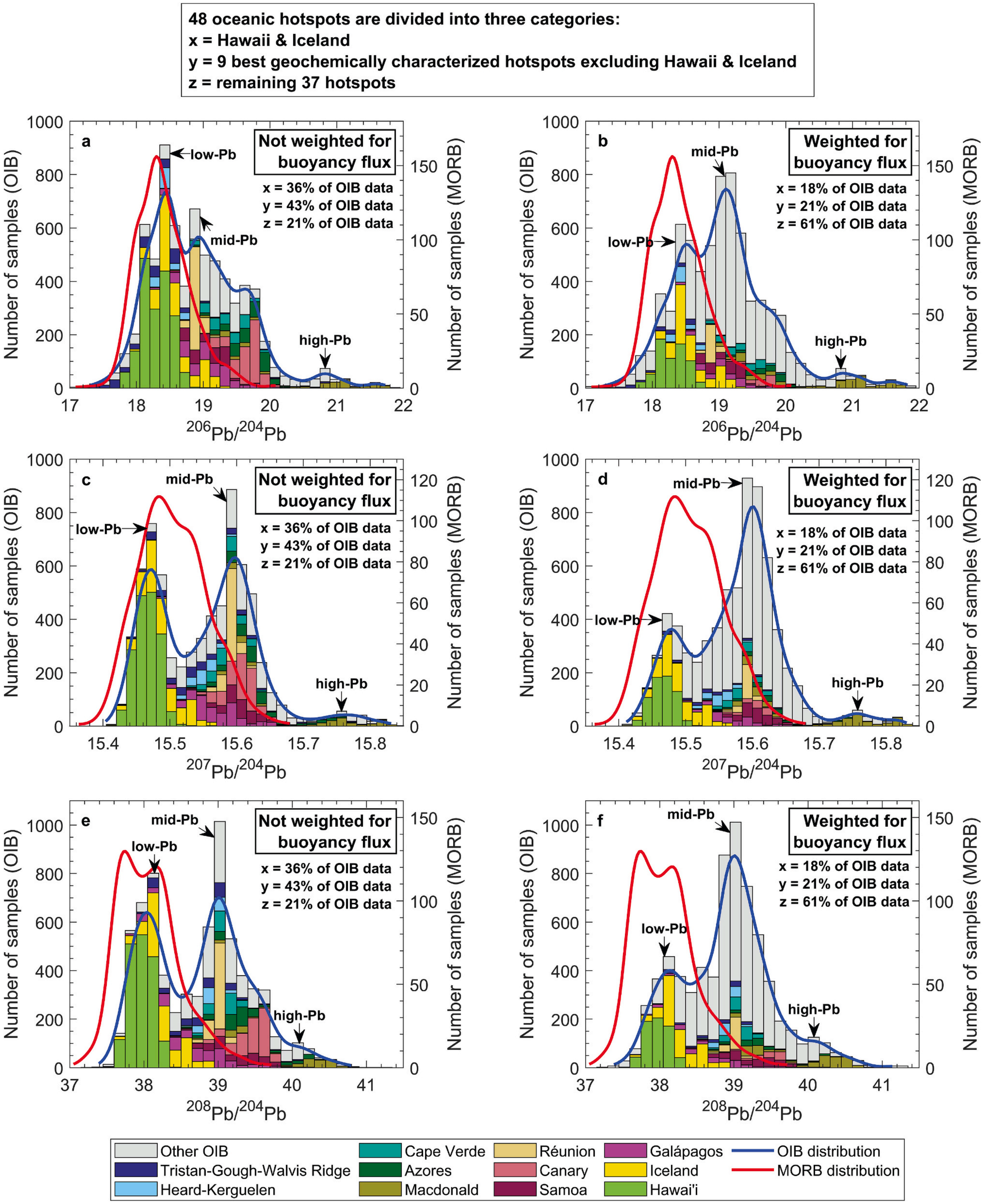

Fig. 13. Histograms for a) ^{206}Pb/^{204}Pb in all OIB, b) ^{206}Pb/^{204}Pb for all OIB where the data contributions for each oceanic hotspot are reweighted based on each hotspot's contribution to the global oceanic buoyancy flux, c) ^{207}Pb/^{204}Pb in all OIB, d) ^{207}Pb/^{204}Pb for all OIB where the data contributions for oceanic each hotspot are reweighted based on each hotspot's contribution to the global oceanic buoyancy flux, e) ^{208}Pb/^{204}Pb in all OIB, and f) ^{208}Pb/^{204}Pb for all OIB where the data contributions for each oceanic hotspot are reweighted based on each hotspot's contribution to the global oceanic buoyancy flux. For OIB, higher quality unspiked TIMS Pb isotope data are included in the figure, but the lower quality unspiked TIMS Pb isotope data are not (see Supplementary Text Section 4.3.2.1.). Pb isotope data from Gale et al. (2013) are used to plot the MORB distributions. OIB and MORB distributions are constructed using a kernel smoothing function fit. The three data categories (i.e., x, y, and z) sum to 100 %, and are provided to illustrate sampling bias in the OIB dataset (left and right panels).

compositions in OIB—suggesting that the lower mantle sampled by plumes hosts a large domain dominated by a more degassed MORB-like $^3He/^4He$. The upper and lower mantle are not isolated from each other (e.g., Grand et al., 1997; Bijwaard et al., 1998; Helffrich and Wood, 2001), so it is perhaps not unexpected that both the upper mantle and large domains of the lower mantle have similar MORB-like $^3He/^4He$ reservoirs. In contrast, domains with the highest $^3He/^4He$ are not sampled by MORB because they are deep and isolated, possibly due to greater density, so they are entrained only by the hottest and most buoyant plumes (Jackson et al., 2017; Bao et al., 2022).

An additional impact of reweighting the $^3He/^4He$ dataset for buoyancy flux is that the contribution from higher $^3He/^4He$ compositions diminishes in the reweighted histogram (Fig. 12e-f). Only ~9 % of OIB have high $^3He/^4He$ (> 20 R_A) in the reweighted histograms, while 15 % of OIB have high $^3He/^4He$ in the unweighted histograms. This decrease indicates that high $^3He/^4He$ compositions in the OIBID are oversampled, and that the high $^3He/^4He$ reservoir is even less common than suggested by unweighted datasets. Similarly, in Supplementary Fig. 23, only 17 % of $^3He/^4He$ analyses from plume-sourced hotspots have high $^3He/^4He$, diminishing to 11 % if in the reweighted histogram. Because all hotspots with high $^3He/^4He$ (> 20 R_A) are linked to deep plumes (Supplementary Fig. 23), and because high $^3He/^4He$ is relatively rare component even among plume-sourced hotspots, we infer that the fraction of the lower mantle that is host to high $^3He/^4He$ is relatively small. In short, reweighting for hotspot buoyancy flux shows that the high $^3He/^4He$ domain is less common and that a more degassed MORB-like component sampled by plumes is more common.

The oversampling of high $^3He/^4He$ is further demonstrated in Fig. 14 where $^3He/^4He$ amplitude, and the maximum $^3He/^4He$ measured at each oceanic hotspot, are plotted against the number of $^3He/^4He$ analyses at each hotspot. Isotope amplitude is calculated following the approach of Zindler and Hart (1986), where the range of a specific isotope system at a given hotspot is expressed as a percentage of the total isotope variability for that isotope system in all OIB. $^3He/^4He$ forms a correlation when isotope amplitude is plotted with number of analyses. However, unlike $^3He/^4He$, the other isotope systems (i.e., $^{87}Sr/^{86}Sr$, $^{143}Nd/^{144}Nd$, $^{176}Hf/^{177}Hf$, $^{206}Pb/^{204}Pb$, $^{207}Pb/^{204}Pb$, $^{208}Pb/^{204}Pb$, and $^{187}Os/^{188}Os$) exhibit no clear relationship between amplitude and the number of analyses (Fig. 14 and Supplementary Fig. 24).

It is not clear why $^3He/^4He$ is the only isotope system to exhibit a

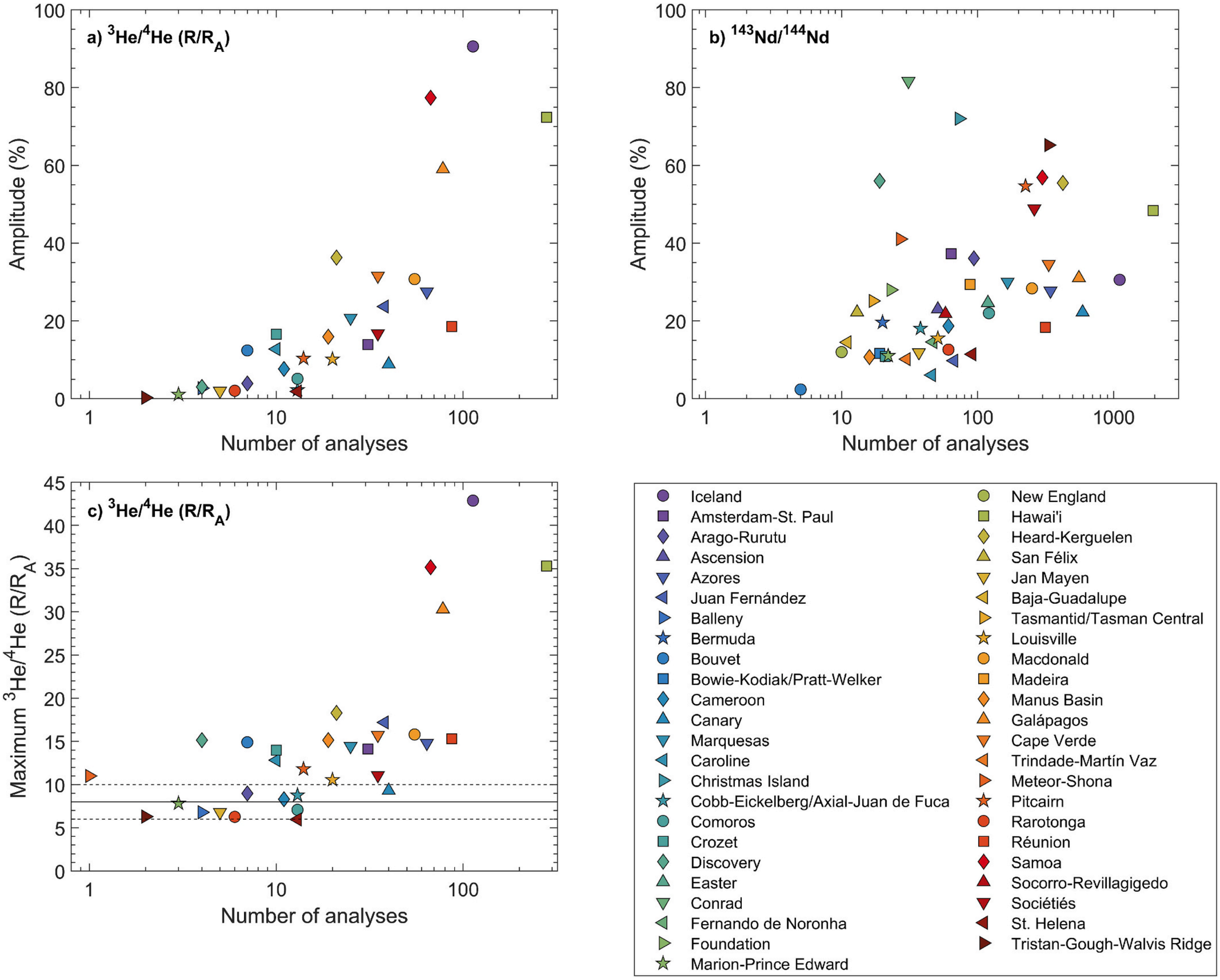

Fig. 14. Isotope amplitude and maximum $^3He/^4He$ plotted against number of analyses, where amplitude is the range of a specific isotope system at a given oceanic hotspot expressed as a percentage of the total isotope variability for that isotope system in all OIB. a) $^3He/^4He$ amplitude plotted against number of analyses, b) $^{143}Nd/^{144}Nd$ amplitude plotted against number of analyses, and c) maximum $^3He/^4He$ plotted against number of analyses. Average MORB composition and 2σ from Graham (2002) is shown with black horizontal lines in panel c. Equivalent plots showing $^{87}Sr/^{86}Sr$, $^{176}Hf/^{177}Hf$, $^{206}Pb/^{204}Pb$, $^{207}Pb/^{204}Pb$, $^{208}Pb/^{204}Pb$ and $^{187}Os/^{188}Os$ amplitude are presented in Supplementary Fig. 24.

relationship between amplitude and the number of analyses, or why there is a relationship between the maximum $^3He/^4He$ and the number of helium isotope analyses at an oceanic hotspot. However, the correlation between $^3He/^4He$ amplitude and number of $^3He/^4He$ analyses (Fig. 14) does *not* imply that, if enough samples at a specific hotspot are analyzed, a high $^3He/^4He$ lava will be discovered. Instead, we speculate that the geochemical community's particular interest in high $^3He/^4He$ values may provide a clue. Significant effort has been made to sample and characterize lavas from high $^3He/^4He$ hotspots in order to place further constraints on the high $^3He/^4He$ domain in the mantle (e.g., Valbracht et al., 1997; Hilton et al., 1999; Class and Goldstein, 2005; Kurz et al., 2009; Starkey et al., 2009; Jackson et al., 2020; Mundl-Petermeier et al., 2020; Horton et al., 2023), and this may help explain the correlations between $^3He/^4He$ amplitude, maximum $^3He/^4He$, and the number of $^3He/^4He$ analyses. We hypothesize that these correlations are a result of sampling bias: when high $^3He/^4He$ is discovered, that locality becomes the focus of an intense sampling effort and geochemists return to the same locality for further sampling and analyses (explaining the larger number of helium isotope analyses at high $^3He/^4He$ localities), at the expense of oceanic hotspot localities with lower $^3He/^4He$ that do not garner the same attention (because they are less "interesting" to the geochemical community and are less well characterized). This skewed sampling effort results in a strong sampling bias toward high $^3He/^4He$ hotspot localities.

While reweighting of the OIB dataset for oceanic hotspot buoyancy flux corrects only for inter-hotspot sampling bias, and not human sampling bias, this reweighting scheme should be robust for the Sr-Nd-Pb-Hf-Os isotope systems. This is because, unlike $^3He/^4He$, the Sr-Nd-Pb-Hf-Os systems exhibit poor correlations between isotope amplitude and the number of isotope analyses (Fig. 14 and Supplementary Fig. 24). These poor correlations suggest that, for example, extreme EM and extreme HIMU localities were not oversampled relative to non-EM and non-HIMU localities.

3.3.4.3. Reweighting OIB histograms for hotspot buoyancy flux: estimating the PREMA composition. The reweighted $^{87}Sr/^{86}Sr$, $^{143}Nd/^{144}Nd$, and $^{176}Hf/^{177}Hf$ histograms (Fig. 12b and d and Supplementary Fig. 20b) are used to define the composition of PREMA. Zindler and Hart (1986) identified PREMA as the "high frequency" component (i.e., the mode of the dataset) in histograms showing $^{87}Sr/^{86}Sr$ and $^{143}Nd/^{144}Nd$, and we follow this approach for defining PREMA for Sr-Nd-Hf isotopes using the reweighted OIB distributions (see Section 3.3.4. and Supplementary Text for description of the reweighting method and Supplementary Table 3 and Supplementary Fig. 22 for reweighting factors).

In the reweighted histograms (Fig. 12b and d and Supplementary Fig. 20b), the $^{143}Nd/^{144}Nd$ mode is slightly higher (0.51295) than in the unweighted histogram (0.51294), the $^{87}Sr/^{86}Sr$ mode shifts slightly from 0.7032 (unweighted) to 0.7033 (reweighted), and the $^{176}Hf/^{177}Hf$ mode in the reweighted histogram shifts by nearly 2.5 epsilon units relative to the unweighted histograms (from 0.28310 to the reweighted ratio of 0.28303). Zindler and Hart's (1986) estimates for $^{87}Sr/^{86}Sr$ and $^{143}Nd/^{144}Nd$ of PREMA (0.7033 and 0.5130, respectively) are identical to our PREMA estimate for $^{87}Sr/^{86}Sr$ (0.7033) and similar to our $^{143}Nd/^{144}Nd$ PREMA estimate (0.51295), and our $^{87}Sr/^{86}Sr$ and $^{143}Nd/^{144}Nd$ estimates are within the PREMA range defined by Cai et al. (2023). Finally, our PREMA $^{176}Hf/^{177}Hf$ estimate (0.28303) is to our knowledge, the first based on isotope distributions. It is within the PREMA range defined by Cai et al. (2023) (0.28290–0.28305) and it is similar to the Giuliani et al.'s (2021) PREMA estimate (0.283100) that employed the Nd—Hf isotope mantle array to calculate the $^{176}Hf/^{177}Hf$ composition of PREMA using an assumed $^{143}Nd/^{144}Nd$ value.

Similar to older PREMA estimates (Zindler and Hart, 1986), our PREMA estimates imply that OIB mainly sample a dominantly geochemically depleted mantle source (e.g., Stracke et al., 2019, 2022). In fact, the reweighted $^{143}Nd/^{144}Nd$ histogram demonstrates that 93 % of all OIB lavas with Nd isotopes analyzed are geochemically depleted (i.e., $^{143}Nd/^{144}Nd > 0.51263$). The observation that geochemically enriched end-members (i.e., $^{143}Nd/^{144}Nd < 0.51263$) are rare in the mantle sampled by OIB, and that the mantle is instead dominated by geochemically depleted end-members—some of which are ultra-depleted (Stracke et al., 2019, 2022)—is not new (e.g., Zindler and Hart, 1986; Giuliani et al., 2021). Nonetheless, the geochemical community has not reached a consensus regarding the origin of the wide-scale geochemical depletion in the OIB mantle sampled by oceanic hotspots (Hofmann et al., 2022). Is it the result of early differentiation of the mantle by continental extraction and, if so, how early (e.g., Giuliani et al., 2021)? Is there a heretofore-unsampled enriched reservoir—-which resulted from early depletion of the planet and complements the geochemical depletion observed in the mantle—residing in the deep mantle, awaiting to be discovered with new geochemical techniques (e.g., Boyet and Carlson, 2005; Šrámek et al., 2013)? Or were the geochemically enriched products of early depletion lost to space, leaving the planet geochemically depleted (e.g., O'Neill and Palme, 2008; Frossard et al., 2022)? The fact that such fundamental questions remain to be answered are a clear indication that geochemical inquiry into the composition of Earth's mantle remains globally-relevant and far from complete.

4. Summary

We compile and present a global OIB database that includes Sr-Nd-Pb-Hf-Os-He-$\delta^{18}O$ isotope data as well as supporting major and trace element concentrations from 48 oceanic hotspots. We find that the existing isotope dataset for global OIB is highly biased and over-represents a small number of hotspots, and many hotspots are still missing key isotope data (e.g., some hotspots still lack $^{176}Hf/^{177}Hf$, $^{187}Os/^{188}Os$, and/or $^3He/^4He$). As a result of this bias in sampling and geochemical characterization, <25 % of oceanic hotspots account for ≥75 % of the available isotope data in the global database, where Hawai'i and Iceland alone account for 35 % to 45 % of available isotope analyses. Therefore, histograms of the OIB isotope data are not representative of the OIB mantle source. To minimize bias and obtain isotope distributions that are representative of the OIB mantle source, isotope distributions are reweighted based on hotspot buoyancy flux. Reweighted isotope distributions show that the mantle source sampled by OIB is dominantly geochemically depleted, has more radiogenic Pb than the unweighted OIB datasets suggests, and is dominated by MORB-like $^3He/^4He$ signatures. In other words, high $^3He/^4He$ is relatively rare in the mantle source of OIB, even more rare than suggested by unweighted histograms of OIB $^3He/^4He$ data.

Looking ahead, there are several ways to improve on the current bias in the OIB database. For example, the majority of OIB samples in the compiled database lack complete isotope data (i.e., Sr-Nd-Pb-Hf-Os-He), and a more concerted effort should be made to obtain multiple isotopes (Sr-Nd-Pb-Hf-Os-He) and major and trace element data on the same sample, including legacy OIB samples with incomplete geochemical analyses. However, in some cases obtaining complete isotope data (i.e., Sr-Nd-Pb-Hf-Os-He) is challenging because the required isotope analyses cannot be carried out on the same sample. For example, in order to measure $^3He/^4He$ the sample needs to contain submarine glass, olivine and/or clinopyroxene phenocrysts. If a sample lacks these phases $^3He/^4He$ cannot be measured in the sample. Similarly, evolved/differentiated samples tend to have low Os concentrations, making it difficult to reliably obtain isotope signatures that reflect derivation from the mantle source. Additionally, sampling campaigns targeting poorly characterized hotspots are particularly welcome, especially those targeting low hotspot buoyancy flux hotspots that tend to be underrepresented in the global OIB geochemical database as well as the hotspots that still lack key isotopes data (e.g., Hf, Os, and/or He isotopes). This effort will require sample sharing between labs, and support from funding agencies to target the class of poorly characterized low-flux hotspots that do not garner the same attention as the high-flux Hawai'i and Iceland hotspots. Studying low buoyancy flux hotspots in greater detail will allow the community to evaluate whether there are systematic geochemical variations that relate to a hotspot's buoyancy, thereby providing a potential future research direction that links the geochemistry and geodynamics of hotspots.

It is important to the community that several key localities like Hawai'i and Iceland are very carefully geochemically characterized, because these hotspots provide greater geochemical context necessary for making fundamental new advances in mantle geochemistry. Therefore, we do not suggest a diminished focus on hotspots like Hawai'i and Iceland. However, we do hope that the less well geochemically characterized hotspots can receive more attention moving forward.

CRediT authorship contribution statement

Sunna Harðardóttir: Writing – review & editing, Writing – original draft, Investigation, Formal analysis, Data curation, Conceptualization. **Matthew G. Jackson:** Writing – review & editing, Writing – original draft, Supervision, Funding acquisition, Conceptualization.

Declaration of competing interest

The authors declare that they have no known competing financial interests or personal relationships that could have appeared to influence the work reported in this paper.

Acknowledgements

David Graham is thanked for sharing his MORB $^3He/^4He$ database and other publications that were used to generate the $^3He/^4He$ MORB distribution in Fig. 12 and Supplementary Fig. 23. Sæmundur Ari Halldórsson, Francis Macdonald, Simon Matthews and Roberta Rudnick are thanked for discussion that helped improve the manuscript. Michael Bizimis, Val Finlayson, Edward Marshall and Eemu Ranta are thanked for providing comments on the manuscript. Maja Bar Rasmussen is thanked for help with oxygen isotope calculations. Additionally, many members of the geochemical community kindly responded to our queries regarding their published geochemical data, and we are indebted to these individuals. Don Porcelli is thanked for editorial handling and Dominique Weis and an anonymous reviewer are thanked for constructive comments that helped improve the manuscript. MGJ acknowledges NSF grants OCE-1929095, OCE-1912931, and EAR-1900652 that funded this research.

Appendix A. Supplementary data

Supplementary data to this article can be found online at https://doi.org/10.1016/j.chemgeo.2024.122505.

Data availability

Data is shared as a supplementary Excel spreadsheet

References

Abedini, A.A., van Soest, M., Hurwitz, S., Kennedy, B.M., 2006. Helium isotopes in basalt-hosted olivines from the Yellowstone Plateau: implications on volcanic processes. In: AGU Fall Meeting Abstract V51D-1700.

Akbari, M., Ghorbani, M.R., Cousens, B.L., Graham, I.T., 2023. A robust discrimination scheme for ocean island basalts based on Ce/Rb, Tb/La, and Ba/Nb ratios. Chem. Geol. 628, 121486. https://doi.org/10.1016/j.chemgeo.2023.121486.

Allègre, C.J., Dupre, B., Brevart, O., 1982. Chemical aspects of the formation of the core. Philosophical transactions of the Royal Society of London. Series A, Mathemat. Phys. Sci. 306, 49–59. https://doi.org/10.1098/rsta.1982.0065.

Arevalo Jr., R., McDonough, W.F., Luong, M., 2009. The K/U ratio of the silicate Earth: insights into mantle composition, structure and thermal evolution. Earth Planet. Sci. Lett. 278, 361–369. https://doi.org/10.1016/j.epsl.2008.12.023.

Ashwal, L., Torsvik, T., Horvath, P., Harris, C., Webb, S., Werner, S., Corfu, F., 2016. A mantle-derived origin for Mauritian trachytes. J. Petrol. 57, 1645–1675. https://doi.org/10.1093/petrology/egw052.

Bai, R., Jackson, M.G., Huang, F., Moynier, F., Devos, G., Halldórsson, S.A., Lisiecki, L., Yin, H., Peng, Y., Nan, X., 2022. Barium isotopes in ocean island basalts are tracers of mantle processes. Geochim. Cosmochim. Acta 336, 436–447. https://doi.org/10.1016/j.gca.2022.08.023.

Bao, X., Lithgow-Bertelloni, C.R., Jackson, M.G., Romanowicz, B., 2022. On the relative temperatures of Earth's volcanic hotspots and mid-ocean ridges. Science 375, 57–61. https://doi.org/10.1126/science.abj8944.

Barling, J., Goldstein, S.L., Nicholls, I.A., 1994. Geochemistry of Heard Island (Southern Indian Ocean): characterization of an enriched mantle component and implications for enrichment of the sub-Indian ocean mantle. J. Petrol. 35, 1017–1053. https://doi.org/10.1093/petrology/35.4.1017.

Bijwaard, H., Spakman, W., Engdahl, E.R., 1998. Closing the gap between regional and global travel time tomography. J. Geophys. Res. 103, 30055–30078. https://doi.org/10.1029/98JB02467.

Bindeman, I.N., Davis, A.M., Drake, M.J., 1998. Ion microprobe study of plagioclase-basalt partition experiments at natural concentration levels of trace elements. Geochim. Cosmochim. Acta 62, 1175–1193. https://doi.org/10.1016/S0016-7037(98)00047-7.

Blichert-Toft, J., Frey, F.A., Albarede, F., 1999. Hf isotope evidence for pelagic sediments in the source of Hawaiian basalts. Science 285, 879–882. https://doi.org/10.1126/science.285.5429.879.

Bouvier, A., Vervoort, J.D., Patchett, P.J., 2008. The Lu-Hf and Sm-Nd isotopic composition of CHUR: constraints from unequilibrated chondrites and implications for the bulk composition of terrestrial planets. Earth Planet. Sci. Lett. 273, 48–57. https://doi.org/10.1016/j.epsl.2008.06.010.

Boyet, M., Carlson, R.W., 2005. ^{142}Nd evidence for early (>4.53 Ga) global differentiation of the silicate Earth. Science 309, 576–581. https://doi.org/10.1126/science.1113634.

Boyet, M., Doucelance, R., Israel, C., Bonnand, P., Auclair, D., Suchorski, K., Bosq, C., 2019. New constraints on origin of the EM-1 component revealed by the measurement of the La-Ce isotope systematics in Gough Island lavas. Geochem. Geophys. Geosyst. 20, 2484–2498. https://doi.org/10.1029/2019GC008228.

Burton, K.W., Cenki-Tok, B., Mokadem, F., Harvey, J., Gannoun, A., Alard, O., Parkinson, I.J., 2012. Unradiogenic lead in Earth's upper mantle. Nat. Geosci. 5, 570–573. https://doi.org/10.1038/ngeo1531.

Cai, R., Liu, J., Pearson, D.G., Giuliani, A., van Keken, P.E., Oesch, S., 2023. Widespread PREMA in the upper mantle indicated by low-degree basaltic melts. Nat. Commun. 14, 8150. https://doi.org/10.1038/s41467-023-43845-4.

Castillo, P.R., 2015. The recycling of marine carbonates and sources of HIMU and FOZO Ocean island basalts. Lithos 216–217, 254–263. https://doi.org/10.1016/j.lithos.2014.12.005.

Castillo, P.R., 2016. A proposed new approach and unified solution to old Pb paradoxes. Lithos 252–253, 32–40. https://doi.org/10.1016/j.lithos.2016.02.015.

Castillo, P.R., MacIsaac, C., Perry, S., Veizer, J., 2018. Marine carbonate in the mantle source of oceanic basalts: Pb isotopic constraints. Sci. Rep. 8, 14932. https://doi.org/10.1038/s41598-018-33178-4.

Chauvel, C., Hofmann, A.W., Vidal, P., 1992. HIMU-EM: the French Polynesian connection. Earth Planet. Sci. Lett. 110, 99–119 doi:0.1016/0012-821X(92)90042-T.

Chauvel, C., McDonough, W., Guille, G., Maury, R., Duncan, R., 1997. Contrasting old and young volcanism in Rurutu Island, Austral chain. Chem. Geol. 139, 125–143. https://doi.org/10.1016/S0009-2541(97)00029-6.

Chauvel, C., Maury, R.C., Blais, S., Lewin, E., Guillou, H., Guille, G., Rossi, P., Gutscher, M.-A., 2012. The size of plume heterogeneities constrained by Marquesas isotopic stripes. Geochem. Geophys. Geosyst. 13. https://doi.org/10.1029/2012GC004123. Q07005.

Class, C., Goldstein, S.L., 2005. Evolution of helium isotopes in the Earth's mantle. Nature 436, 1107–1112. https://doi.org/10.1038/nature03930.

Class, C., Goldstein, S.L., Shirey, S.B., 2009. Osmium isotopes in Grande Comore lavas: a new extreme among a spectrum of EM-type mantle endmembers. Earth Planet. Sci. Lett. 284, 219–227. https://doi.org/10.1016/j.epsl.2009.04.031.

Collerson, K.D., Williams, Q., Ewart, A.E., Murphy, D.T., 2010. Origin of HIMU and EM-1 domains sampled by ocean island basalts, kimberlites and carbonatites: the role of CO_2-fluxed lower mantle melting in thermochemical upwellings. Phys. Earth Planet. Inter. 181, 112–131. https://doi.org/10.1016/j.pepi.2010.05.008.

Condie, K.C., 2003. Incompatible element ratios in oceanic basalts and komatiites: tracking deep mantle sources and continental growth rates with time. Geochem. Geophys. Geosyst. 4, 1005. https://doi.org/10.1029/2002GC000333.

Condie, K., 2015. Changing tectonic settings through time: indiscriminate use of geochemical discriminant diagrams. Precambrian Res. 266, 587–591. https://doi.org/10.1016/j.precamres.2015.05.004.

Condie, K.C., 2021. Two major transitions in Earth history: evidence for two lithospheric strength thresholds. J. Geol. 129, 455–473. https://doi.org/10.1086/711141.

Cordier, C., Chauvel, C., Hemond, C., 2016. High-precision lead isotopes and stripy plumes: revisiting the Society chain in French Polynesia. Geochim. Cosmochim. Acta 189, 236–250. https://doi.org/10.1016/j.gca.2016.06.010.

Cordier, C., Delavault, H., Chauvel, C., 2021. Geochemistry of the Society and Pitcairn-Gambier mantle plumes: what they share and do not share. Geochim. Cosmochim. Acta 306, 362–384. https://doi.org/10.1016/j.gca.2021.04.014.

Davies, G.F., 1988. Ocean bathymetry and mantle convection: 1. Large-scale flow and hotspots. J. Geophys. Res. 93, 10467–10480. https://doi.org/10.1029/JB093iB09p10467.

Davies, G.F., 1992. Temporal variation of the Hawaiian plume flux. Earth Planet. Sci. Lett. 113, 277–286. https://doi.org/10.1016/0012-821X(92)90225-K.

Debaille, V., Trønnes, R.G., Brandon, A.D., Waight, T.E., Graham, D.W., Lee, C.A., 2009. Primitive off-rift basalts from Iceland and Jan Mayen: Os-isotopic evidence for a mantle source containing enriched subcontinental lithosphere. Geochim. Cosmochim. Acta 73, 3423–3449. https://doi.org/10.1016/j.gca.2009.03.002.

Delavault, H., Chauvel, C., Thomassot, E., Devey, C.W., Dazas, B., 2016. Sulfur and lead isotopic evidence of relic Archean sediments in the Pitcairn mantle plume. Proc. Natl. Acad. Sci. USA 113, 12952–12956. https://doi.org/10.1073/pnas.1523805113.

Doucet, L.S., Li, Z.-X., Fougerouse, D., Olierook, H.K.H., Gamaleldien, H., Kirkland, C.L., Hartnady, M.I.H., 2023. The global lead isotope system: toward a new framework reflecting Earth's dynamic evolution. Earth Sci. Rev. 243, 104483. https://doi.org/10.1016/j.earscirev.2023.104483.

Eiler, J.M., Farley, K.A., Valley, J.W., Stolper, E.M., Hauri, E.H., Craig, H., 1995. Oxygen isotope evidence against bulk recycled sediment in the mantle sources of Pitcairn Island lavas. Nature 377, 138–141. https://doi.org/10.1038/377138a0.

Eisele, J., Sharma, M., Galer, S.J.G., Blichert-Toft, J., Devey, C.W., Hofmann, A.W., 2002. The role of sediment recycling in EM-1 inferred from Os, Pb, Hf, Nd, Sr isotope and trace element systematics of the Pitcairn hotspot. Earth Planet. Sci. Lett. 196, 197–212. https://doi.org/10.1016/S0012-821X(01)00601-X.

Farley, K.A., Natland, J.H., Craig, H., 1992. Binary mixing of enriched and undegassed (primitive?) mantle components (he, Sr, Nd, Pb) in Samoan lavas. Earth Planet. Sci. Lett. 111, 183–199. https://doi.org/10.1016/0012-821X(92)90178-X.

Farnetani, C.G., Legras, B., Tackley, P.J., 2002. Mixing and deformation in mantle plumes. Earth Planet. Sci. Lett. 196, 1–15. https://doi.org/10.1016/S0012-821X(01)00597-0.

Frossard, P., Israel, C., Bouvier, A., Boyet, M., 2022. Earth's composition was modified by collisional erosion. Science 377, 1529–1532. https://doi.org/10.1126/science.abq7351.

Gale, A., Dalton, C.A., Langmuir, C.H., Su, Y., Schilling, J.-G., 2013. The mean composition of ocean ridge basalts. Geochem. Geophys. Geosyst. 14, 489–518. https://doi.org/10.1029/2012GC004334.

Garapic, G., Jackson, M.G., Hauri, E.H., Hart, S.R., Farley, K.A., Blusztajn, J.S., Woodhead, J.D., 2015. A radiogenic isotopic (He-Sr-Nd-Pb-Os) study of lavas from the Pitcairn hotspot: implications for the origin of EM-1 (enriched mantle 1). Lithos 228–229, 1–11. https://doi.org/10.1016/j.lithos.2015.04.010.

Gasperini, D., Blichert-Toft, J., Bosch, D., Del Moro, A., Macera, P., Télouk, P., Albarède, F., 2000. Evidence from Sardinian basalt geochemistry for recycling of plume heads into the Earth's mantle. Nature 408, 701–704. https://doi.org/10.1038/35047049.

Gast, P.W., Tilton, G.R., Hedge, C., 1964. Isotopic composition of lead and strontium from Ascension and Gough Islands. Science 145, 1181–1185. https://doi.org/10.1126/science.145.3637.1181.

Gautheron, C., Moreira, M., Gerin, C., Tassan-Got, L., Bezos, A., Humler, E., 2015. Constraints on the DUPAL anomaly from helium isotope systematics in the Southwest Indian mid-ocean ridge basalts. Chem. Geol. 417, 163–172. https://doi.org/10.1016/j.chemgeo.2015.10.005.

Geldmacher, J., Hoernle, K., Klügel, A., van den Bogaard, P., Bindeman, I., 2008. Geochemistry of a new enriched mantle type locality in the northern hemisphere: implications for the origin of the EM-I source. Earth Planet. Sci. Lett. 265, 167–182. https://doi.org/10.1016/j.epsl.2007.10.001.

Gibson, S.A., Thompson, R.N., Day, J.A., Humphris, S.E., Dickin, A.P., 2005. Melt-generation processes associated with the Tristan mantle plume: constraints on the origin of EM-1. Earth Planet. Sci. Lett. 237, 744–767. https://doi.org/10.1016/j.epsl.2005.06.015.

Gibson, S.A., Cale, C.W., Geist, D.J., Day, J.A., Brügmann, G., Harpp, K.S., 2016. The influence of melt flux and crustal processing on Re-Os isotope systematics of ocean island basalts: constraints from Galápagos. Earth Planet. Sci. Lett. 449, 345–359. https://doi.org/10.1016/j.epsl.2016.05.021.

Giuliani, A., Jackson, M.G., Fitzpayne, A., Dalton, H., 2021. Remnants of early Earth differentiation in the deepest mantle-derived lavas. Proc. Natl. Acad. Sci. USA 118, e2015211118. https://doi.org/10.1073/pnas.2015211118.

Graham, D.W., 2002. Noble gas isotope geochemistry of mid-ocean ridge and ocean island basalts: Characterization of mantle source reservoirs. In: Porcelli, D., Ballentine, C., Wieler, R. (Eds.), Noble Gases in Geochemistry and Cosmochemistry, 47. Reviews in Mineralogy and Geochemistry, Mineralogical Society of America, Washington DC, pp. 247–317. https://doi.org/10.2138/rmg.2002.47.8.

Graham, D.W., Michael, P.J., 2021. Predominantly recycled carbon in Earth's upper mantle revealed by He-CO_2-Ba systematics in ultradepleted ocean ridge basalts. Earth Planet. Sci. Lett. 554, 116646. https://doi.org/10.1016/j.epsl.2020.116646.

Graham, D.W., Humphris, S.E., Jenkins, W.J., Kurz, M.D., 1992. Helium isotope geochemistry of some volcanic rocks from Saint Helena. Earth Planet. Sci. Lett. 110, 121–131. https://doi.org/10.1016/0012-821X(92)90043-U.

Graham, D.W., Reid, M.R., Jordan, B.T., Grunder, A.L., Leeman, W.P., Lupton, J.E., 2009. Mantle source provinces beneath the Northwestern USA delimited by helium isotopes in young basalts. J. Volcanol. Geotherm. Res. 188, 128–140. https://doi.org/10.1016/j.jvolgeores.2008.12.004.

Graham, D.W., Hanan, B.B., Lupton, J.E., Hoernle, K., Werner, R., Christie, D.M., Sinton, J.M., 2014. Helium isotope variations and mantle plume-spreading ridge interactions along the Galapagos spreading center. In: Harpp, K.S., Mittelstaedt, E., d'Ozouville, N., Graham, D.W. (Eds.), The Galapagos: a natural laboratory for the earth sciences. Geophysical Monograph Series, Washington DC, pp. 393–414. https://doi.org/10.1002/9781118852538.ch18.

Graham, D.W., Michael, P.J., Rubin, K.H., 2018. An investigation of mid-ocean ridge degassing using he, CO_2, and $\delta^{13}C$ variations during the 2005-06 eruption at 9°50'N on the East Pacific rise. Earth Planet. Sci. Lett. 504, 84–93. https://doi.org/10.1016/j.epsl.2018.09.040.

Grand, S.P., van der Hilst, R.D., Widiyantoro, S., 1997. Global seismic tomography: a snapshot of convection in the Earth. GSA Today 7, 1–7.

Green, T.H., 1995. Significance of Nb/Ta as an indicator of geochemical processes in the crust-mantle system. Chem. Geol. 120, 347–359. https://doi.org/10.1016/0009-2541(94)00145-X.

Hanan, B.B., Graham, D.W., 1996. Lead and helium isotope evidence from oceanic basalts for a common deep source of mantle plumes. Science 272, 991–995. https://doi.org/10.1126/science.272.5264.991.

Hanyu, T., Kaneoka, I., 1997. The uniform and low $^3He/^4He$ ratios of HIMU basalts as evidence for their origin as recycled materials. Nature 390, 273–276. https://doi.org/10.1038/36835.

Hanyu, T., Tatsumi, Y., Senda, R., Miyazaki, T., Chang, Q., Hirahara, Y., Takahashi, T., Kawabata, H., Suzuki, K., Kimura, J.-I., Nakai, S., 2011. Geochemical characteristics and origin of the HIMU reservoir: a possible mantle plume source in the lower mantle. Geochem. Geophys. Geosyst. 12. https://doi.org/10.1029/2010GC003252. Q0AC09.

Hanyu, T., Kawabata, H., Tatsumi, Y., Kimura, J.-I., Hyodo, H., Sato, K., Miyazaki, T., Chang, Q., Hirahara, Y., Takahashi, T., Senda, R., Nakai, S., 2014. Isotope evolution in the HIMU reservoir beneath St. Helena: implications for the mantle recycling of U and Th. Geochim. Cosmochim. Acta 143, 232–252. https://doi.org/10.1016/j.gca.2014.03.016.

Harðardóttir, S., Halldórsson, S.A., Hilton, D.R., 2018. Spatial distribution of helium isotopes in Icelandic geothermal fluids and volcanic materials with implications for location, upwelling and evolution of the Icelandic mantle plume. Chem. Geol. 480, 12–27. https://doi.org/10.1016/j.chemgeo.2017.05.012.

Harðardóttir, S., Matthews, S., Halldórsson, S.A., Jackson, M.G., 2022. Spatial distribution and geochemical characterization of Icelandic mantle end-members: implications for plume geometry and melting processes. Chem. Geol. 604, 120930. https://doi.org/10.1016/j.chemgeo.2022.120930.

Harrison, L.N., Weis, D., Garcia, M.O., 2020. The multiple depleted mantle components in the Hawaiian-Emperor chain. Chem. Geol. 532, 119234. https://doi.org/10.1016/j.chemgeo.2019.119324.

Hart, S.R., 1984. A large-scale isotope anomaly in the Southern Hemisphere mantle. Nature 309, 753–757. https://doi.org/10.1038/309753a0.

Hart, S.R., Gaetani, G.A., 2006. Mantle Pb paradoxes: the sulfide solution. Contrib. Mineral. Petrol. 152, 295–308. https://doi.org/10.1007/s00410-006-0108-1.

Hart, S.R., Hauri, E.H., Oschmann, L.A., Whitehead, J.A., 1992. Mantle plumes and entrainment: isotopic evidence. Science 256, 517–520. https://doi.org/10.1126/science.256.5056.517.

Hauri, E.H., 1996. Major-element variability in the Hawaiian mantle plume. Nature 382, 415–419. https://doi.org/10.1038/382415a0.

Helffrich, G.R., Wood, B.J., 2001. The Earth's mantle. Nature 412, 501–507. https://doi.org/10.1038/35087500.

Hilton, D.R., Barling, J., Wheller, G.E., 1995. Effect of shallow-level contamination on the helium isotope systematics of ocean-island lavas. Nature 373, 330–333. https://doi.org/10.1038/373330a0.

Hilton, D.R., Grönvold, K., Macpherson, C.G., Castillo, P.R., 1999. Extreme 3He/4He ratios in Northwest Iceland: constraining the common component in mantle plumes. Earth Planet. Sci. Lett. 173, 53–60. https://doi.org/10.1016/S0012-821X(99)00215-0.

Hoernle, K., Tilton, G., Schmincke, H.-U., 1991. Sr-Nd-Pb isotopic evolution of Gran Canaria: evidence for shallow enriched mantle beneath the Canary Islands. Earth Planet. Sci. Lett. 106, 44–63. https://doi.org/10.1016/0012-821X(91)90062-M.

Hofmann, A.W., 1997. Mantle geochemistry: the message from oceanic volcanism. Nature 385, 219–229. https://doi.org/10.1038/385219a0.

Hofmann, A.W., 2014. Sampling mantle heterogeneity through oceanic basalts: isotopes and trace elements. In: Holland, H.D., Turekian, K.K. (Eds.), Treatise on Geochemistry, 3, pp. 67–101. https://doi.org/10.1016/B978-0-08-095975-7.00203-5.

Hofmann, A.W., White, W.M., 1982. Mantle plumes from ancient oceanic crust. Earth Planet. Sci. Lett. 57, 421–436. https://doi.org/10.1016/0012-821X(82)90161-3.

Hofmann, A.W., Jochum, K.P., Seufert, M., White, W.M., 1986. Nb and Pb in oceanic basalts: new constraints on mantle evolution. Earth Planet. Sci. Lett. 79, 33–45. https://doi.org/10.1016/0012-821X(86)90038-5.

Hofmann, A.W., Class, C., Goldstein, S.L., 2022. Size and composition of the MORB+OIB reservoir. Geochem. Geophys. Geosyst. 23, e2022GC010339. https://doi.org/10.1029/2022GC010339.

Hoggard, M.J., Parnell-Turner, R., White, N., 2020. Hotspots and mantle plumes revisited: towards reconciling the mantle heat transfer discrepancy. Earth Planet. Sci. Lett. 542, 116317. https://doi.org/10.1016/j.epsl.2020.116317.

Homrighausen, S., Hoernle, K., Hauff, F., Geldmacher, J., Wartho, J.-A., van den Bogaard, P., Garbe-Schönberg, D., 2018. Global distribution of the HIMU end member: formation through Archean plume-lid tectonics. Earth Sci. Rev. 182, 85–101. https://doi.org/10.1016/j.earscirev.2018.04.009.

Honda, M., Woodhead, J.D., 2005. A primordial solar-neon enriched component in the source of EM-I-type Ocean island basalts from the Pitcairn Seamounts, Polynesia. Earth Planet. Sci. Lett. 236, 597–612. https://doi.org/10.1016/j.epsl.2005.05.038.

Horton, F., Asimow, P.D., Farley, K.A., Curtice, J., Kurz, M.D., Blusztajn, J., Biasi, J.A., Boyes, X.M., 2023. Highest terrestrial 3He/4He credibly from the core. Nature 623, 90–94. https://doi.org/10.1038/s41586-023-06590-8.

Huang, S., Zheng, Y., 2017. Mantle geochemistry: insights from ocean island basalts. Sci. China Earth Sci. 60, 1976–2000. https://doi.org/10.1007/s11430-017-9090-4.

Ito, G., Mahoney, J.J., 2005. Flow and melting of a heterogeneous mantle: 2. Implications for a chemically nonlayered mantle. Earth Planet. Sci. Lett. 230, 47–63. https://doi.org/10.1016/j.epsl.2004.10.034.

Ito, G., Lin, J., Gable, C.W., 1997. Interaction of mantle plumes and migrating mid-ocean ridges: implications for the Galapagos plume-ridge system. J. Geophys. Res. 102, 15403–15417. https://doi.org/10.1029/97JB01049.

Jackson, M.G., Dasgupta, R., 2008. Compositions of HIMU, EM1, and EM2 from global trends between radiogenic isotopes and major elements in ocean island basalts. Earth Planet. Sci. Lett. 276, 175–186. https://doi.org/10.1016/j.epsl.2008.09.023.

Jackson, M.G., Macdonald, F.A., 2022. Hemispheric geochemical dichotomy of the mantle is a legacy of austral supercontinent assembly and onset of deep continental crust subduction. AGU Adv. 3, e2022AV000664. https://doi.org/10.1029/2022AV000664.

Jackson, M.G., Hart, S.R., Koppers, A.A.P., Staudigel, H., Konter, J., Blusztajn, J., Kurz, M., Russell, J.J., 2007a. The return of subducted continental crust in Samoan lavas. Nature 448, 684–687. https://doi.org/10.1038/nature06048.

Jackson, M.G., Kurz, M.D., Hart, S.R., Workman, R.K., 2007b. New Samoan lavas from Ofu Island reveal a hemispherically heterogeneous high ^{3}He/^{4}He mantle. Earth Planet. Sci. Lett. 264, 360–374. https://doi.org/10.1016/j.epsl.2007.09.023.

Jackson, M.G., Hart, S.R., Konter, J.G., Kurz, M.D., Blusztajn, J., Farley, K.A., 2014. Helium and lead isotopes reveal the geochemical geometry of the Samoan plume. Nature 514, 355–358. https://doi.org/10.1016/j.epsl.2008.09.023.

Jackson, M.G., Konter, J.G., Becker, T.W., 2017. Primordial helium entrained by the hottest mantle plumes. Nature 542, 340–343. https://doi.org/10.1038/nature21023.

Jackson, M.G., Blichert-Toft, J., Halldórsson, S.A., Mundl-Petermeier, A., Bizimis, M., Kurz, M.D., Price, A.A., Harðardóttir, S., Willhite, L.N., Breddam, K., Becker, T.W., Fischer, R.A., 2020. Ancient he and W isotopic signatures preserved in mantle domains least modified by crustal recycling. Proc. Natl. Acad. Sci. USA 117, 30993–31001. https://doi.org/10.1073/pnas.2009663117.

Jackson, M.G., Becker, T.W., Steinberger, B., 2021. Spatial characteristics of recycled and primordial reservoirs in the deep mantle. Geochem. Geophys. Geosyst. 22, e2020GC009525. https://doi.org/10.1029/2020GC009525.

Kamber, B.S., Collerson, K.D., 2000. Role of 'hidden' deeply subducted slabs in mantle depletion. Chem. Geol. 166, 241–254. https://doi.org/10.1016/S0009-2541(99)00218-1.

Kawabata, H., Hanyu, T., Chang, Q., Kimura, J.-I., Nichols, A.R.L., Tatsumi, Y., 2011. The petrology and geochemistry of St. Helena alkali basalts: evaluation of the oceanic crust-recycling model for HIMU OIB. J. Petrol. 52, 791–838. https://doi.org/10.1093/petrology/egr003.

Kendrick, M.A., Hémond, C., Kamenetsky, V.S., Danyushevsky, L., Devey, C.W., Rodemann, T., Jackson, M.G., Perfit, M.R., 2017. Seawater cycled throughout Earth's mantle in partially serpentinized lithosphere. Nat. Geosci. 10, 222–228. https://doi.org/10.1038/ngeo2902.

King, S.D., Adam, C., 2014. Hotspot swells revisited. Phys. Earth Planet. Inter. 235, 66–83. https://doi.org/10.1016/j.pepi.2014.07.006.

Kogiso, T., Hirschmann, M.M., Pertermann, M., 2004. High-pressure partial melting of mafic lithologies in the mantle. J. Petrol. 45, 2407–2422. https://doi.org/10.1093/petrology/egh057.

Kurz, M.D., Jenkins, W.J., Hart, S.R., 1982. Helium isotopic systematics of oceanic islands and mantle heterogeneity. Nature 297, 43–47. https://doi.org/10.1038/297043a0.

Kurz, M.D., Curtice, J., Fornari, D., Geist, D., Moreira, M., 2009. Primitive neon from the center of the Galapagos hotspot. Earth Planet. Sci. Lett. 286, 23–34. https://doi.org/10.1016/j.epsl.2009.06.008.

Labidi, J., Dottin III, J.W., Clog, M., Hemond, C., Cartigny, P., 2022. Near-zero ^{33}S and ^{36}S anomalies in Pitcairn basalts suggest Proterozoic sediments in the EM-1 mantle plume. Earth Planet. Sci. Lett. 584, 117422. https://doi.org/10.1016/j.epsl.2022.117422.

Lassiter, J.C., 2004. Role of recycled oceanic crust in the potassium and argon budget of the Earth: toward a resolution of the "missing argon" problem. Geochem. Geophys. Geosyst. 5. https://doi.org/10.1029/2004GC000711. Q11012.

Lassiter, J.C., Hauri, E.H., 1998. Osmium-isotope variations in Hawaiian lavas: evidence for recycled oceanic lithosphere in the Hawaiian plume. Earth Planet. Sci. Lett. 164, 483–496. https://doi.org/10.1016/S0012-821X(98)00240-4.

Licciardi, J.M., Clark, P.U., Brook, E.J., Pierce, K.L., Kurz, M.D., Elmore, D., Sharma, P., 2001. Cosmogenic ^{3}He and ^{10}Be chronologies of the late Pinedale northern Yellowstone ice cap, Montana, USA. Geology 29, 1095–1098. https://doi.org/10.1130/0091-7613(2001)029<1095:CHABCO>2.0.CO;2.

Macdonald, G.A., Katsura, T., 1964. Chemical composition of Hawaiian Lavas. J. Petrol. 5, 82–133. https://doi.org/10.1093/petrology/5.1.82.

Malaviarachchi, S.P.K., Makishima, A., Tanimoto, M., Kuritani, T., Nakamura, E., 2008. Highly unradiogenic lead isotope ratios from the Horoman peridotite in Japan. Nat. Geosci. 1, 859–863. https://doi.org/10.1038/ngeo363.

Marty, B., Pik, R., Gezahegn, Y., 1996. Helium isotopic variations in Ethiopian plume lavas: nature of magmatic sources and limit on lower mantle contribution. Earth Planet. Sci. Lett. 144, 223–237. https://doi.org/10.1016/0012-821X(96)00158-6.

McDonough, W.F., Sun, S.-S., 1995. The composition of the Earth. Chem. Geol. 120, 223–253. https://doi.org/10.1016/0009-2541(94)00140-4.

McKenzie, D., O'Nions, R.K., 1983. Mantle reservoirs and ocean island basalts. Nature 301, 229–231. https://doi.org/10.1038/301229a0.

Moreira, M.A., 2013. Noble gas constraints on the origin and evolution of Earth's volatiles. Geochem. Perspect. 2, 229–403. https://doi.org/10.7185/geochempersp.2.2.

Moreira, M.A., Kurz, M.D., 2001. Subducted oceanic lithosphere and the origin of the 'high μ' basalt helium isotopic signature. Earth Planet. Sci. Lett. 189, 49–57. https://doi.org/10.1016/S0012-821X(01)00340-5.

Moreira, M.A., Dosso, L., Ondreas, H., 2008. Helium isotopes on the Pacific-Antarctic ridge (52.5°–41.5°S). Geophys. Res. Lett. 35, L10306. https://doi.org/10.1029/2008GL033286.

Mukhopadhyay, S., Parai, R., 2019. Noble gases: a record of Earth's evolution and mantle dynamics. Annu. Rev. Earth Planet. Sci. 47, 389–419. https://doi.org/10.1146/annurev-earth-053018-060238.

Mundl, A., Touboul, M., Jackson, M.G., Day, J.M.D., Kurz, M.D., Lekic, V., Helz, R.T., Walker, R.J., 2017. Tungsten-182 heterogeneity in modern ocean island basalts. Science 356, 66–69. https://doi.org/10.1126/science.aal4179.

Mundl-Petermeier, A., Walker, R.J., Fischer, R.A., Lekic, V., Jackson, M.G., Kurz, M.D., 2020. Anomalous ^{182}W in high ^{3}He/^{4}He ocean island basalts: Fingerprints of Earth's core? Geochim. Cosmochim. Acta 271, 194–211. https://doi.org/10.1016/j.gca.2019.12.020.

Neave, D.A., Namur, O., Shorttle, O., Holtz, F., 2019. Magmatic evolution biases basaltic records of mantle chemistry towards melts from recycled sources. Earth Planet. Sci. Lett. 520, 199–211. https://doi.org/10.1016/j.epsl.2019.06.003.

O'Neill, H.St.C., Palme, H., 2008. Collisional erosion and the non-chondritic composition of the terrestrial planets. Phil. Trans. R. Soc. A 366, 4205–4238. https://doi.org/10.1098/rsta.2008.0111.

Oversby, V.M., Ringwood, A.E., 1971. Time of formation of the Earth's core. Nature 234, 463–465. https://doi.org/10.1038/234463a0.

Paquet, M., Day, J.M.D., Brown, D.B., Waters, C.L., 2022. Effective global mixing of the highly siderophile elements into Earth's mantle inferred from oceanic abyssal peridotites. Geochim. Cosmochim. Acta 316, 347–362. https://doi.org/10.1016/j.gca.2021.09.033.

Parman, S.W., 2007. Helium isotopic evidence for episodic mantle melting and crustal growth. Nature 446, 900–903. https://doi.org/10.1038/nature05691.

Parnell-Turner, R., White, N., Henstock, T., Murton, B., Maclennan, J., Jones, S.M., 2014. A continuous 55-million-yeat record of transient mantle plume activity beneath Iceland. Nature 7, 914–919. https://doi.org/10.1038/ngeo2281.

Paul, D., White, W.M., Blidhret-Toft, J., 2005. Geochemistry of Mauritius and the origin of rejuvenescent volcanism on oceanic island volcanoes. Geochemi. Goephys. Geosyst. 6. https://doi.org/10.1029/2004GC000883. Q06007.

Pertermann, M., Hirschmann, M.M., 2003. Anhydrous partial melting experiments on MORB-like eclogite: phase relations, phase compositions and mineral-melt partitioning of major elements at 2-3 GPa. J. Petrol. 44, 2173–2201. https://doi.org/10.1093/petrology/egg074.

Pietruszka, A.J., Norman, M.D., Garcia, M.O., Marske, J.P., Burns, D.H., 2013. Chemical heterogeneity in the Hawaiian mantle plume from the alteration and dehydration of recycled oceanic crust. Earth Planet. Sci. Lett. 361, 298–309. https://doi.org/10.1016/j.epsl.2012.10.030.

Pilet, S., Baker, M.B., Stolper, E.M., 2008. Metasomatized lithosphere and the origin of alkaline lavas. Science 320, 916–919. https://doi.org/10.1126/science.1156563.

Plank, T., Langmuir, C.H., 1998. The chemical composition of subducting sediment and its consequences for the crust and mantle. Chem. Geol. 145, 325–394. https://doi.org/10.1016/S0009-2541(97)00150-2.

Ribe, N.M., Christensen, U.R., 1999. The dynamical origin of Hawaiian volcanism. Earth Planet. Sci. Lett. 171, 517–531. https://doi.org/10.1016/S0012-821X(99)00179-X.

Rudge, J.F., 2009. Finding peaks in geochemical distributions: a re-examination of the helium-continental crust correlation. Earth Planet. Sci. Lett. 274, 179–188. https://doi.org/10.1016/j.epsl.2008.07.021.

Rudnick, R.L., Barth, M., Horn, I., McDonough, W.F., 2000. Rutile-bearing refractory eclogites: missing link between continents and depleted mantle. Science 287, 278–281. https://doi.org/10.1126/science.287.5451.278.

Ruttor, S., Nebel, O., Nebel-Yacobsen, Y., Cohen, B.E., Eggins, S., 2021. Alkalinity of ocean island lavas decoupled from enriched source components: a case study from the EM1-PREMA Tasmantid mantle plume. Geochim. Cosmochim. Acta 314, 140–158. https://doi.org/10.1016/j.gca.2021.09.023.

Salters, V.J.M., Sachi-Kocher, A., 2010. An ancient metasomatic source for the Walcis Ridge basalts. Chem. Geol. 273, 151–167. https://doi.org/10.1016/j.chemgeo.2010.02.010.

Schilling, J., 1991. Fluxes and excess temperatures of mantle plumes inferred from their interaction with migrating mid-ocean ridges. Nature 352, 397–403. https://doi.org/10.1038/352397a0.

Shorttle, O., Maclennan, J., 2011. Compositional trends of Icelandic basalts: implications for short-length scale lithological heterogeneity in mantle plumes. Geochem. Geophys. Geosyst. 12. https://doi.org/10.1029/2011GC003748. Q11008.

Shorttle, O., Rudge, J.F., Maclennan, J., Rubin, K.H., 2016. A statistical description of concurrent mixing and crystallization during MORB differentiation: implications for trace element enrichment. J. Petrol. 57, 2127–2162. https://doi.org/10.1093/petrology/egw056.

Sleep, N.H., 1990. Hotspots and mantle plumes: some phenomenology. J. Geophys. Res. 95, 6715–6736. https://doi.org/10.1029/JB095iB05p06715.

Sobolev, A.V., Hofmann, A.W., Kuzmin, D.V., Yaxely, G.M., Arndt, N.T., Chung, S.-L., Danyushevsky, L.V., Elliott, T., Frey, F.A., Garcia, M.O., Gurenko, A.A., Kamenetsky, V.S., Kerr, A.C., Krivolutskaya, N.A., Matvienkov, V.V., Nikogosian, I. K., Rocholl, A., Sigurdsson, I.A., Sushchevskaya, N.M., Teklay, M., 2007. The amount of recycled crust in sources of mantle-derived melts. Science 316, 412–417. https://doi.org/10.1126/science.

Šrámek, O., McDonough, W.F., Kite, E.S., Lekic, V., Dye, S.T., Zhong, S., 2013. Geophysical and geochemical constraints on geoneutrino fluxes from Earth's mantle. Earth Planet. Sci. Lett. 361, 356–366. https://doi.org/10.1016/j.epsl.2012.11.001.

Starkey, N.A., Stuart, F.M., Ellam, R.M., Fitton, J.G., Basu, S., Larsen, L.M., 2009. Helium isotopes in early Iceland plume picrites: constraints on the composition of high ^{3}He/^{4}He mantle. Earth Planet. Sci. Lett. 277, 91–100. https://doi.org/10.1016/j.epsl.2008.10.007.

Stracke, A., 2012. Earth's heterogeneous mantle: a product of convection-driven interaction between crust and mantle. Chem. Geol. 330–331, 274–299. https://doi.org/10.1016/j.chemgeo.2012.08.007.

Stracke, A., 2021. A process-oriented approach to mantle geochemistry. Chem. Geol. 579, 120350. https://doi.org/10.1016/j.chemgeo.2021.120350.

Stracke, A., Bizimis, M., Salters, V.J.M., 2003. Recycling oceanic crust: quantitative constraints. Geochem. Geophys. Geosyst. 4, 8003. https://doi.org/10.1029/2001GC000223.

Stracke, A., Hofmann, A.W., Hart, S.R., 2005. FOZO, HIMU, and the rest of the mantle zoo. Geochem. Geophys. Geosyst. 6. https://doi.org/10.1029/2004GC000824. Q05007.

Stracke, A., Genske, F., Berndt, J., Koornneef, J.M., 2019. Ubiquitous ultra-depleted domains in Earth's mantle. Nat. Geosci. 12, 851–855. https://doi.org/10.1038/s41561-019-0446-z.

Stracke, A., Willig, M., Genske, F., Beguelin, P., Todd, E., 2022. Chemical geodynamics insights from a machine learning approach. Geochem. Geophys. Geosyst. 23, e2022GC010606. https://doi.org/10.1029/2022GC010606.

Stroncik, N., Niedermann, S., Schnabel, E., Erzinger, J., 2011. Determining the geochemical structure of the mantle from surface isotope distribution patterns? Insights from Ne and he isotopes and abundance ratios. In: AGU Fall Meeting Abstract V51B-2519.

Tang, M., Rudnick, R.L., McDonough, W.F., Gaschnig, R.M., Huang, Y., 2015. Europium anomalies constrain the mass of recycled lower continental crust. Geology 43, 703–706. https://doi.org/10.1130/G36641.1.

Tatsumi, Y., 2000. Continental crust formation by crustal delamination in subduction zones and complementary accumulation of the enriched mantle I component in the mantle. Geochem. Geophys. Geosyst. 1. https://doi.org/10.1029/2000GC000094, 2000GC000094.

Taylor, R.N., Ishizuka, O., Michalik, A., Milton, J.A., Croudace, I.W., 2015. Evaluating the precision of Pb isotope measurement by mass spectrometry. J. Anal. At. Spectrom. 30, 198–213. https://doi.org/10.1039/C4JA00279B.

Turner, S.J., Langmuir, C.H., 2015. The global chemical systematics of arc front stratovolcanoes: evaluating the role of crustal process. Earth Planet. Sci. Lett. 422, 182–193. https://doi.org/10.1016/j.epsl.2015.03.056.

Turner, S.J., Langmuir, C.H., Dungan, M.A., Escrig, S., 2017. The importance of mantle wedge heterogeneity to subduction zone magmatism and the origin of EM1. Earth Planet. Sci. Lett. 472, 216–228. https://doi.org/10.1016/j.epsl.2017.04.051.

Valbracht, P.J., Staudacher, T., Malahoff, A., Allègre, C.J., 1997. Noble gas systematics of deep rift zone glasses from Loihi Seamount, Hawaii. Earth Planet. Sci. Lett. 150, 399–411. https://doi.org/10.1016/S0012-821X(97)00094-0.

Vollmer, R., 1977. Terrestrial lead isotopic evolution and formation time of the Earth's core. Nature 270, 144–147. https://doi.org/10.1038/270144a0.

Wang, X.-J., Chen, L.-H., Hofmann, A.W., Hanyu, T., Kawabata, H., Zhong, Y., Xie, L.-W., Shi, J.-H., Miyazaki, T., Hirahara, Y., Takahashi, T., Senda, R., Chang, Q., Vaglarov, B.S., Kimura, J.-I., 2018. Recycled ancient ghost carbonate in the Pitcairn mantle plume. Proc. Natl. Acad. Sci. USA 115, 8682–8687. https://doi.org/10.1073/pnas.1719570115.

Weaver, B.L., 1991. The origin of ocean island basalt end-member compositions: trace element and isotopic constraints. Earth Planet. Sci. Lett. 104, 381–397. https://doi.org/10.1016/0012-821X(91)90217-6.

Weis, D., Bassias, Y., Gautier, I., Mennessier, J.-P., 1989. Dupal anomaly in existence 115 Ma ago: evidence from isotopic study of the Kerguelen Plateau (South Indian Ocean). Geochim. Cosmochim. Acta 53, 2125–2131. https://doi.org/10.1016/0016-7037(89)90331-1.

Weis, D., Garcia, M.O., Rhodes, J.M., Jellinek, M., Scoates, J.S., 2011. Role of the deep mantle in generating the compositional asymmetry of the Hawaiian mantle plume. Nat. Geosci. 4, 831–838. https://doi.org/10.1038/NGEO1328.

Weis, D., Harpp, K.S., Harrison, L.N., Boyet, M., Chauvel, C., Farnetani, C.G., Finlayson, V.A., Lee, K.K.M., Parai, R., Shahar, A., Williamson, N.M.B., 2023. Earth's mantle composition revealed by mantle plumes. Nat. Revi. Earth & Environ. 4, 604–625. https://doi.org/10.1038/s43017-023-00467-0.

Weiss, Y., Class, C., Goldstein, S.L., Hanyu, T., 2016. Key new pieces of the HIMU puzzle from olivines and diamond inclusions. Nature 537, 666–670. https://doi.org/10.1038/nature19113.

White, W.M., 1985. Sources of oceanic basalts: radiogenic isotopic evidence. Geology 13, 115–118. https://doi.org/10.1130/0091-7613(1985)13<115:SOOBRI>2.0.CO;2.

White, W.M., 2010. Ocean Island basalts and mantle plumes: the geochemical perspective. Annu. Rev. Earth Planet. Sci. 38, 133–160. https://doi.org/10.1146/annurev-earth-040809-152450.

White, W.M., 2015. Isotopes, DUPAL, LLSVPs, and Anekantavada. Chem. Geol. 10–28. https://doi.org/10.1016/j.chemgeo.2015.09.026.

White, W.M., Duncan, R.A., 1996. Geochemistry and geochronology of the Society Islands: New evidence for deep mantle recycling. In: Basu, A., Hart, S. (Eds.), Earth Processes: Reading the Isotopic Code, 95. Geophysical Monograph Series, AGU, pp. 183–206. https://doi.org/10.1029/GM095p0183.

White, W.M., Hofmann, A.W., 1982. Sr and Nd isotope geochemistry of oceanic basalts and mantle evolution. Nature 296, 821–825. https://doi.org/10.1038/296821a0.

Willbold, M., Stracke, A., 2006. Trace element composition of mantle end-members: Implications for recycling of oceanic and upper and lower continental crust. Geochem. Geophys. Geosyst. 7. https://doi.org/10.1029/2005GC001005. Q04004.

Willbold, M., Stracke, A., 2010. Formation of enriched mantle components by recycling of upper and lower continental crust. Chem. Geol. 276, 188–197. https://doi.org/10.1016/j.chemgeo.2010.06.005.

Willhite, L., Jackson, M.G., Blichert-Toft, J., Bindeman, I., Kurz, M.D., Halldórsson, S.A., Harðardóttir, S., Gazel, E., Price, A.A., Byerly, B.L., 2019. Hot and heterogenous high-^{3}He/^{4}He components: new constraints from proto-Iceland plume lavas from Baffin Island. Geochem. Geophys. Geosyst. 20, 5939–5967. https://doi.org/10.1029/2019GC008654.

Woodhead, J.D., 1996. Extreme HIMU in an oceanic setting: the geochemistry of Mangaia Island (Polynesia), and temporal evolution of the Cook-Austral hotspot. J. Volcanol. Geotherm. Res. 72, 1–19. https://doi.org/10.1016/0377-0273(96)00002-9.

Woodhead, J.D., Devey, C.W., 1993. Geochemistry of the Pitcairn seamounts, I: source character and temporal trends. Earth Planet. Sci. Lett. 116, 81–99. https://doi.org/10.1016/0012-821X(93)90046-C.

Woodhead, J.D., McCulloch, M.T., 1989. Ancient seafloor signals in Pitcairn Island lavas and evidence for large amplitude, small length-scale mantle heterogeneities. Earth Planet. Sci. Lett. 94, 257–273. https://doi.org/10.1016/0012-821X(89)90145-3.

Woodhead, J.D., Greenwood, P., Harmon, R.S., Stoffers, P., 1993. Oxygen isotope evidence for recycled crust in the source of EM-type Ocean island basalts. Nature 362, 809–813. https://doi.org/10.1038/362809a0.

Workman, R.K., Hart, S.R., Jackson, M., Regelous, M., Farley, K.A., Blusztajn, J., Kurz, M., Staudigel, H., 2004. Recycled metasomatized lithosphere as the origin of the Enriched Mantle II (EM2) end-member: evidence from the Samoan volcanic chain. Geochem. Geophys. Geosyst. 5, Q04008. https://doi.org/10.1029/2003GC000623.

Workman, R.K., Eiler, J.M., Hart, S.R., Jackson, M.G., 2008. Oxygen isotopes in Samoan lavas: confirmation of continent recycling. Geology 36, 551–554. https://doi.org/10.1130/G24558A.1.

Zartman, R.E., Haines, S.M., 1988. The plumbotectonic model for Pb isotopic systematics among major terrestrial reservoirs–a case for bi-directional transport. Geochim. Cosmochim. Acta 52, 1327–1339. https://doi.org/10.1016/0016-7037(88)90204-9.

Zhang, J.-B., Liu, Y.-S., Ducea, M.N., Xu, R., 2020. Archean, highly unradiogenic lead in shallow cratonic mantle. Geology 48, 584–588. https://doi.org/10.1130/G47064.1.

Zindler, A., Hart, S., 1986. Chemical geodynamics. Annu. Rev. Earth Planet. Sci. 14, 493–571. https://doi.org/10.1146/annurev.ea.14.050186.002425.